

ON THE PLANETHOOD OF TITAN

-

CLASSIFICATION, NON-LINEAR STABILITY, AND
FLUID-DYNAMICS OF ISOTHERMAL PROTOPLANETS

By

Bojan Pečnik

from Zagreb

SUBMITTED IN PARTIAL FULFILLMENT OF THE
REQUIREMENTS FOR THE DEGREE OF
DOCTOR OF NATURAL SCIENCES

AT

LUDWIG-MAXIMILIANS-UNIVERSITY
MÜNCHEN, GERMANY

18TH JANUARY 2006

LUDWIG-MAXIMILIANS-UNIVERSITY
FACULTY OF PHYSICS

Dated: 18th January 2006

Research Supervisor:

Gregor Morfill

External Examiner:

Ralph Neuhäuser

Examining Committee:

Martin Fässler

Ralf Bender

Alex Schenzle

Table of Contents

Table of Contents	iv
Abstract	vi
Acknowledgements	vii
Questions in the planetary astrophysics	2
1 Hydrostatic Classification	6
1.1 Introduction	6
1.2 Model	8
1.2.1 Motivation	8
1.2.2 Model Assumptions	9
1.2.3 Model Equations	9
1.2.4 Boundary Conditions	10
1.2.5 Solution Procedure	10
1.3 Results	12
1.3.1 Solution Manifold	12
1.3.2 Manifold Regions	14
1.3.3 Self-Gravity Effect	15
1.3.4 Two types of envelope equilibria	17
1.3.5 Differences: Isothermal Coreless Gas Spheres vs. Isothermal Proto-planets	17
1.3.6 Estimating the Applicability of the Ideal Gas	19
1.3.7 Estimating the Applicability of the Isothermal Assumption	22
1.3.8 Manifolds and Environment	24
1.3.9 Static Critical Core Mass	27
1.3.10 Temperature-Mass Invariance	33
1.3.11 Critical core and core density	34
1.4 Discussion and Conclusions	34
2 Planets and minor bodies	39
2.1 Low-mass planetary boundary	39

2.2	Planethood affiliation in the solar system	41
3	Hydrodynamic Classification	45
3.1	Computational strategy	46
3.2	Hydro-code setup	47
3.3	Scheme tests	56
3.3.1	Saw-tooth profile advection	56
3.3.2	Free-fall	57
3.3.3	Isothermal shock tube	62
3.4	Hydro-dynamical surveys	80
3.4.1	Types of dynamical behavior	83
3.4.2	Medium core density	86
3.4.3	Low core density	106
3.5	Fluid-dynamics and disk-planet models	120
3.5.1	Future of the disk-planet calculations	120
3.5.2	Perturbations and the protoplanetary evolution	121
4	Summary and Discussion	122
	Bibliography	132

Abstract

This work aims to clarify some of the basic concepts of the giant planet formation.

In order to enhance the understanding of the general roadmap of the giant planet formation we have mapped out all the qualitatively different protoplanetary equilibria, for a simple isothermal self-gravitating core-envelope model.

A clear concept for the distinction between a planet and a minor body naturally follows from our static classification. We explain e.g. why Titan has an atmosphere, while Rhea has none. Also, we offer a new interpretation for the locally isothermal disk-planet interaction calculations.

We examine the role of so-called critical mass, necessary to permanently attract gas of the protoplanetary nebula to a terrestrial-planet-like, heavy element core. We develop a concept for the global static critical core mass, as a core of a protoplanet which connects all four qualitatively different parameter-space regions of the core-envelope solutions.

To determine the subset of physically significant protoplanetary solutions, as well as to investigate the role of the stability in the formation of the planets, we perform the non-linear stability analysis - the evolution of the models which are the typical representatives of their class is followed on a timescale of the envelope dynamics.

We find five basic modes of dynamical behavior: *oscillation*, *pulsation*, *transition*, *ejection*, and *collapse*. We also investigate and identify the transitions within a classified protoplanetary core-envelope solution set. Static core-envelope solutions can be either stable or unstable, depending on the region of a parameter-space. We find examples of both linear and non-linear instability. We find that the whole parameter-space region around the critical core mass is unstable against collapse.

Acknowledgements

I would like to thank to Professor Gregor Morfill, my supervisor, for his generous support from the start, and for his approval of my non-scientific, space- and education-related endeavors.

I am indebted to Dr. Günther Wuchterl for his guidance, advice, and continuous support during this research. Thank You for always being there for me, for helping me to see the beauty and feel the excitement of a discovery.

Professor Ralph Neuhäuser was kind enough to support me with a pleasant working environment and a friendly atmosphere of his scientific group. Working within such a team was a pleasure, as were the scientific discussions with Christopher Broeg and Johannes Schönke.

My graduate studies in Germany were supported in part by the Croatian Ministry of Science, Education, and Sport.

I will be eternally grateful to my parents for their patience, love, and support.

Finally, I want to thank Aleksandra for making this world even more beautiful.

‘The current understanding of the planetary astrophysics reminds me of the build-up of the Ptolemy’s crystal spheres’.

Dr Tsevi Mazeh

We (the planetary astrophysicists) understand only parts of the evolution of the planetary systems, and have little knowledge of the global evolutionary properties of the planets. Studying particular cases of the planetary evolution, described with models containing detailed physics, revealed a whole zoo of different planetary properties including different core growth models, protoplanetary disk stability and interaction issues, a variety of relevant timescales, chaotic dynamical nature, etc. It became clear that the investigation of a single aspect of the evolution of a planetary system, no matter how careful and detailed, will stand only a small chance of delivering a general understanding of the planetary evolution that would be comparable to the current understanding of the evolution of stars.

With the complexity of the issue in mind, we choose a different approach that should provide more insight to a planetary evolution. Questions we will try to address are discussed in the introductory chapter. We selected a simple model which should be a reasonably good representation for the protoplanet during the largest part of its early evolution. We address the model applicability in Chapter 1. In the same Chapter we classify static protoplanets into four qualitatively different regimes. In Chapter 2 we discuss the implications of such classification for the definition of a planetary body. We try to discriminate the physically significant models from all the available solutions in Chapter 3, as well as to understand the typical dynamical protoplanetary timescales and perturbations.

Questions in the planetary astrophysics

The problematique of planet formation is interwoven with star formation, protoplanetary disks, the growth of dust and solid planets in those nebula disks, and finally nebula dispersal (e.g. Hayashi et al., 1985).

Planets are believed to form concurrently with a ‘parent’ star, from a centrifugally-supported disk of gas and dust (e.g. Safronov, 1969; Lissauer, 1993). The protoplanetary nebulae are a natural outcome of the modelling of the observed cloud core conditions, if a macroscopic mechanism for the angular momentum transfer exists (e.g. Morfill et al., 1985). However, present modelling still cannot span the evolution from the cloud collapse to the protoplanetary nebula conditions, where the planet formation occurs.

Disk observations have recently improved with the introduction of the infra-red space-based Spitzer telescope (e.g. Chen et al., 2005), but the observational data for the inner disk (0.05-30 AU) still ‘can not be used to discriminate between various one-parameter disk models’¹. Although, observations do show that the disk disappearance occurs on a 10 – 30 Ma time scale, and there are indications of the inner (dust) disk disappearing before the outer part, as if being ‘eaten’ by forming planets. The radial velocity observations also show uniform distribution of the orbital distances of mature extra-solar planets (see ‘California & Carnegie Planet Search’ webpage² and ‘Lists of Extrasolar Planets’³ of the IAU’s Working Group on Extrasolar Planets, as well as Jean Schneider’s ‘Extrasolar

¹quote from the summary of the ‘Disks to Planets 2005’ conference, Pasadena, California

²<http://exoplanets.org/massradiiframe.html>

³<http://www.dtm.ciw.edu/boss/IAU/div3/wgesp/planets.html>

Planets Encyclopaedia'⁴, or Udry et al. (2003) and Santos et al. (2003)), hinting that there is no preferred orbital position for the formation of the gas giants around the solar-type stars.

Theory provides several ways to form giant planets (for a review see Wuchterl et al., 2000), of which the ‘nucleated instability’ is serving as the standard model for the planet formation. In this model, a gravity field of a sufficiently large solid core (i.e. ‘the critical core’) is used to produce a local enhancement of self-gravity, necessary to overcome the counteracting gas pressure and trigger the accumulation of planet’s envelope. Other models provide the necessary gravity field through the gravitational instability of the nebula itself (the ‘disk instability’ model), or through an ‘external perturber’ (e.g. rendezvous with a stellar companion), or through a ‘fragmentation during collapse’, although the last case is unlikely to form objects of planetary mass because opacity limits the process to masses above $\approx 10 M_J$ (see Bodenheimer et al., 1993).

It is not exactly clear what is the nature of the instability connected with the formation of a giant planet. It has the elements of disk instability (i.e. Toomre instability), and the cloud instability (i.e. Jeans instability), but its neither of those; the nebulous disk forms a planet in a presence of an external gravity field (i.e. core), and the relevant instability most likely has properties which can be fully understood only through the analysis of all three spatial dimensions.

In general, present theory of the planet formation still leaves its key building blocks somewhat unconstrained. Complexity of the constitutive physical processes is surely to blame for the lack of the complete picture, but it can also partly be attributed to the insufficient knowledge of the typical protoplanetary environment. On the other hand, current diversity of the observations of the extra-solar planets is still waiting to be explained by the theory’s ‘planetary main sequence’.

We tried to address this apparent deadlock by providing a roadmap toward a general

⁴<http://www.obspm.fr/encycl/encycl.html>

framework of the planet formation, within a paradigm of the standard model (i.e. the nucleated instability);

During the early stages of the planetary evolution, typical dynamical processes most likely operate on the time-scales much smaller than the core-accretion timescale. Thus, most of its early days proto-planet will spend in a hydro-static equilibrium or very close to it. It was therefore important to provide an idealized but complete survey of all hydrostatic states. We provide such a classification for an isothermal core-envelope model, based on a fairly simple set of assumptions (c.f. Chapter 1). A comparison of our classification with an analogous study containing improved microphysics (Broeg, 2005, including numerical equation of state, detailed energy transfer, and tabulated gas and dust opacities), shows that our model provides a qualitatively correct and complete overview of hydrostatic equilibria.

Based on the compactness and the self-gravitating properties of our core-envelope models, we classify protoplanetary equilibria into four categories (c.f. Sect. 1.3.2):

‘mature telluric planet’, ‘mature gas giant’, ‘nebula’, and ‘protoplanet’.

Furthermore, we redefine the concept of the static critical core mass as the core mass of the model which connects all four qualitatively different envelope categories.

The role of a critical core in the planet evolution has been associated with the envelope gas accumulation, either through a quasi-static accretion or through an envelope collapse. The evolution of just-critical models was followed by other investigators, through a sequence of quasi-static models (e.g. Ikoma et al., 2001; Bodenheimer et al., 2000), or dynamically (e.g. Wuchterl, 1991a,b, 1993), with discrepant results which were difficult to put into a single, general framework.

We aim to provide a simplified, but general paradigm for the protoplanetary evolution up to, and around, the critical core mass, through the stability analysis of our qualitatively complete set of static solutions.

The issue of the equilibrium stability could have been looked into through the linear

stability analysis, or through the non-linear hydro-dynamical evolution. While the linear analysis can discriminate a linearly stable equilibrium from an unstable one, it cannot provide sufficient information about the end-state of the unstable equilibria. Thus we perform a non-linear analysis of all qualitatively different protoplanets, using (the typical representatives of) the equilibria from our static classification as initial states for hydro-dynamic simulations (c.f. Chapter 3).

With such an approach, three main issues that we address are;

First, we investigate whether a protoplanetary embryo necessarily has to acquire a critical core mass in order to become a giant planet, or whether there is another venue to initiate an envelope accumulation (c.f. Sect. 3.4.2: *Subcritical core mass model sequence*). Such an evolutionary option, alternative to the steady (sub-critical) core growth, could help solve the biggest problem of the current standard model - the core growth/nebula dissipation timescale mismatch.

Second issue deals with the protoplanetary dynamics around the critical core mass (c.f. Sect. 3.4.2: *Region around the critical core*). A detailed look at all qualitatively different models in the vicinity of the critical core could potentially lead to a joint framework for the previously disparate studies of the critical models.

Third, we investigate, and confirm, the stability of the compact protoplanet against the nebula removal. As a corollary, we develop one of the criteria an object needs to fulfill in order for it to be a planet (c.f. Sect. 2.1), i.e. using our new concept of the critical core mass, we precisely determine requirements, on the planetary body, necessary to retain the gaseous envelope in the vacuum of space.

Chapter 1

Hydrostatic Classification

In this chapter we classify the protoplanets according to the general properties of their envelopes. Resulting from this classification, we provide a concise and precise statement for distinction between a planet and a minor planet, discussed in Chapter 2. We also develop a concept for the global static critical core mass, a core of a protoplanet which connects all four qualitatively different envelope regimes. We present the multiplicity of protoplanetary solutions, and discuss the role of the envelope self-gravity. We show that the self-gravitating effect can determine the envelope features even if the envelope mass is small compared to the core mass.

1.1 Introduction

With the discovery of the extra-solar gas giants, the general problem of the planet formation has considerably grown in complexity over the last decade. However, a global theoretical overview of the properties of the giant planets, irrespective of the parent protoplanetary disc or the total mass of the giant planet, is still missing.

In the *nucleated instability* hypothesis, envelopes of giant planets are thought to be formed as a consequence of accretion of solid bodies forming their cores. To determine the envelope mass corresponding to a given core, static protoplanetary models have been constructed (e.g. Perri and Cameron, 1974; Mizuno, 1980; Stevenson, 1982).

If the envelope is modelled including detailed energy transfer and if the outer part of the envelope is radiative, and for standard assumptions about nebula conditions, it has been found that there is an upper limit for the masses of static envelopes and therefore for the total mass of a proto giant planet. This upper limit in core mass - the critical mass - was found to be insensitive to nebula conditions, but to weakly depend on dust opacities (Mizuno, 1980) and on the rate at which the core (solid body) is accreted (Stevenson, 1982).

Even the largest static critical masses are typically more than a factor of ten smaller than Jupiter's mass (see Mizuno, 1980; Stevenson, 1982; Wuchterl, 1991b; Ikoma et al., 2001). The nondependence of the critical mass on nebula conditions disappears when the outermost parts of the protoplanetary envelopes become convective, which happens for nebula properties which are well within of proposed solar nebula conditions (Wuchterl, 1993). Envelope masses of such protoplanets range between 6 and 48 Earth masses (M_{\oplus}) but hydrostatic models alone are unable to reproduce a Jupiter-mass protoplanet. Therefore dynamical and/or quasi-hydrostatical effects should play an important role in formation of gas giants.

There are a number of incompletely studied processes (e.g. the formation, evolution, and stability of the protoplanetary disks, the dust growth, the planetesimal formation, etc.) that are relevant for the general problem of planet formation. Their complexity makes a piecewise approach necessary in studies of planet formation. An alternative approach is to study the final outcome, i.e. the possible and probable end-states of the process. In that context, we present an idealized road-map of all hydrostatic states, in order to provide insight when analyzing the complex behavior of hydrodynamic and quasi-hydrostatic models with detailed microphysics. In addition, this work aims to clarify the concept of the critical core mass necessary to permanently attract gas of the protoplanetary nebula to a terrestrial-planet-like heavy element core.

1.2 Model

1.2.1 Motivation

Within nucleated instability theory, the formation of giant planets includes many possible scenarios for protoplanetary cores and their respective envelopes. Those range from small planetoids embedded in dilute protoplanetary nebulae to present-day-Jovian-like cores of several M_{\oplus} squeezed by some Mbars of metallic H_2 -He mixtures (Guillot, 1999). To date, many investigations have been made into the evolution of protoplanets, both hydrostatically (Bodenheimer et al., 2000; Ikoma et al., 2001), (for review see Wuchterl et al., 2000) and hydrodynamically (e.g. Wuchterl, 1991a,b, 1993). In these studies, 'the evolution' of *particular* planets is followed, but not much is known about the evolution of all possible protoplanets. Therefore, it is somewhat *difficult to frame the detailed solutions of previous investigations within a global perspective*.

We follow the thermodynamical approach that was used by (Stahl et al., 1995) to investigate the coreless equilibria of constant mass, isothermal gas spheres, and the nature of the Jeans instability. We also expand on the work of (Sasaki, 1989), who studied isothermal protoplanets in the minimum mass solar nebula (MMSN). In our model the total mass of the protoplanet and the density of nebula cloud, in which the protoplanet is embedded, are not prescribed. In leaving these as output variables, and starting only with the (heavy-element) core mass and the density of the envelope gas at the core's surface, we aim for a *complete classification of all hydrostatic equilibria*. This classification should contribute in clarifying whether multiple planetary equilibria exist for given nebula conditions and how protoplanetary models relate to gas giants, both inside and outside of the solar system.

1.2.2 Model Assumptions

We approximate the protoplanet as a spherically symmetric, isothermal, self-gravitating classical ideal gas envelope in equilibrium around a core of given mass. This gaseous envelope is that required to fill the gravitational sphere of influence, approximated by the Hill-sphere:

$$r_{\text{Hill}} = a \sqrt[3]{M_{\text{planet}}/3M_{\star}}, \quad (1.2.1)$$

where a is the orbital distance from a parent star. With mean molecular weight of $\mu = 2.3 \cdot 10^{-3} \text{ kg mol}^{-1}$, protoplanetary envelopes, as well as the nebula, are roughly approximated by a hydrogen-helium mixture. The protoplanet's heavy-element-core is represented by a rigid sphere of uniform density of $\varrho_{\text{core}} = 5500 \text{ kg m}^{-3}$.

The nebula temperature profile is taken according to (Kusaka et al., 1970; Hayashi et al., 1985), cf. Table 1.2. The nebula density structure is not *a priori* determined, but, for critical core mass determination, nebula densities agree with those from (Kusaka et al., 1970) for $a = 1$ and 30 AU, and from (Hayashi et al., 1985) for $a = 5.2$ AU, cf. Table 1.2. It has been shown that the critical core mass values have only a weak dependence on the nebula density (cf. Sect. 1.3.9), therefore choice of the nebula density is not critical.

1.2.3 Model Equations

The envelope is set in isothermal hydrostatic equilibrium, with spherical symmetry, and as such is described by:

$$\frac{dM(r)}{dr} = 4\pi r^2 \varrho(r), \quad (1.2.2)$$

the equation of hydrostatic equilibrium:

$$\frac{dP(r)}{dr} = -\frac{GM(r)}{r^2} \varrho(r), \quad (1.2.3)$$

and the equation of state for an ideal gas:

$$P(r) = \frac{\mathfrak{R}T}{\mu} \varrho(r). \quad (1.2.4)$$

$M(r)$ is defined as the total mass (core plus envelope) contained within the radius r :

$$M(r) = M_{core} + \int_{r_{core}}^r 4\pi r'^2 \varrho(r') dr', \quad (1.2.5)$$

where r is the radial distance measured from the core center and ϱ is the envelope gas density at radial distance r .

1.2.4 Boundary Conditions

The total mass of the protoplanet is defined as:

$$M_{tot} = M_{core} + M_{env} = M(r_{out}) \quad (1.2.6)$$

with

$$M(r_{core}) = M_{core}. \quad (1.2.7)$$

The inner and outer radial boundaries are:

$$r_{in} = r_{core} = \sqrt[3]{\frac{M_{core}}{\frac{4}{3}\pi\varrho_{core}}} \quad \text{and} \quad r_{out} = r_{Hill}. \quad (1.2.8)$$

An additional boundary condition at the core surface is:

$$\varrho_{env}(r_{core}) = \varrho_{csg}. \quad (1.2.9)$$

This model, together with the specified assumptions and boundary conditions, is sufficient to completely determine a single model-protoplanet. The total mass and nebula density at r_{Hill} (gas density at protoplanet's outer boundary) are results of the calculation.

1.2.5 Solution Procedure

The total protoplanetary mass is obtained by integrating outward from r_{core} to $r_{Hill}(M_{tot})$, starting with $r_{Hill}^0 = r_{Hill}(M_{core})$ and iterating $r_{Hill}(M_{core} + M_{env})$.

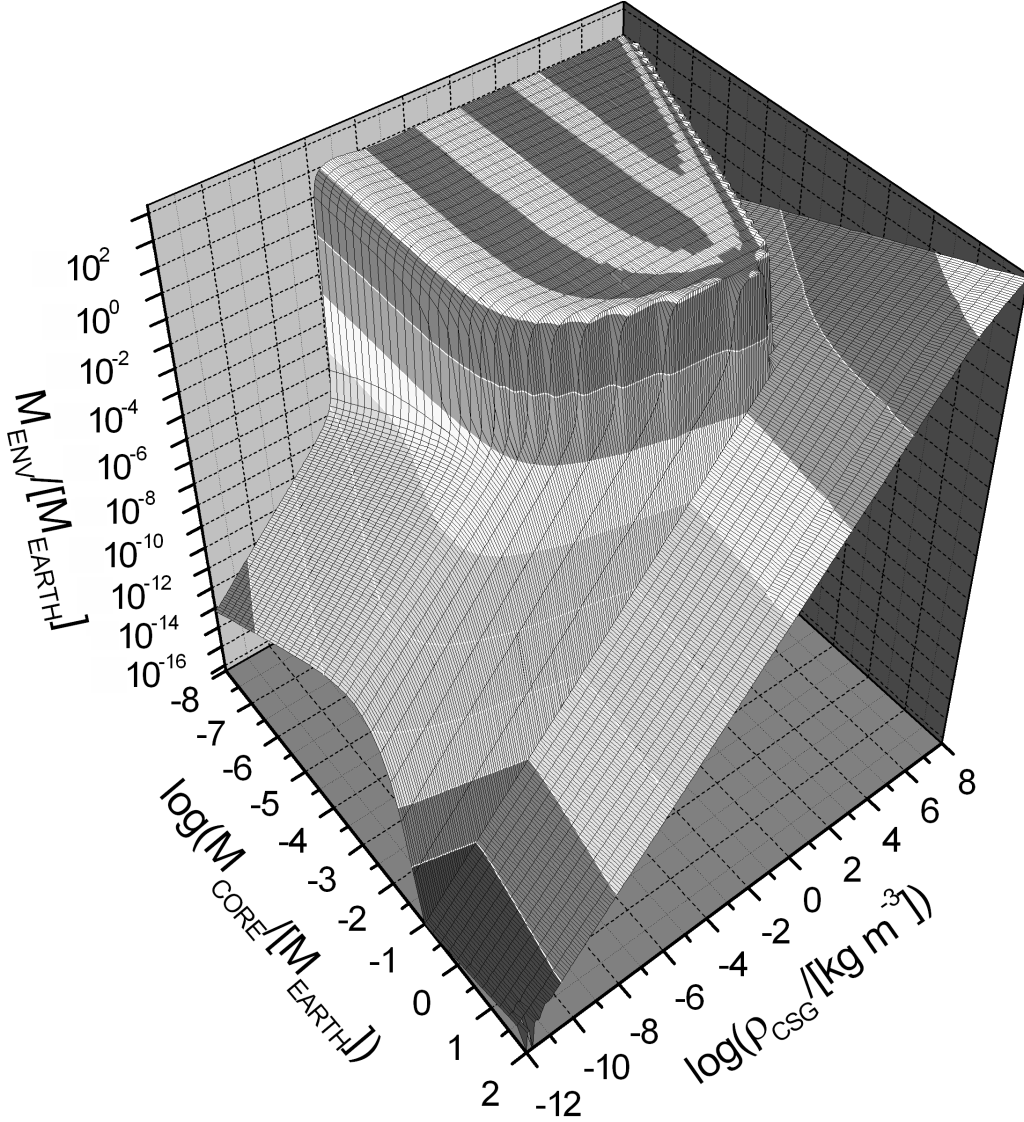


Figure 1.1: Envelope mass solution manifold. Environmental parameters for this manifold are set to $a=5.2$ AU, and $T=123$ K. Each point on the surface gives the mass of the protoplanet's envelope for given M_{core} and gas density at core surface, ρ_{CSG} . Models with different initial parameters generally connect to different nebulae. Several different regions are easily discernible: I - flat slope with gradient of 1, for the region $[-1,2]$ in $\log M_{\text{core}}$ and $[-12,6]$ in $\log \rho_{\text{CSG}}$; II - flat slope with gradient of 0.5, roughly encompasses $[4-6,8]$ in $\log \rho_{\text{CSG}}$, and all $\log M_{\text{core}}$; III - 'base of the island', $[-8,-1]$ in $\log M_{\text{core}}$ and $[-12,-6]$ in $\log \rho_{\text{CSG}}$; IV - 'island', $[-8,-1]$ in $\log M_{\text{core}}$ and $[-6,4-8]$ in $\log \rho_{\text{CSG}}$ (cf. Fig. 1.2).

Table 1.1: Symbols

<i>Symbol</i> [†]	Meaning
a [AU]	orbital distance
$G = 6.67259 \cdot 10^{-11}$	gravitational constant
$\mu = 2.3 \cdot 10^{-3}$	mean molecular weight
M_{core}	predefined core mass
M_{env}	envelope mass
M_{tot}	total mass
$M(r)$	total mass interior to radius r
$M_{\odot} = 1.989 \cdot 10^{30}$	solar mass
$M_{\oplus} = 5.976 \cdot 10^{24}$	Earth mass
r_{core}	core radius
r_{Hill}	Hill sphere radius
$\mathfrak{R} = 8.31441$	molar gas constant
$\varrho_{\text{core}} = 5500$	predefined core density
ϱ_{csg}	envelope gas density at core surface
ϱ_{env}	envelope gas density
$T(a)$	nebula gas temperature

[†] SI units used unless otherwise specified

Integration is performed from the core surface to the Hill radius, using the Maple 6 software (e.g. Garvan, 2001), with the Fehlberg fourth-fifth order Runge-Kutta method.

1.3 Results

1.3.1 Solution Manifold

In order to cover as many hydrostatic solutions as possible, the system of equations 1.2.2, 1.2.3, and 1.2.4 is solved for a wide range of parameters M_{core} and ϱ_{csg} . The set of all solutions for this range constitutes the solution manifold. Figure 1.1 shows the solution manifold for a protoplanet whose orbital distance corresponds to the position of proto-Jupiter according to the Kyoto-model of solar system formation (Hayashi et al., 1985). The manifolds with orbital parameters (a, T) of proto-Neptune and proto-Earth have

Table 1.2: Manifolds

Orb. param. (a, T)	(1, 225)	(5.2, 123)	(30, 51.1)
$M_{\text{core,crit}}^{\text{MMSN}}/[M_{\oplus}]$	0.1524	0.0948	0.0335
$M_{\text{env}}^{\text{max}}/[M_{\oplus}]$	21	96	380

Critical core mass increases for smaller orbital distances because of (in order of importance): the higher gas temperature (cf. Sect. 1.3.8 and 1.3.10), the smaller Hill sphere (cf. Sect.1.3.8), and the higher densities of the reference nebulae (taken from the minimum mass solar nebula models of (Kusaka et al., 1970; Hayashi et al., 1985)).

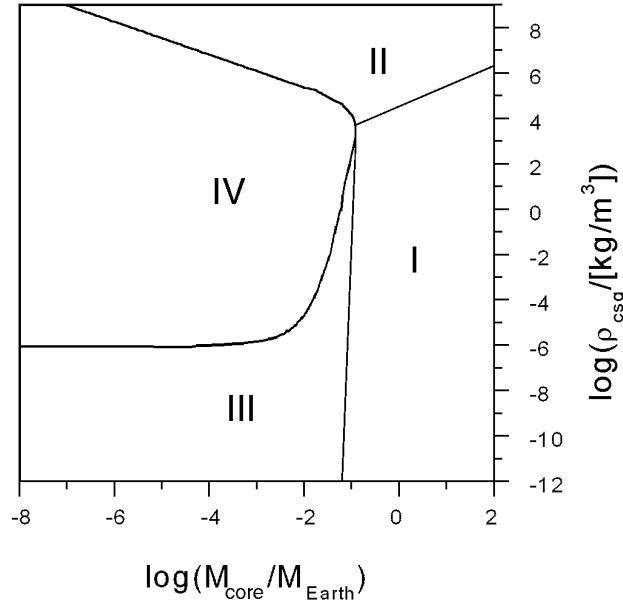


Figure 1.2: Manifold regions: I - compact non-self-gravitating envelopes, II - compact self-gravitating envelopes, III - uniform non-self-gravitating envelopes, IV - uniform self-gravitating envelopes. The border of the region IV somewhat depends on the choice of the surrounding nebula (cf. Fig 1.12); we use here a value from the (Hayashi et al., 1985) minimum mass solar nebula model.

similar morphologies. It should be reiterated that *the solution set contains all qualitatively different protoplanetary models* at a particular orbital distance; not just for a particular nebula, but for any nebula - from a dense gravitationally-just-stable clouds to a near-vacuum space.

1.3.2 Manifold Regions

Several distinct regions exist in the parameter space of the solution manifold (Fig. 1.2), and they can be examined from two complimentary perspectives. One way is to use gas density at the core surface, ϱ_{csg} , as an independent variable (eg. Fig. 1.3), and the other is to use the nebula gas density, ϱ_{out} (eg. Fig. 1.4). While ϱ_{out} is more physically intuitive, ϱ_{csg} maps out region IV of Fig. 1.2 more clearly, and is more efficient in terms of representing the entire manifold.

Figure 1.2 divides the solution manifold into four distinct regions, depending whether the solution is compact or uniform and self-gravitating or not. Figures 1.3 and 1.4 point to the existence of the four possible regimes for a planet;

1. *'mature telluric planet'* (region I): envelope mass is a linear function of ϱ_{out} , and ϱ_{csg} .
2. *'mature giant planet'* (region II): envelope mass weakly drops with ϱ_{out} ($M_{\text{env}} \propto \varrho_{\text{out}}^{-0.005}$).
 $M_{\text{env}} \propto \varrho_{\text{csg}}^{0.5}$ is weaker than for the *'mature telluric planet'* region. *'Nebula'* densities (ϱ_{out}) are so low that they may well be considered vacuous.
3. *'nebula'* (region III): envelope mass is a linear function of ϱ_{out} , and ϱ_{csg} .
4. *'protoplanet'* (region IV): envelope mass is a non-trivial function of ϱ_{out} or ϱ_{csg} .

Borders between regions are drawn using morphological features of the envelope mass properties - zero curvature (transition from positive to negative curvature) for border along the protoplanet region, and with $\partial M / \partial \varrho_{\text{cs}} = 0.75$ for the border between the two compact regions.

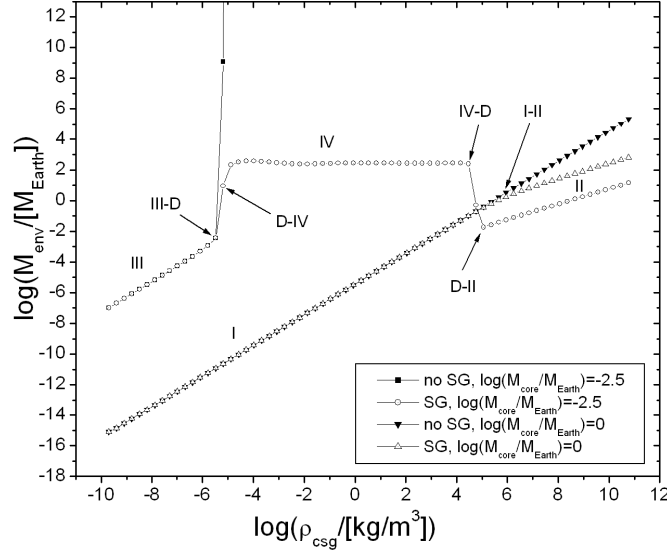


Figure 1.3: Demonstration of the self-gravitating effect for sub- and super-critical cores: comparison of cuts through two manifolds - with- ($M = M(r)$ in Eq. 1.2.3) and without- ($M = M_{\text{core}}$) the envelope's gravitating effect, each for two core masses. Cuts are for $a = 30$ AU and $T = 51.1$ K. Circles and squares represent the envelope mass of the subcritical core, calculated for $M = M(r)$ and $M = M_{\text{core}}$ in Eq. 1.2.3, respectively. White and black triangles have the same meaning but for the supercritical core. Labels without arrows correspond to manifold regions from Fig. 1.2, while labels with arrows mark interfaces between regions. D corresponds to the 'divergent wall' which surrounds region IV (cf. Fig. 1.1). Self-gravitating envelopes with $M = M(r)$ in Eq. 1.2.3 equation have a larger envelope mass than the corresponding envelopes with $M = M_{\text{core}}$ in Eq. 1.2.3 (cf. Fig. 1.6).

1.3.3 Self-Gravity Effect

The key effect, which is responsible for the manifold morphology as observed in Fig. 1.1, can be described as a self-gravity of the protoplanet's envelope. Keeping in mind the hydrostatics of the model, and the fact that the surrounding nebula is not prescribed, one can see that *self-gravity reduces envelope mass for given core surface pressure*, i.e. envelope mass would be larger if there were no self-gravitating effect (Fig. 1.3).

The envelope's radial gas density profile is shaped through the interplay of inward gravitational force and outward gas pressure. If the envelope mass is small compared to the core mass, gravitational force can be approximated as arising from the core's gravitational potential only. Once the envelope mass is comparable to (or greater than)

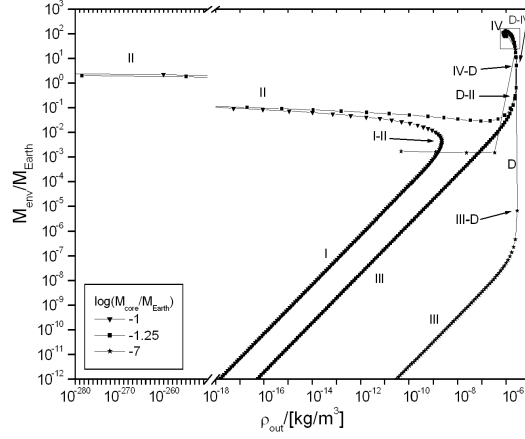


Figure 1.4: Envelope mass as a function of the nebula density ρ_{out} . Labels are the same as in Fig. 1.3. Lines connect states with increasing ρ_{csg} . Note the strong dependence of ρ_{out} on the envelope mass, and a non-trivial behavior of the $M_{\text{env}}(\rho_{\text{out}})$ for the region IV (enlargement in Fig. 1.5).

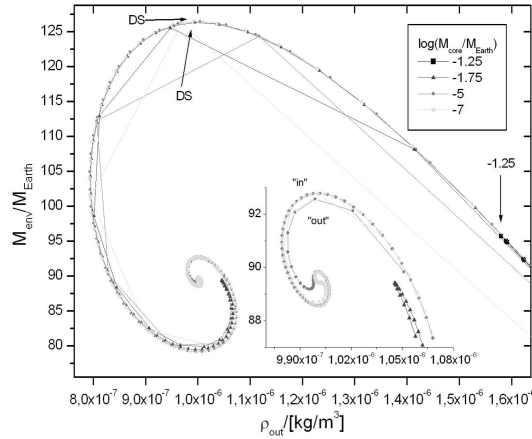


Figure 1.5: Enlargement of the boxed region of Fig. 1.4, isothermal curl regularized with the finite-density core; ‘-1.25’ - black squares represent protoplanets with first subcritical M_{core} line on the mesh of Fig. 1.1 and arrow points at the black square with highest M_{env} , DS - two protoplanetary states with the largest envelope mass in the manifold, but with typically very different ρ_{csg} (cf. Sect. 1.3.9); *in* and *out* curves are the consequence of the core. The smaller the core, the closer the *in* and *out* curves are. Figure is corresponding to a V-U plane for the protoplanets (see Sect. 1.3.5 for further discussion).

the core mass, they both contribute to gravitational potential, making its gradient steeper and, in effect, reducing the envelope mass. As a consequence, the self-gravitating envelope connects to a nebula different than the one which is in balance with the envelope in the absence of the self-gravitating effect. Further discussion of the role of self-gravity can be found in Sect. 1.3.5.

1.3.4 Two types of envelope equilibria

The solution manifold (Fig. 1.2) contains two basic types of envelope equilibria (Fig. 1.6):

1. *uniform*, or quasi-homogenous envelope: density of the envelope gas drops weakly with increasing radial distance, keeping the distribution of mass more or less uniform throughout the entire envelope; $\partial M_{\text{env}}/\partial r_{\text{out}} > 0$
2. *condensed*, or quasi-compact envelope: typically small, but very dense gas layer is wrapped around the core, at larger radii further out gas density is very low; $\partial M_{\text{env}}/\partial r_{\text{out}} \approx 0$

This is reminiscent of a similar equilibria, found by (Stahl et al., 1995), for constant mass coreless 'Van der Waals' gas spheres.

If an envelope's mass is much smaller than the core mass, the radial profile of gas density is simply an exponential function, well approximated by :

$$P(r) = P_0 \exp\left(-\frac{\mu}{\mathfrak{R}T} GM(r)\left(\frac{1}{r_{\text{core}}} - \frac{1}{r}\right)\right). \quad (1.3.1)$$

If $(M(r) - M_{\text{core}}) \ll M_{\text{core}}$, then Eq. 1.3.1 reduces to the barometric formula.

1.3.5 Differences: Isothermal Coreless Gas Spheres vs. Isothermal Protoplanets

The curl in Figs. 1.4 and 1.5 is reminiscent of a similar feature found for the isothermal coreless ideal-gas spheres (e.g. Schwarzschild, 1958, §13) represented in the U-V plane.

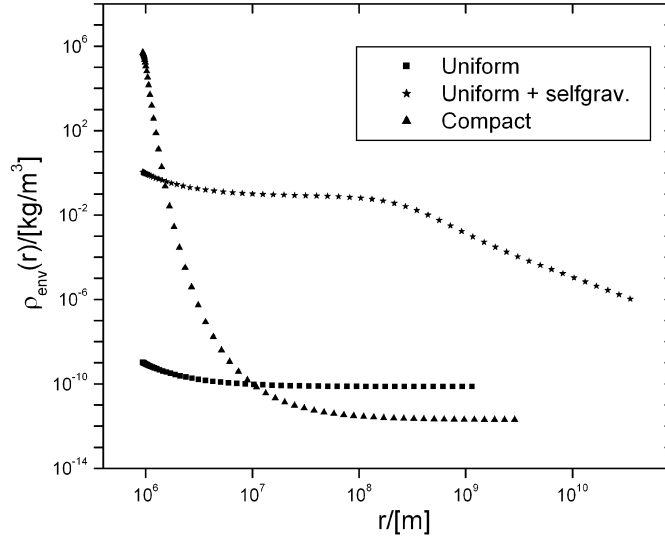


Figure 1.6: The uniform, compact and self-gravitating profiles. The uniform self-gravitating profile resembles the non-self-gravitating one until the envelope mass becomes comparable to the core mass. At this part the density profile changes to $\rho_{env}(r) \propto r^{-2}$.

Similarity follows from the definition of U and V quantities:

$$U = \frac{r}{M(r)} \frac{dM(r)}{dr} = \frac{4\pi r^3 \rho}{M(r)} = 3 \frac{\rho}{M(r)/(\frac{4}{3}\pi r^3)} \quad (1.3.2)$$

$$V = -\frac{r}{P} \frac{dP}{dr} = \frac{\rho}{P} \frac{GM(r)}{r} = \frac{3}{2} \frac{GM(r)/r}{P/\rho} \quad (1.3.3)$$

and from the fact that the mean density of the total object for our model is always the same, as implicitly defined through Eq. 1.2.1.

Unlike the singular isothermal sphere - with an infinite pressure at the center, our protoplanetary model has a solid core of uniform (and finite) density at its center. This will result in the departure from the potential of the coreless isothermal sphere - instead of $\rho(r) \propto r^{-2}$ structure, the envelope gas close to the core surface will obey a form of barometric law (c.f. Eq. 1.3.1).

If the mean envelope density at lower stratifications is comparable to the the core density, an ‘effective’ core will shorten the characteristic length-scale of the potential, making the exponential profile of the barometric-law-like profile even steeper. For the appropriate effective core, the outer stratifications will exactly match the outer stratifications of the solution which has the gas density at the core surface much smaller than the core density

(cf. Fig. 1.14). Those profiles will connect to the same nebula density, but will have a slightly different envelope mass, due to the difference in the profile of the inner stratification. Therefore, a curl from Fig. 1.5 will have two branches - ‘in’ (the solution with a non-self-gravitating inner stratification) and ‘out’ (the solution with an effective core).

The smaller the core mass, the sooner will the profile connect to the ‘ r^{-2} ’ structure, thus smaller the difference in the envelope mass between the pairs of solutions, and the closer will ‘in’ and ‘out’ branches in Fig. 1.5 be.

The fall off of gas density with increasing radius in the self-gravitating part of the envelope can be approximated by $\rho_{env}(r) \sim r^{-2}$ (cf. Fig. 1.6, self-gravitating profile), as expected in the theory of stellar structure for a self-gravitating isothermal sphere of ideal gas (e.g. Shu, 1992, § 18). Small deviations from r^{-2} are due to the finite amount of mass needed for the envelope to become self-gravitating, which produces a slight imbalance between the self-gravity and the amount of mass $M(r)$. No similar effect is observed for coreless, isothermal gas spheres (Stahl et al., 1995).

Depending on the fraction of the self-gravitating part of the envelope and of the core mass, this wavelike deviation can extend to the outer boundary, or can be attenuated deep within the envelope.

1.3.6 Estimating the Applicability of the Ideal Gas

We made two major assumptions while constructing our model - that the gas is ideal, and that the heat is instantaneously radiated away, i.e. the gas is isothermal. In Sect. 1.3.7 we examine the isothermal assumption, and we deal with the ideal gas in this section.

In order to keep the protoplanet in an equilibrium with the surrounding nebula, we have set the envelope gas temperature equal to the nebula temperature for the appropriate orbital distance. Therefore, we compare different equations of state at the envelope temperature. In addition to ideal gas, we take (Saumon et al., 1995) EOS, (Carnahan and Starling, 1969) EOS, as well as the completely degenerate electron gas.

Figure 1.7 shows that for the gas densities up to about 40 kg m^{-3} , ideal gas, Saumon-Chabrier-van Horn, and Carnahan-Starling EOS agree to better than a percent. For higher densities Saumon-Chabrier EOS shows additional non-ideal effects, while Carnahan-Starling EOS exhibits similar behavior for densities larger than 200 kg m^{-3} . We can also see that the electron degeneracy does not contribute to the pressure at least till the point where Saumon-Chabrier EOS departs from ideal-gas behavior.

However, in general we see that the ideal gas is an excellent approximation for our model, for the better part of the envelope gas density range. Certainly, there are also models where densities are high enough for significant non-ideal effects, but typically for the protoplanets in our model those high density envelope regions are restricted to areas close to the core, while the rest of the envelope will be well approximated with the ideal gas. We can see on Fig. 1.8 that if we use e.g. Carnahan-Starling EOS, numerical details will be changed, but the qualitative picture will remain the same. This is also true for Saumon-Chabrier EOS, which is work in preparation by C. Broeg. The ideal isothermal gas will not be a good approximation for the compact envelopes, which are typically associated with the giant planets in the late stages of their evolution. Using our model, we can show that a protoplanet will have a compact envelope under certain conditions. What we can not do with this model is to obtain a quantitatively correct picture of such a compact envelope.

Additionally, Fig. 1.14 shows why the choice of EOS is not critical for the qualitative picture: Although the non-ideal effects might change the density stratifications of the compact inner parts, each solution which is not self-gravitating in its inner (barometric-law like) part, will have a counterpart solution with an effective core. Properties of the effective core will be dictated by the EOS, but its effect on the scale-height will remain the same.

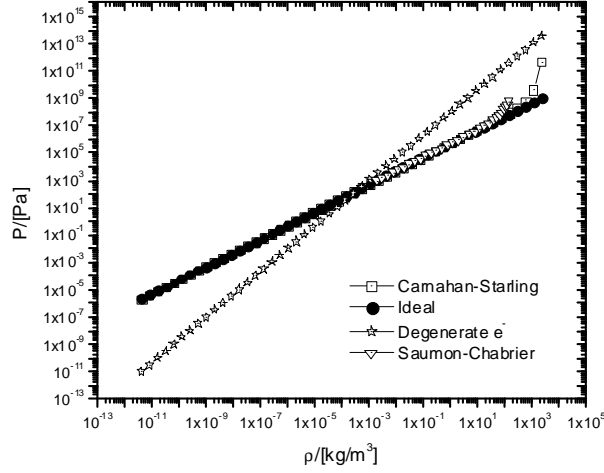


Figure 1.7: Pressure as a function of density, for $T = 123$ K. Black circles represent the ideal gas, squares are for the Carnahan-Starling EOS, and triangles are for the Saumon-Chabrier EOS. This figure also shows that the completely degenerate electron gas (stars) is not a good assumption for this (ρ, T) parameter range.

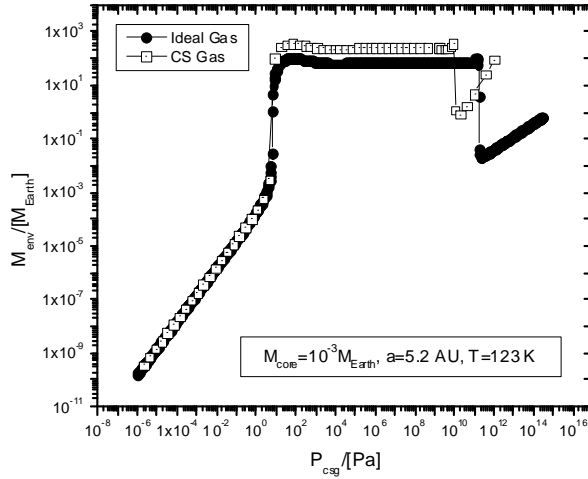


Figure 1.8: Cut through the envelope mass manifold, for a $10^{-3}M_{\oplus}$ core, $a = 5.2$ AU, and $T = 123$ K. Black circles represent the ideal gas, and squares are for the Carnahan-Starling EOS.

1.3.7 Estimating the Applicability of the Isothermal Assumption

In the previous section we showed that ideal gas is a good approximation for most of the parameter range we use. The validity of the isothermal assumption is examined below.

By analogy with the pressure scale-height, a temperature scale-height of a radiative stratification can be defined as:

$$H_T = \frac{H_P}{\nabla_{\text{rad}}} = -\frac{\partial r}{\partial \ln T} \quad (1.3.4)$$

where

$$H_P = -\frac{\partial r}{\partial \ln P} = \frac{P}{\rho} \frac{r^2}{GM(r)} \quad (1.3.5)$$

for ideal gas and hydrostatic equilibrium, and

$$\nabla_{\text{rad}} = -\left. \frac{\partial \ln T}{\partial \ln P} \right|_{\text{rad}} = \frac{3 \kappa L P}{4 \pi a c G M(r) T^4}, \quad (1.3.6)$$

where a is the radiation constant, κ is the gas opacity taken to be $0.1 \text{ m}^2 \text{ kg}^{-1}$, c is the speed of light, and L is the core luminosity due to the planetesimal accretion rate of $10^{-6} M_{\oplus} \text{ yr}^{-1}$.

The temperature scale-height corresponds to the length-scale of a radiative giant-protoplanet over which the envelope temperature drops by a factor of $1/e$. The specific temperature scale-height $H_T(r)/r_{\text{Hill}}$ evaluates the ratio of the thermal length-scale to the radial extent of the entire protoplanetary envelope, at a position r . Evaluated at $r = r_{\text{Hill}}$, $H_T(r_{\text{Hill}})$ is the global estimate of the thermal scale-height of the protoplanet. Figure 1.9 shows that the isothermal assumption is valid for large portions of the manifold regions III and IV (cf. Fig. 1.2), where $H_T(r_{\text{Hill}})/r_{\text{Hill}}$ has values much larger than unity. These envelopes have a relative thermal scale-height above unity for at least the outer 90% of the envelope. Therefore, even though the small innermost envelope region is probably non-isothermal,

the protoplanet should be well represented by the isothermal gas.

Close to giant-protoplanet's critical core mass (e.g. $\log M_{\text{core}} = -1.25$ in Fig. 1.4), $H_{\text{T}}/r_{\text{Hill}}$ is expected to be of order unity and the isothermal assumption breaks down. Compact solutions (regions I and II from Fig. 1.2, and high ρ_{csg} solutions in Fig. 1.9) have very large $H_{\text{T}}/r_{\text{Hill}}$, indicating that nearly vacuous space, around the compact envelope, is nearly isothermal. Detachment from a protoplanetary nebula could represent either hydrodynamically active protoplanets, or the collapsed gas giants with cleared protoplanetary nebula (i.e. mature giant planets). In both cases objects are expected to be deep in the non-isothermal regime. The radial profiles of the compact objects will change if a detailed energy transport is included, but they will nevertheless remain compact. A comparison of the Jupiter's radius with the one of our model planet's (of equivalent mass and T_{env} of 5000 K, estimated to be representative of Jupiter's average temperature from (Guillot, 1999) shows that, with $r_{\text{compact}} = 6.63 \cdot 10^7$ m, our model falls short less than 10% of reproducing the radius of the real gas giant.

In the context of Jupiter's potentially rapid formation (order of 10^6 years), it could be argued that the core accretion rate should be even higher. However, $H_{\text{T}}/r_{\text{Hill}}$ is proportional to the inverse of \dot{M}_{core} , and even if it is set to $10^{-5} M_{\oplus} \text{ yr}^{-1}$, the validity of the isothermal assumption is still appropriate for the regions III and IV of Fig. 1.2. Indeed, such high core accretion rates are applicable for cores comparable to M_{\oplus} (i.e. cores at late stages of giant-protoplanet's evolution), and are surely an overestimation for the younger cores (e.g. for the cores of $10^{-3} M_{\oplus}$), making the case for the isothermal regime even more solid. However, because of the simplicity of our model, the results are only qualitative, while quantitatively correct values would only be accessible through a more elaborate model.

$H_{\text{T}}/r_{\text{Hill}}$ shows that close to the critical core mass, there are non-isothermal effects.

But the basic isothermal picture is valid for most of (quasi-homogenous part of) the manifold. It even appears that the possible transition from homogenous to compact state can be initiated within the isothermal regime.

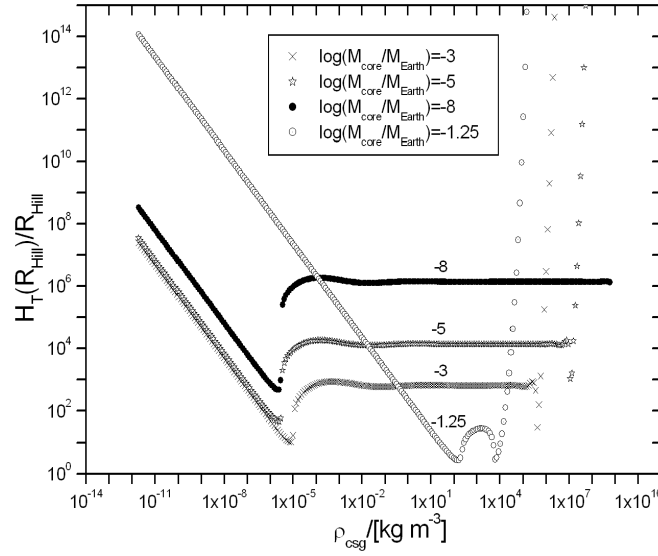


Figure 1.9: Specific temperature scale-height as a function of the density at the core surface, for different subcritical core masses. Protoplanetary models with cores of -8 (black circles), -5 (stars), and -3 (crosses) in logarithmic M_{\oplus} units have $H_T(r_{\text{Hill}})/r_{\text{Hill}}$ much larger than unity. This justifies the isothermal assumption for the manifold regions III and IV.

1.3.8 Manifolds and Environment

Manifold solutions are dependent on four environmental parameters: the gas temperature T of the protoplanet (and of the surrounding-nebula), the orbital distance a from the parent star, the mean molecular weight μ , and the mass of the parent star M_{\star} . These parameters influence the balance of the two forces that determine the radial density structure - the outward force arising from the gas pressure, and the inward gravity force; T and μ are connected with pressure through Eq. 1.2.4, while a and M_{\star} determine the Hill-sphere, i.e. the volume of the envelope mass.

Due to the simplicity of the model, the impacts of T and μ on the solutions will be discussed together, as will the influence of a and M_{\star} . In reality, these parameters will have very different impacts.

Unless otherwise specified, the reference parameters throughout the current section are: $\log(M_{\text{core}}/M_{\oplus})=-5$, $a = 5.2$ AU, $T_{\text{env}} = 123$ K, and $\mu = 2.3 \cdot 10^{-3}$ kg mol $^{-1}$.

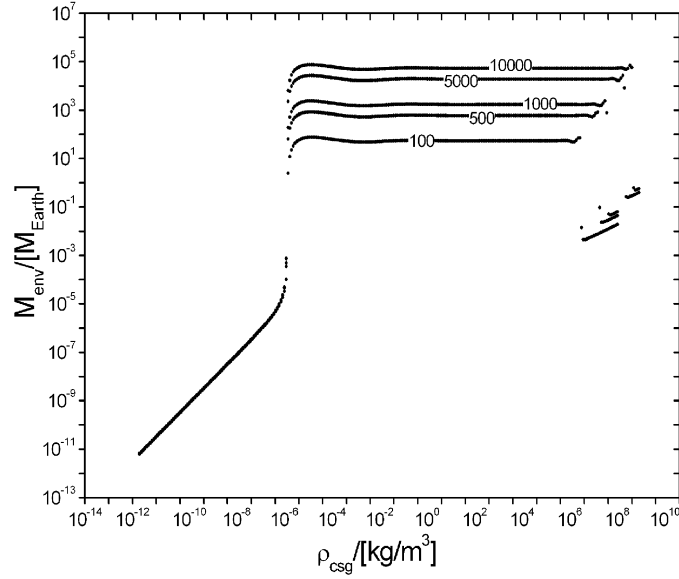


Figure 1.10: Envelope mass solutions as a function of gas density at the core surface, for gas temperatures of 100, 500, 1000, 5000, and 10000 K. Change of T has no influence on the envelope mass of the non-self-gravitating regions, while same change of T will produce a significant effect for protoplanets in self-gravitating regions.

Temperature and Mean Molecular Weight

Although *this* model is isothermal, the choice of gas temperature influences the solution manifold quantitatively. From Eq. 1.2.4 it is clear that pressure relates linearly to temperature. Since the pressure force counterbalances the gravitational force, protoplanets with hotter envelopes require more gravity (and thus more mass) to have a hydrostatic solution. The value of the critical core mass is a good example of the quantitative influence of temperature. For example, the critical core mass for a 123 K protoplanet in Jupiter's orbit is $0.0948 M_{\oplus}$, while the critical core mass value for a 5000 K case is $24.5 M_{\oplus}$.

Figure 1.10 shows that, for subcritical cores and small gas densities at the core surface (region III in Fig. 1.2), gas temperature has virtually no impact on envelope mass. Since the envelope mass is small compared to the core mass, the envelope parameters (e.g. T_{env}) have no influence on the hydrostatic force balance via gravity feedback. On the contrary, for envelopes in which self-gravity shapes the radial structure (regions IV and

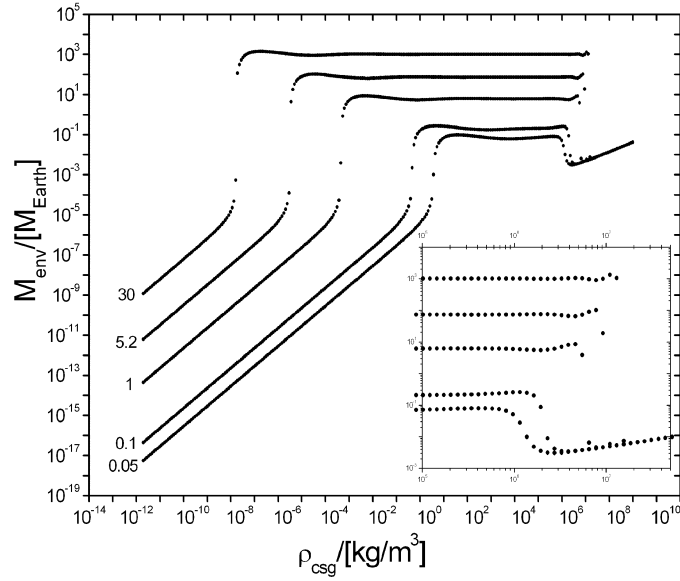


Figure 1.11: Envelope mass solutions as a function of gas density at the core surface, for orbital distances of 0.05, 0.1, 1, 5.2, and 30 AU. Enlargement: Transition from uniform to compact envelope solutions is more abrupt for protoplanets at large orbital radii. This is a consequence of larger Hill-sphere for outer protoplanets.

II in Fig. 1.2), the envelope mass is significantly affected by different T_{env} .

The scaling law which relates manifolds of various temperatures is discussed in Sect. 1.3.10. As previously mentioned, this simple model does not incorporate an energy transport equation, nor does it account for the gas and dust opacities. Therefore, a change in μ can not be distinguished from the corresponding change in T , and will not be further discussed.

Orbital Distance and Star Class

Orbital distance, together with the masses of the protoplanet and the parent star determine the protoplanet's gravitational sphere of influence, the so called Hill-sphere. Since the available volume for the protoplanet's envelope scales with the cube of the orbital distance (see Equ. 1.2.1), the strength of the envelope's self-gravitating effect depends critically on the distance from the core to the parent star (see Fig. 1.11). Therefore, in order for the inner protoplanets to have (at least partly) self-gravitating envelopes, the gas

density at the core surface must be larger than for the corresponding outer protoplanets. For solutions with compact envelopes (right side of Fig. 1.11 and enlargement) the orbital distance has no impact on the envelope mass, since the radii of the compact inner part are typically several orders of magnitude smaller than their respective Hill-spheres.

The transition from a uniform self-gravitating to a compact envelope is characterized by a considerable drop in the gas density for the outer envelope stratifications. In addition, protoplanets close to the parent star have relatively small Hill-radii and most of the envelope mass can be found in the core proximity. Therefore, the transition from uniform to compact envelope for protoplanets close to the parent star is less abrupt than for more distant protoplanets, as can be seen in the enlargement of Fig. 1.11.

Varying the mass of the parent star is equivalent to changing the orbital distance of the protoplanet, provided that the gas temperature stays the same. It follows from Eq. 1.2.1 that $\delta a^{-3} = \delta M_{\star}$, e.g. changing the orbital distance of the protoplanet from 5.2 AU to 1 AU is equivalent to changing the mass of the parent star from $M_{\star} = 0.21 M_{\odot}$ to $M_{\star} = 30 M_{\odot}$. It remains to be seen if this equivalence will hold for a more complex model, because the nebula properties will likely change in accordance to the known mass-luminosity relation as M_{\star} is varied.

1.3.9 Static Critical Core Mass

There are several definitions of the critical core mass currently in use. The critical core mass concept has been introduced by various investigators (e.g. Perri and Cameron, 1974; Mizuno et al., 1978; Mizuno, 1980; Bodenheimer and Pollack, 1986; Wuchterl, 1991a). As a starting point, we choose here a definition suggested by (Wuchterl, 1991a), for 'static critical core mass': *No more static core-envelope models with increasing core mass exist at the critical mass.*

This definition is valid along a (time) sequence of protoplanetary models with increasing M_{core} . It is only along such a sequence, in the context of the static models, that a time

evolution with growing cores can proceed. Essentially, the static critical core mass is the largest core mass for a static protoplanet that can be embedded in a given nebula, characterized by a nebula gas density, a temperature, and a distance from a parent star. For the ($a = 5.2$ AU and $T = 123$ K) manifold this means that, among the solutions with $\rho_{env}(r_{Hill}) = 1.4 \cdot 10^{-8} \text{ kg m}^{-3}$ (defined for the minimum mass solar nebula, (e.g. Hayashi et al., 1985), the solution with the largest core mass determines the static critical mass (Fig. 1.12, the innermost solid line). This gives static critical core mass of $M_{core,crit}^{MMSN} = 0.0948 M_{\oplus}$.

Figure 1.12 shows that the value for critical core mass exhibits a generally weak dependence on the density of the surrounding nebula, so the choice of ρ_{out}^{MMSN} from different nebula models is not critical. For the very dense nebulae (around $10^{-6} \text{ kg m}^{-3}$) and depending on the choice of the solution branch (cf. Sect. 1.3.9), the values for the local critical core masses can span several orders in magnitude even for the same nebula.

The critical core masses for different manifolds are presented in Table 1.2, and are found to depend on the parameters that affect hydrostatic balance (cf. Sect. 1.3.8).

By comparing the Figs. 1.1 and 1.2 it follows that the natural choice for the *global static critical core mass*, one which is valid for the whole manifold, should be the core of the protoplanet which is at the interface of all four manifold regions (c.f. Fig. 1.2). The model at the interface has a minimum in the envelope mass, for a manifold cut along the constant ρ_{csg} value. The interface is also an inflection point, for a manifold cut at a constant M_{core} . The conditions for the *global static critical core mass* thus are:

$$\begin{aligned} \frac{\partial M_{env}}{\partial M_{core}} &= 0 & \frac{\partial^2 M_{env}}{\partial M_{core}^2} &> 0 \\ \frac{\partial M_{env}}{\partial \rho_{csg}} &= 0 & \frac{\partial^2 M_{env}}{\partial \rho_{csg}^2} &= 0 \end{aligned} \tag{1.3.7}$$

Since the numeric values for the global critical core masses are very close to the values of the critical core masses from the definition suggested by (Wuchterl, 1991a), we do not present the global numerical values separately.

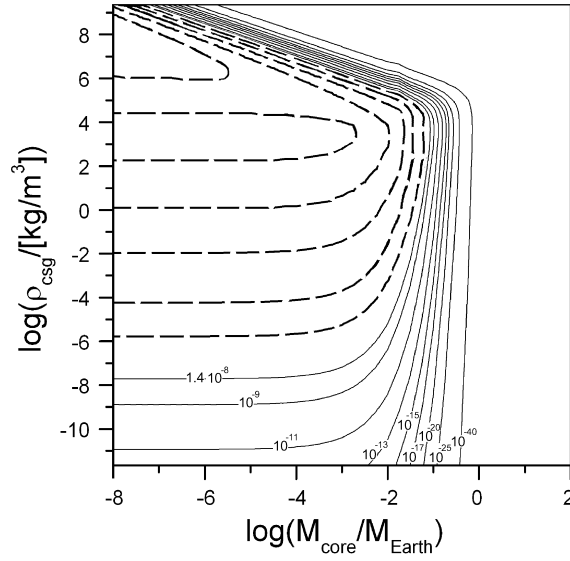


Figure 1.12: Solution branches - isobars for $\rho_{env}(r_{Hill}) = \rho_{out}$ - for ($a = 5.2$ AU and $T = 123$ K) manifold: standard solar nebula solution branch is represented by innermost solid line; an enhanced nebula with the $\rho_{out} = 10^{-6} \text{kg m}^{-3}$ nebula (dashed lines) has multiple solution branches; each solution branch has its own maximum core mass, hence, local critical mass

The values obtained for critical core masses in this model agree well with those of Sasaki (Sasaki (1989)), who used a similar set of assumptions. However, such isothermal values are significantly smaller than today's commonly accepted critical mass values, obtained with inclusion of detailed energy transfer, that are typically between 7 and 15 M_{\oplus} . The reasons for this are two-fold. Firstly, we use the equation of state for ideal gas. Secondly, the temperature of the isothermal gas is taken from nebula models, hence the nebula temperature is the temperature of the entire protoplanet. This is certainly a lower limit for the realistic temperature of the interior of the protoplanet. Larger critical core mass values are obtained if the gas temperature is in the range of the temperatures for the interior of gas giants modelled with detailed energy transfer (cf. Sect. 1.3.8). Clearly, the correct determination of critical core mass requires temperature structure, but emphasis in this work was not on quantitative details, but rather on global qualitative features.

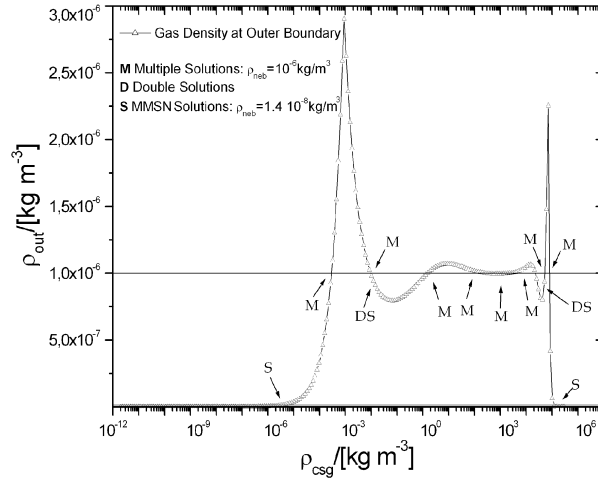


Figure 1.13: For nebula density enhanced relative to minimum mass solar nebula, even more than two hydrostatic equilibria could exist; *M* - protoplanetary solutions with $\log M_{\text{core}}/[M_{\text{Earth}}] = -2$ that fit into $\rho_{\text{out}} = 10^{-6} \text{ kg m}^{-3}$ nebula; *DS* - double solutions - special case of multiple solutions, cf. Figs. 1.5 and 1.15; *S* - protoplanetary solutions with same core, whose envelope fits into minimum mass solar nebula.

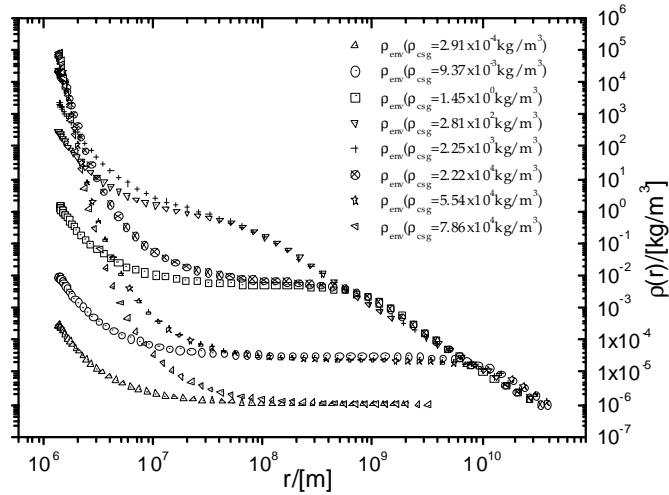


Figure 1.14: Density profiles for the solutions which fit into the same ($10^{-6} \text{ kg m}^{-3}$) nebula. These solutions are labelled with *M* in Fig. 1.13.

Local Critical Core Mass

From Figs. 1.12 and 1.13 one can see that, for each subcritical core immersed in a nebula, there are at least two solutions permitted. However, if one considers only the time-sequence of hydrostatic models with a growing core, it is clear that solutions with higher density at the core surface can not be reached.

The situation is more complicated if the protoplanet is embedded in a denser protoplanetary nebula. Our model clearly predicts multiple solutions for certain sets of parameters (Fig. 1.13). Instead of one solution-branch for a given nebula cloud (with two solutions for each core, as for a minimum mass solar nebula), several solution-branches are possible, again each with two solutions for a specific core (Fig. 1.12, dashed solution branches for $\rho_{out} = 10^{-6} \text{ kg m}^{-3}$). Multiple solution-branches are enabled by envelope self-gravity (cf. Fig. 1.14) and are due to tidal restrictions imposed by the parent-star via r_{Hill} (cf. Fig. 1.3, region IV).

Each solution-branch has one critical core mass, beyond which there is no static solution, for a sequence of hydrostatic models with increasing core mass. For the minimum mass solar nebula this means one critical core mass, in the way critical core mass was suggested by (Wuchterl, 1991a). For some denser nebulae, however, the existence of several branches implies several - *local* - critical core masses, where solutions beyond the critical core mass of the branch are unavailable *locally*. After reaching the local critical core mass, the planet could, in principle, continue evolution by ‘jumping’ to another branch. Similar behavior, for certain sets of initial parameters, is observed by one of us in hydrodynamical models. The local critical core mass satisfies the above definition but not Eq. 1.3.7 for the global critical core mass.

Double Maxima

A special case of multiple solutions can be seen in Figs. 1.5, 1.13, and 1.15 as double peaks in envelope mass. For every (subcritical) core, two special solutions, which fit into the same nebula cloud (i.e. have same $\rho(r_{\text{Hill}})$) and have almost exactly the same envelope mass (equal to one part in 10^4 , or better), are found to exist. Usually these two solutions have a very similar stratification in the outer parts of the protoplanet’s envelope, but deep inside the protoplanet their radial structure is quite distinct (cf. Sect. 1.3.5).

Supercritical (*in the newly proposed, global sense*) cores do not possess such a feature,

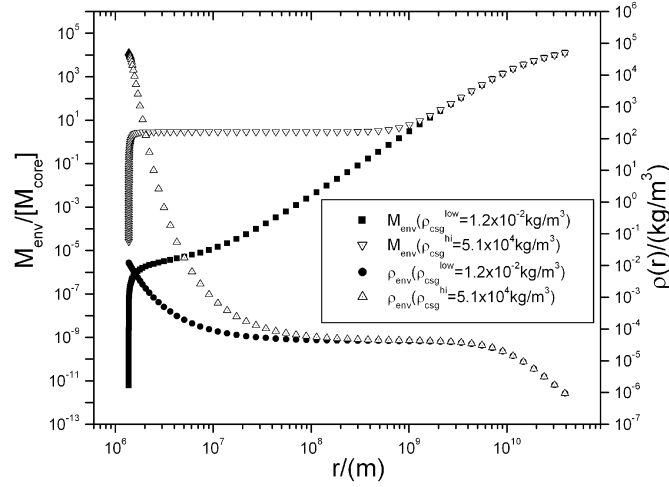


Figure 1.15: Mass and density radial structure of the special case of multiple solutions, where two protoplanets have same core, almost same envelope mass, connect to same nebula, but have different radial structure. These solutions are labelled with DS in Fig. 1.13.

because density profile *always* effectively goes to zero long before Hill radius is reached. Therefore there is no significant contribution to the envelope mass in the outer stratifications, and envelope mass increases monotonically with gas density at core surface (cf. Fig. 1.3).

Envelopes with lower gas density at core surface, $\varrho_{\text{csg}}^{\text{low}}$, (Fig. 1.15) have a maximum possible mass (for the corresponding manifold) because the envelope gas density at the core surface is low enough to ensure uniformity for the major part of the radial structure. Consequently, envelope density does not substantially decrease from the core-surface value. At the same time, ϱ_{csg} is high enough to enable significant mass contributions from the outer parts of the envelope, where the volume (and therefore the mass, for a given density) per unit radius, is the largest. Values for such maximum envelope masses are tabulated in Table 1.2, page 13.

Envelopes with higher $\varrho_{\text{csg}}^{\text{high}}$ build up the self-gravitating effect (which starts as soon as $M_{\text{env}} \approx M_{\text{core}}$) very close to their core, i.e. within a r_{core} . Because of the very strong self-gravitating effect ($M_{\text{env}} \approx 3M_{\text{core}}$ for innermost regions), the radial density fall-off close to the core (Fig. 1.15) is strong.

A new, *effective core* is formed from the dense envelope-gas-layer wrapped tightly around the core. In this case, the envelope density distribution resembles one with the core (and the radius) of this effective core. In stratifications where the envelope mass becomes comparable to the effective core, another self-gravitating effect changes the radial envelope density distribution to $\rho_{\text{env}} \propto r^{-2}$.

For a particular choice of $\rho_{\text{csg}}^{\text{high}}$, the envelope density profile in outer stratifications matches that of $\rho_{\text{csg}}^{\text{low}}$, thus making the mass of both envelopes almost equal.

1.3.10 Temperature-Mass Invariance

It has been noted that, if mass and distance are measured in a system of appropriate units (i.e. mass in units of core mass, and distance in units of core radii), solution manifolds with different temperatures are almost identical, except for a shifting on a core-mass-axis, according to the relation:

$$\frac{T_1}{T_2} = \left(\frac{M_1}{M_2}\right)^{2/3} \quad (1.3.8)$$

that can be derived for homologous envelopes satisfying $\rho_1(r_1/r_{\text{core},1}) = \rho_2(r_2/r_{\text{core},2})$, for any pair of r_1 and r_2 such that $r_1/r_{\text{core},1} = r_2/r_{\text{core},2}$. In other words, the radial profile of a certain protoplanet with core mass M_1 and temperature T_1 will be the same as the radial profile of another protoplanet with core mass M_2 and temperature T_2 , if equation 1.3.8 is obeyed, and if mass is measured in units of core mass and length in units of core radii.

This is true for all manifold regions, sub- and super-critical, self-gravitating or not. Note that in Fig. 1.10 the non-self-gravitating region was not affected with change in envelope temperature, but relation 1.3.8 does hold even for non-self-gravitating envelopes, since it connects envelopes with different temperatures *and* core masses. Fig. 1.10 was plotted for different temperatures, but constant core mass.

1.3.11 Critical core and core density

It can be shown that the introduction of gravitational smoothing parameter in the disk-planet interaction type calculations (e.g. Kley, 1999; D'Angelo et al., 2002), or alternative procedure with the same effect, is equivalent to drastically reducing the core density.

A manifold with a reduced core density (a problem with 'soft' potential) has much higher critical core mass (of the order of $100 M_{\oplus}$ already for a smoothing parameter as small as $b \approx 0.1 r_{\text{Hill}}$!). Also, the transition between the envelope regions is smoother. On Fig. 1.16 we compare the envelope mass manifold for the models with realistic core density ($\rho_{\text{core}} = 5500 \text{ kg m}^{-3}$) with the analogue for the models with low core density ($\rho_{\text{core}} = 1.5 \cdot 10^{-4} \text{ kg m}^{-3}$), equivalent to the gravitational smoothing parameter $b=0.5$, used in most of today's disk-planet interaction type calculations (e.g. D'Angelo et al., 2003; Nelson and Papaloizou, 2004). Figures 1.12 and 3.28 show the same comparison for nebula density manifolds. Note that, for the low core density case, local critical core mass is a strong function of the nebula density!

Different manifold topography could greatly affect the (correctness of the) dynamics of the models in the disk-planet interaction type calculations. It is not apriori clear that computed cases are even in the qualitatively same dynamical regime, as the one in which would be models with correctly calculated gravitational potential¹.

1.4 Discussion and Conclusions

In an effort to obtain a global overview of hydrostatic protoplanetary equilibria, we have chosen a simple physical model so as to be able to clearly understand the interaction of competing processes.

Our use of relatively simple physics has several consequences; because the ideal gas equation of state is used, gas particles are 'soft', and can be compressed as much as is

¹In fact, in Sect. 3.4.3 we show that the dynamics of low- ρ_{core} manifold is *qualitatively* different from dynamics of realistic- ρ_{core} manifold

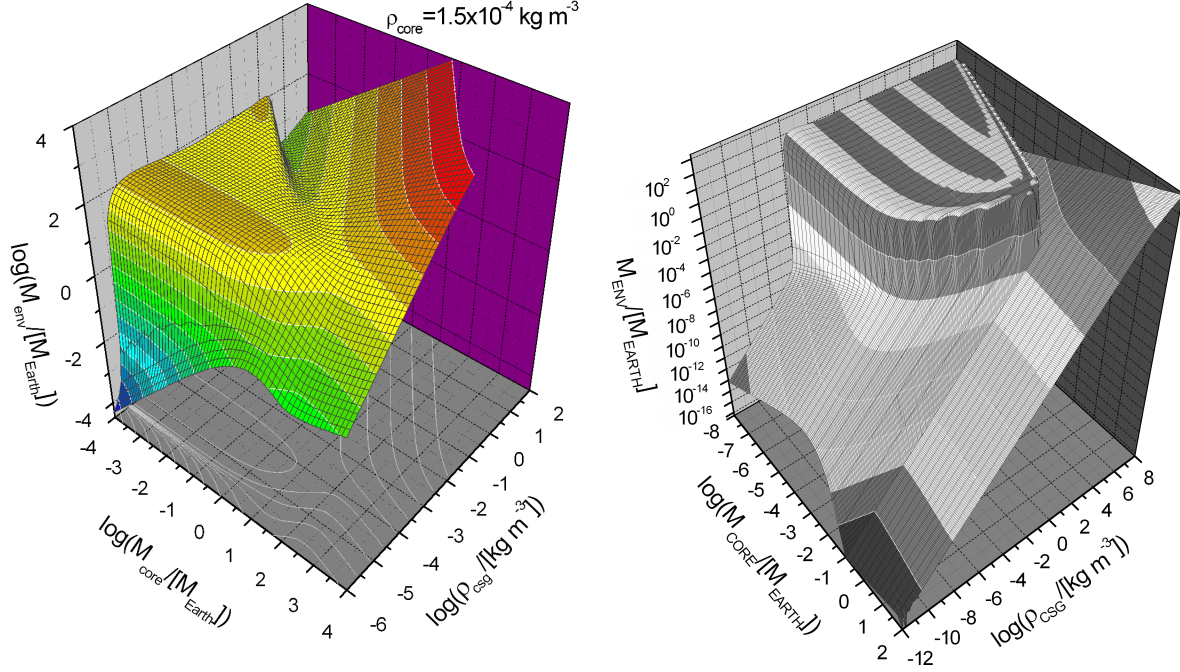


Figure 1.16: Comparison of the envelope mass manifolds for models with $\rho_{\text{core}} = 5500 \text{ kg m}^{-3}$ (right plot) and $\rho_{\text{core}} = 1.5 \cdot 10^{-4} \text{ kg m}^{-3}$ (the latter core density being a typical value used in the disk-planet interaction type calculations). Note the different manifold topography around the critical core mass (the ‘nose’ of the ‘island’), and the fact that for low core density manifold critical core mass is higher than $1000 M_{\oplus}$ (more than four orders of magnitude higher than for the manifold with the correct core mass!). Also compare nebula density manifolds, Fig. 1.12 with Fig. 3.28. Raw data for the low core density manifold courtesy of J. Schönke, AIU Jena.

needed, in effect overestimating the importance of gravity relative to gas-pressure, when large envelope-gas-pressure is applied. Comparison of the ideal gas EOS to the numerical Saumon-Chabrier EOS shows disagreement for the $\log T = 2.1$ isotherm and densities above $\rho = 40 \text{ kg m}^{-3}$. This would indicate that the non-ideal EOS for high-density effective-cores is needed.

It has been noted that manifold properties are insensitive to variation of orbital distance a or mass of the parent star M_{\star} , as long as $a M_{\star}^{-3} = \text{const}$ holds (cf. Sect. 1.3.8). Also, solutions whose envelope temperature and core mass are obeying relation 1.3.8 are found to be the same, if appropriate units for mass (i.e. core mass) and length (i.e. core radius) are used. This indicates the existence of analytic solutions for some envelope

regimes, through certain dimensionless scaling variables. Such a treatment is, however, out of the scope of the present work.

The envelope gas temperature is equal to the nebula T throughout the protoplanet, and that certainly underestimates the thermal pressure and hence reduces the values for the critical core mass. However, from Equ. 1.3.8, one can show that for a more realistic estimate of the envelope temperature representative for the young planets (5000 K) critical core mass values are overestimated ($\sim 24.5M_{\oplus}$), due to envelope isothermality/lack of an energy transport equation and use of ideal-gas EOS, when compared to canonical critical core mass values from protoplanetary models with detailed microphysics.

Both the local and the global critical core masses signal the end of the availability of the hydrostatic solutions, for given nebula conditions. In the case of the local critical core mass, non-availability holds for a small region of the parameter space around the local critical core mass, while for the global critical core mass this is true for every core larger than the critical core mass. The significant difference between the two types of critical core mass is that, at the global critical core mass (and above), the non-isothermal effects are crucial in shaping the structure of the protoplanetary envelopes, and are present throughout the parameter space. These non-isothermal effects are important for determining the details of the dynamical disk-planet interaction.

The critical core mass values obtained in this model are almost two orders of magnitude smaller than the canonical critical core masses which incorporate detailed energy transfer. Thus, if subcritical or just-critical regimes of a dynamical disk-planet interaction are to be investigated through a model that is locally isothermal, the planet mass should be appropriately set. Most of the present locally-isothermal disk-planet models (e.g. Kley, 1999; D'Angelo et al., 2002, 2003; Nelson and Papaloizou, 2004) operate with planets which *should be deep in the super-critical regime*.

A solution set from our model encompasses solutions that are reminiscent of the planets in the various stages of evolution (from the small rocks embedded in the dilute nebula to

the mature planets, as we know them), and of various configurations (the telluric planets of region I in Fig. 1.2, and the gas giants of region II). The 'nebula' and 'mature planet' regimes are the physically intuitive beginning and end phase of the planetary evolution. However, the 'protoplanet' regime presents us with an interesting region in the parameter space, where planet could make the transition from 'infancy' to 'maturity'. Depending on the detailed structure and the dynamics of the surrounding nebula, it is easy to conceive a standard scenario of the planet formation. That is, the accretion of nebula gas onto a supercritical protoplanet. Other scenarios could be imagined as well, e.g. a massive protoplanet could release a major part of its envelope to reach the appropriate equilibrium, or it could dramatically condense its otherwise mostly gaseous envelope. Amounts of the dust in the environment will doubtless play a very important role in the process.

In conclusion, several important features of the solution set have to be mentioned:

1. Two basic types of the envelope equilibria are found for protoplanets:

- *uniform*; the density of the envelope gas drops weakly from the core to the outer boundary
- *compact*; the dense gas layer forming an effective core, and a very low, exponentially decreasing, gas density further out

Both types can be self-gravitating or non-self-gravitating, dividing the solution manifold into four distinct regions.

2. As a consequence of the envelope's self-gravitating effect, a wide range of possible envelope solutions exists.

3. We have developed a new concept for the global static critical core mass, which marks the contact point of all four qualitatively different types of protoplanets. This concept is based on a qualitative change of the envelope properties while considering a complete set of available solutions (a solution manifold), as opposed to the critical

core mass definitions which are valid only for a solution subset fitting a particular nebula.

4. For every subcritical core there are at least two envelope solutions possible (a self-gravitating one and a non-self-gravitating one) for a given nebula, and for a certain nebula parameters the number of the possible envelope solutions can be even larger. Such nebulae also have multiple (local) critical core masses.
5. The global static critical core mass value is shown to decrease with the increasing orbital distance a , mainly because of the decrease in the temperature of the surrounding nebula.

Chapter 2

Planets and minor bodies

In this Chapter we discuss the low mass planetary boundary, a spin-off from the definition of the global critical core mass (see Sect. 1.3.9).

2.1 Low-mass planetary boundary

The number of known planets has increased by more than an order of magnitude within the last decade (for the current list see e.g. Jean Schneider's 'Extrasolar Planets Encyclopaedia'¹). However, additional planets brought in a diversity which has made task of defining *what is a planet* all the more difficult. Current working definition of the planet can be examined on the website of 'the Working Group on Extrasolar Planets'² of the International Astronomical Union.

During the course of our investigation, we have developed a concept for a global static critical core mass (c.f. Sect. 1.3.9). We make use of this concept to provide a planethood criterion to distinguish between a planet and a lesser body, such as a planetoid, or an asteroid. The following discourse should be valid upon assumption that the body in question fulfills the dynamical planethood criteria (i.e. it is the gravitationally dominant body in the orbit around a star or a stellar remnant).

¹<http://www.obspm.fr/encycl/encycl.html>

²<http://www.ciw.edu/IAU/div3/wgesp/>

We argue that an object should not be called a *planet* if it is not capable to retain its envelope in case it is connected to a vacuum (i.e. to an empty space, as opposed to the proto-planetary nebula gas cloud). Therefore, one of the characteristics that a celestial body must fulfill to be called a planet can be specified as:

A planet will have a core which is supercritical within the appropriate manifold³. A minor planet will have a subcritical core.

Supercriticality is used here in a reference to a *global static critical core mass*, as defined in Sect. 1.3.9. We go further, and define a '*giant planet*' as a supercritical core within the respective manifold for a solar (parent star) gas composition. On the other hand, a '*telluric planet*' should be supercritical within the respective manifold for a nitrogen atmosphere.

We have chosen nitrogen in the case of a telluric planet for several reasons, but we could have decided for some other gas with similar properties. Here we briefly present arguments for nitrogen. First and foremost, it is the principal ingredient of the first planet known to the (hu)mankind. Second, it is substantially heavier than hydrogen or helium, which appears to be a key property enabling a body significantly smaller than e.g. Saturn's core to retain a gas envelope in the open space. Third, the only two other bodies having atmosphere in the Sol system (excluding the giant planets, off-course) both have nitrogen in their atmospheres, giving (partial) atmospheric pressure similar to the one on Earth⁴.

³'manifold' is a complete set of equilibrium states relevant to the planetary environment

⁴Admittedly, Venus has carbon-dioxide as a main atmosphere constituent, but that could be due to the ongoing geological process. Besides, the molecular weight of carbon-dioxide is not very different from the molecular weight of nitrogen and thus would lead to similar classification.

2.2 Planethood affiliation in the solar system

Why Titan has smelly clouds while Rhea is just an ice-ball

The *planethood criterion* presented in the previous section, for a distinction between a planet and a minor planet, *should be valid generally*, even for a completely realistic (model-)planet, i.e. for a manifold constructed for any relevant physical planetary environment, including all relevant micro- and macro- physics. The last statement assumes that it is possible to define the critical core mass concept, for such a general manifold.

However, we argue that even an isothermal manifold, as defined in the previous Chapter, will be a decent model to distinguish a telluric planet from a planetoid, in case of the Solar system. The telluric planets are associated with relatively thin atmospheres for which an isothermal assumption is a reasonable approximation (within a study of general properties of the planet). Keeping in mind that the deviation from an isothermal approximation might somewhat change the value of the critical core mass (c.f. Sect. 1.3.10), we conclude that, within a factor of two, we can use an isothermal manifold as a probe for the telluric planet criterion in the Solar system.

At relevant isothermal manifold is determined with the appropriate values for: the orbital distance from the primary, the mass of the primary, the envelope gas temperature, the mean molecular weight (of the envelope gas), and the solid core density.

We investigated manifolds of all large bodies in the Solar System. Results are summarized in Table 2.2. Besides analyzing manifolds of the known planets, we have also looked into the planethood criteria for (larger) moons, asking: *If present-moon's primary would be a star* (e.g. see Clarke, 1968), *what role the orbiting body would assume?*

Bodies, having cores of roughly factor two within the mass of the critical core, are borderline cases, and their affiliation should be investigated with a more sophisticated physical model.

It should be noted that if a supercritical object does not have an envelope, and it

object	M_{primary}	orb. dist. a /[AU]	ρ_{core} /[kg m^{-3}]	T_{cs} /[K]	M_{crit} /[kg] [‡]	$M_{\text{obj}}/M_{\text{crit}}$	TPC satisfied
Mercury	M_{\odot}	0.387	5427	440	$2.51 \cdot 10^{22}$	13.2	✓
Venus	M_{\odot}	0.723	5204	737	$7.08 \cdot 10^{22}$	68.8	✓
Earth	M_{\odot}	1.0	5515	287	$1.91 \cdot 10^{22}$	312.8	✓
Mars	M_{\odot}	1.523	3934	210	$1.58 \cdot 10^{22}$	40.6	✓
Jupiter [†]	M_{\odot}	5.203	5515	153	$1.12 \cdot 10^{22}$	-	-
Saturn [†]	M_{\odot}	9.537	5515	143	$1.17 \cdot 10^{22}$	-	-
Uranus [†]	M_{\odot}	19.19	5515	68	$4.47 \cdot 10^{21}$	-	-
Neptune [†]	M_{\odot}	30.07	5515	53	$3.16 \cdot 10^{21}$	-	-
Pluto	M_{\odot}	39.48	1750	44	$4.46 \cdot 10^{21}$	2.8	✓?
Ceres	M_{\odot}	2.767	2050	167	$1.66 \cdot 10^{22}$	0.057	×
Moon	M_{\oplus}	0.00254	3344	250	$1.0 \cdot 10^{22}$	7.35	✓
Io	M_{J}	0.0028	3550	130	$1.0 \cdot 10^{21}$	89.4	✓
Europa	M_{J}	0.004486	3010	103	$1.12 \cdot 10^{21}$	42.78	✓
Ganymede	M_{J}	0.00715	1936	115	$2.51 \cdot 10^{21}$	59.0	✓
Callisto	M_{J}	0.01259	1851	115	$3.16 \cdot 10^{21}$	34.03	✓
Mimas	M_{S}	0.00124	1170	70	$2.51 \cdot 10^{20}$	0.15	×
Enceladus	M_{S}	0.00159	1300	70	$3.16 \cdot 10^{20}$	0.27	×
Tethys	M_{S}	0.00197	990	86	$6.31 \cdot 10^{20}$	0.98	✓?
Dione	M_{S}	0.00252	1500	87	$8.91 \cdot 10^{20}$	1.23	✓?
Rhea	M_{S}	0.00352	1240	76	$1.0 \cdot 10^{21}$	2.32	✓?
Titan	M_{S}	0.00817	1880	94	$2.24 \cdot 10^{21}$	60.1	✓
Iapetus	M_{S}	0.02381	1974	76	$2.69 \cdot 10^{21}$	0.73	×

Table 2.1: Terrestrial Planethood Criterion (TPC) for Solar System objects. Celestial bodies are assumed to fulfill TPC if they can keep a nitrogen atmosphere of temperature T_{cs} , in a vacuum, orbiting at a distance a from a parent star of mass M_{primary} . Solar system giant planets are supercritical even for a solar composition gas (hence also for nitrogen), thus we only show the value for the nitrogen-supercritical object, at the present-day locations of the giant planets. See text for discussion.

[†] At the locations of gas giants we show a critical core mass for Earth's density

[‡] Data sets calculated with C. Broeg, AIU Jena

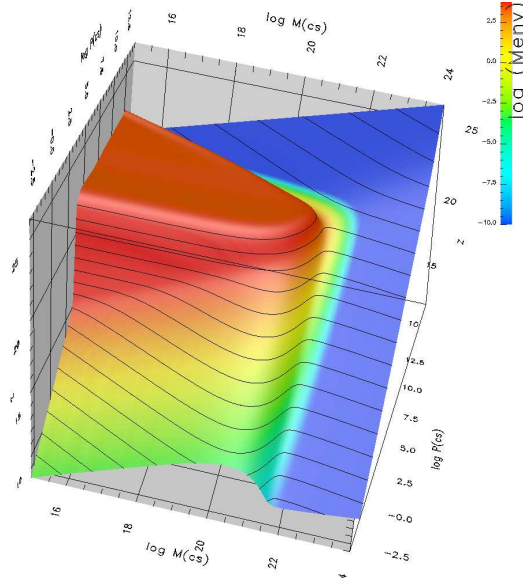


Figure 2.1: Mass manifold for the core density of $\rho_{\text{core}} = 1880 \text{ kg m}^{-3}$, Titan’s orbital parameters a , T , $M_{\star} = M_{\text{J}}$, and $\mu(\text{N}_2)$. Color scale is the outer density. Deep blue color represents compact envelopes. Core with the mass of Titan is supercritical for nitrogen, and is fulfilling a terrestrial planethood criterion. *Titan can have an N_2 atmosphere, because it is supercritical.* See text for further discussion.

could have one according to our classification, there is no contradiction.

This simply means that the significant amounts of nitrogen gas (or any other gas with a relatively high mean molecular weight) was not available during the formation/evolution of the body, or has been lost. The body itself could still qualify as a planet, on the condition that its core is supercritical. For bodies without an atmosphere, we choose the appropriate manifold temperature from the respective present-day surface temperatures. The surface temperature of Titan, similar to the average surface temperatures of other major Saturn’s moons, justifies such a choice.

We present in more detail the manifold for the parameters appropriate for the position and the environment of Titan. The envelope mass manifold is plotted in Fig. 2.1 and a manifold for the envelope density at the outer boundary is shown in Fig. 2.2. Comparing those pictures, we see that a 10^{23} kg core has a compact envelope regardless of the gas density at the core surface. Such a core always has a hydrostatic envelope solution

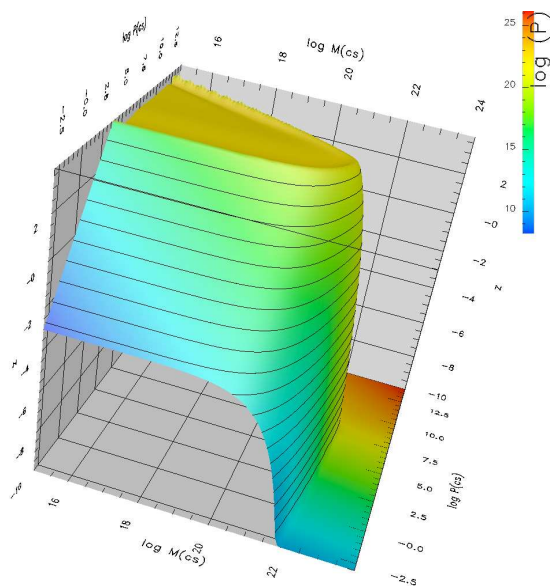


Figure 2.2: Outer density manifold for the core density of $\rho_{\text{core}} = 1880 \text{ kg m}^{-3}$, Titan's orbital parameters a , T , $M_{\star} = M_{\text{J}}$, and $\mu(\text{N}_2)$. Values below 10^{-10} Pa are plotted as 10^{-10} Pa . Color scale is the envelope mass.

which connects to the vacuous nebula, and will therefore in principle⁵ be able to retain its atmosphere indefinitely. Since Titan's core mass is larger than 10^{23} kg , it follows that it should be able to keep the nitrogen atmosphere, provided it has one. And this is the case for the real Titan, as we presently see it.

⁵based on the nature of the hydrostatic equilibrium, i.e. the balance between pressure and gravity

Chapter 3

Hydrodynamic Classification

In Chapter 1 we performed the classification of all possible hydrostatic solutions for a core-envelope model. This Chapter will try to discriminate stable, i.e. physically significant, solutions, from unstable ones. Due to intrinsic non-linear nature of the problem, we felt that a linear stability analysis would not provide a complete picture. Therefore we decided to use the static profiles, from Chapter 1, as initial states for a hydrodynamical code. After considering the dynamical timescales of the problem, as well as the number of the calculations needed for different models, we decided to use an explicit hydrodynamic code, which was possible to build and test within a reasonable time-frame, and whose performance was good enough for the required problem. We investigated the transition region between linearly stable and linearly (and non-linearly) unstable envelopes, as well as the envelope stability around the critical core mass. We also looked into the typical perturbations needed to make a transition from one multiple solution to the other.

3.1 Computational strategy

Two basic options are available for the hydro-dynamical analysis; system of equations, determining a new time level, could either be explicit or implicit functions of the values/equations from the previous time level. Implicit schemes in general have numerous physical and numerical advantages over the explicit counterparts, but are technically more challenging. Faced not only with a problem of technical development, but also with the challenge of crossing into a relatively uncharted physical problem, we decided to use an explicit hydrodynamic scheme. Such code was possible to build and test within a given time-frame, and its performance (correct to 10^{-3} level) was good enough for the required problem (c.f. Sect. 3.3).

The nature of our survey requires investigation of more than a hundred different protoplanetary models, and typically follows the evolution of every model for about ten to hundred sound-crossing times. These requirements would not be possible to fulfill for the models with a realistic core density of solids (i.e. $\rho_{\text{core}} \approx 10^3 \text{ kg m}^{-3}$), because such a core density imposes a prohibitively small time-step size in our explicit scheme, through the Courant-Friedrichs-Levy condition (c.f. Sect 3.2).

The compromise solution, increasing the cell size, is achieved through reducing the core density, but only to the point where we can still be reasonably certain that our dynamical analysis is qualitatively correct. Through a comparison of the linear stability properties for manifolds with different core densities (c.f. Schönke, 2005), we have chosen, for our models, the core density of $\rho_{\text{core}} = 1 \text{ kg m}^{-3}$.

Finally, we chose the *Ada95* developing environment, as an experiment testing the advantages of an object-oriented approach to astrophysical numerical modelling, compared to traditional programming languages (e.g. fortran, pascal).

3.2 Hydro-code setup

The equation system

The dynamical behavior of radiation and matter is contained in the equations of radiation hydrodynamics (RHD). In the concordance with our model, we assume small, non-relativistic velocities, spherical (1D) geometry, and an Eulerian (fixed) coordinate system (c.f. e.g. Winkler and Norman (1987)). Then the equations describing the gas are:

Equation of continuity (mass conservation):

$$\frac{\partial \varrho}{\partial t} + \frac{1}{r^2} \frac{\partial r^2 \varrho u}{\partial r} = 0 \quad (3.2.1)$$

Equation of motion (momentum conservation):

$$\frac{\partial \varrho u}{\partial t} + \frac{1}{r^2} \frac{\partial r^2 \varrho u u}{\partial r} + \frac{\partial P}{\partial r} + \frac{G \varrho m}{r^2} - \frac{4\pi}{c} \varrho \kappa_H H - u_Q = 0 \quad (3.2.2)$$

Equation of gas energy (1st law of thermodynamics):

$$\frac{\partial \varrho e}{\partial t} + \frac{1}{r^2} \frac{\partial r^2 \varrho u e}{\partial r} + P \frac{1}{r^2} \frac{\partial r^2 u}{\partial r} + 4\pi \varrho (\kappa_J J - \kappa_S S) - \varrho (\epsilon_{nuc} + \epsilon_Q) = 0 \quad (3.2.3)$$

The effect of the self-gravity is included by the

Poisson equation (self-gravity):

$$m = \int_0^r 4\pi \varrho r'^2 dr', \quad (3.2.4)$$

and the radiation field is described with

Radiation energy equation (0th moment):

$$\frac{1}{c} \frac{\partial J}{\partial t} + \frac{1}{r^2} \frac{\partial r^2 J u}{\partial r} + \frac{1}{r^2} \frac{\partial r^2 H}{\partial r} + \frac{1}{c} K \frac{1}{r^2} \frac{\partial r^2 u}{\partial r} - \frac{1}{c} \frac{3K - J}{r} u + \varrho (\kappa_J J - \kappa_S S) = 0, \quad (3.2.5)$$

Radiation flux equation (1st moment):

$$\frac{1}{c} \frac{\partial H}{\partial t} + \frac{1}{c} \frac{1}{r^2} \frac{\partial r^2 H u}{\partial r} + \frac{\partial K}{\partial r} + \frac{3K - J}{r} + \frac{1}{c} H \frac{1}{r^2} \frac{\partial r^2 u}{\partial r} + \varrho \kappa_H H = 0. \quad (3.2.6)$$

Table 3.1: Symbols in the RHD equations

Symbol	Meaning
ϱ	gas density
u	gas velocity
r	radial coordiante
t	temporal coordinate
P	pressure
m	mass
c	speed of light
$\{J, H, K\}_\nu$ †	0 th , 1 st , and 2 nd moment of the specific intensity
$S_\nu = \frac{4\pi}{c} J_\nu$ †	monochromatic radiation energy density
$\kappa_H, \kappa_J, \kappa_S,$	interaction with the radiation field
ϵ_{nuc}	nuclear energy production rate
ϵ_Q	artificial viscous energy production rate
u_Q	artificial viscous pressure
V	volume
A	surface

† for discussion c.f. e.g. LeVeque et al. (1997), § by D. Mihalas

All of the variables used in these equations can be found in Table 3.1.

The isothermal case simplifies the situation; isothermality implies that the ‘surplus energy’ is instantly radiated away (with the infinite speed and the perfect efficiency). This reduces the system of equations which we use to 3.2.7; the *continuity equation* (3.2.1) and the *equation of motion* without the contribution from the radiative flux, $F = 4\pi H$:

$$\frac{\partial \varrho}{\partial t} + \frac{1}{r^2} \frac{\partial r^2 \varrho u}{\partial r} = 0$$

$$\frac{\partial \varrho u}{\partial t} + \frac{1}{r^2} \frac{\partial r^2 \varrho u u}{\partial r} + \frac{\partial P}{\partial r} + \frac{G \varrho m}{r^2} - u_Q = 0, \quad (3.2.7)$$

where m is calculated through *the Poisson equation* (3.2.4).

To proceed to a discretized set of equations, suitable for the numerical modeling, we will rewrite our equation set in the integral form:, for a volume V with surface ∂V

$$\frac{\partial}{\partial t} \int_V \varrho dV + \int_{\partial V} \varrho u dA = 0 \quad (3.2.8)$$

and

$$\frac{\partial}{\partial t} \int_V \varrho u dV + \int_{\partial V} \varrho u u dA + \int_V \nabla P dV + \int_V \frac{Gm\varrho}{r^2} dV = 0. \quad (3.2.9)$$

Notation and definitions of the discretized system

The discrete version of the equation set is obtained by applying the rules which transform the differential operators into finite volume operators. The temporal difference (3.2.10) and the spatial difference (3.2.11) are defined for any physical quantity X located at the grid point r_l , i.e., $X_i = X(r_i)$. Label X denotes a physical quantity from a new time level, while X^* is referring to the same quantity, but from a previous time level.

$$\delta X_i = X_i - X_i^* \quad (3.2.10)$$

$$\Delta X_i = X_i - X_{i+1} \quad (3.2.11)$$

$$\bar{X}_i = 0.5(X_i + X_{i+1}) \quad (3.2.12)$$

$$\Delta \text{Vol}_i = \frac{1}{3}(r_i^3 + r_{i+1}^3) \quad (3.2.13)$$

The smallest grid index ($i = 1$) is reserved for the outer grid boundary, while the largest ($i = l_{\max}$) corresponds to the inner grid boundary. On the other hand, the zero-point for the radial coordinate is placed into the center of the sphere.

Viscosity and diffusion

The artificial viscosity is used in order to broaden shock waves over a few computational cells. The artificial viscosity coefficient μ_Q is given with (c.f. LeVeque et al. (1997), § by E. Dorfi):

$$\mu_{Q_i} = q_1 l_{\text{visc}} c_T - (q_2 l_{\text{visc}})^2 \min(\nabla u_i, 0) \quad (3.2.14)$$

The expression for μ_Q includes a typical viscous length scale l_{visc} . The linear term in l_{visc} is usually included to damp out small scale oscillations near contact discontinuities, and is always present for non-zero q_1 . However, test calculations have showed that these

type of oscillations are either insignificant or non-existent in our model. The second term is quadratic in l_{visc} and is set in a way that *compressive and non-homologous* motions produce a viscous pressure. To be able to resolve the shock on a grid scale, $q_{1,2} l_{\text{visc}} \simeq \Delta x$ must be fulfilled.

We have chosen $q_2 = 7$, to be able to calculate possible strong shocks ($>$ Mach 10). With $q_1 = 0$, and with the appropriate expression for divergence in spherical geometry, we calculate the artificial viscosity coefficient from:

$$\mu_{Q_i} = -q_2 \Delta r_i \min \left(\frac{\Delta (r_i^2 u_i)}{\Delta \text{Vol}_i}, 0 \right) \quad (3.2.15)$$

Introducing artificial viscosity is equivalent to the existence of a diffusive process, which will introduce an additional restriction on the size of the time step.

Time-stepping

For stability reasons, all explicit schemes must obey *Courant-Friedrichs-Levy* (CFL) condition, Courant et al. (1928), here presented in its simplest form for a grid spacing Δx :

$$t_{\text{CFL}} = \min_{\text{all cells}} \frac{\Delta x}{|u| + c_T}, \quad (3.2.16)$$

where u is the gas velocity, and c_T is the isothermal sound velocity.

Additional constraint arises from the diffusive process introduced through the artificial viscosity coefficient (c.f. LeVeque et al. (1997), § by E. Dorfi):

$$t_D = \min_{\text{all cells}} \frac{1}{6} \frac{(\Delta x)^2}{\mu_Q}. \quad (3.2.17)$$

The time step size is then determined from:

$$\delta t = \alpha \min(t_{\text{CFL}}, t_D), \quad (3.2.18)$$

where $\alpha < 1$ is additional parameter for ensuring the stability of the scheme. We use $\alpha = 0.4$.

Advection

We tested two advection schemes (cf. Sect. 3.3.1), and decided to use Van Leer's monotonic advection (VL), cf. e.g. Winkler and Norman (1987), p.109-110. VL scheme uses 4-point stencil, i.e. it requires information about physical quantity in question from the neighboring cells. Hence, it was impossible to implement VL scheme for the cells on the boundaries. For the inner and the outer boundary, the donor cell (DC) advection scheme was used instead.

DC scheme can be described with:

$$X_i^{\text{adv}} = \begin{cases} X_i^* & \text{if } u_i \geq 0 \\ X_{i-1}^* & \text{if } u_i < 0 \end{cases} \quad (3.2.19)$$

VL advection, on the other hand, follows this recipe (Winkler and Norman (1987), p.109-110):

$$s_i = \begin{cases} 0.5 & \text{if } u_i \geq 0 \\ -0.5 & \text{if } u_i < 0 \end{cases}$$

$$d_{\text{WN}}X_i = \begin{cases} \frac{2\Delta X_{i-1}\Delta X_i}{X_{i-1} - X_{i+1}} & \text{if } \Delta X_{i-1}\Delta X_i > 0 \\ 0 & \text{otherwise} \end{cases}$$

$$X_i^{\text{adv}} = (0.5 + s_i)(X_i^* + 0.5 d_{\text{WN}}X_i^*) + (0.5 - s_i)(X_{i-1}^* + 0.5 d_{\text{WN}}X_{i-1}^*) \quad (3.2.20)$$

The use of $d_{\text{WN}}X$ here is to be consistent with Winkler and Norman (1987), and is not to be confused with the differential notation.

The advected quantity for the new time-level is a function of the variables from the previous time-level only, and can be calculated before the cell gas density and velocity for the new time-level are known. In fact, such an advected quantity is used to calculate ρ_i and u_i for the new time-level.

Discretized set of equations

Applying the transformations, of the differential operators to the finite volume operators, onto the equations 3.2.8 and 3.2.9, and solving for the envelope gas density, and the gas

velocity (both belonging to the new time level), one gets the following relations:

Gas density of the i -th cell:

$$\varrho_i = \varrho_i^* - \frac{\delta t}{\Delta \text{Vol}_i} \Delta(r_i^2 u_i^* \varrho_i^{\text{adv}}) \quad (3.2.21)$$

Gas velocity of the i -th cell:

$$\begin{aligned} u_i = & u_i^* \frac{\overline{m_{i-1}^*}}{m_{i-1}} - \frac{\delta t}{m_{i-1}} \cdot (\\ & \Delta \left[\left\{ \overline{r_{i-1}^2 \varrho_{i-1}^{\text{adv}} u_{i-1}^*} \right\} u_i^{\text{adv},*} \right] \\ & + r_i^2 \Delta(P_{i-1}) \\ & + 4\pi \frac{GM(r_i)}{r_{i,1/2}^2} \\ & + \left[-\frac{2}{3} \Delta \left\{ \mu_{Q_i} \varrho_{i-1}^* r_{i-1}^3 \left(\frac{\Delta u_{i-1}^*}{\Delta r_{i-1}} - \frac{\overline{u_{i-1}^*}}{\overline{r_{i-1}}} \right) \right\} \right]) \end{aligned} \quad (3.2.22)$$

The cell mass is defined as $m_i = \varrho_i \Delta \text{Vol}_i$, and m_{i-1} is used instead of m_i in Eq. 3.2.22 for the numerical convenience; choice of whether to average over i -th cell and left or right neighbor is completely arbitrary.

For the discussion on the renormalization of the radius used to calculate gravitational term in the equation of motion, $r_{i,1/2}$, see Sect. 3.2: *Numerical perturbations - static gravitational cell mass*. $M(r_i)$ is defined as the mass interior to the grid-point r_i .

Note that the ϱ_i is a function of the variables from the previous time-level only, in accordance with the principles of the explicit scheme. Function for the u_i , on the contrary, combines the variables from the previous time-level with the variables from the current time-level, namely $\overline{m_{i-1}}$ and ΔP_{i-1} . Combining the variables from different time-levels to compute a new variable is a trademark of implicit schemes. However, during initial testing we noticed that the scheme is much more stable if we use the combination of variables as stated in Eq. 3.2.22. Other tests (cf. Sect. 3.3) ensured us that the calculated variables are consistent with the analytical expectations within the expected order of accuracy.

Boundary conditions

The different sets of boundary conditions (BCs) were used during initial test phases and main calculation run. Here we discuss only the main calculation BCs. Other BCs are elaborated in the sections devoted to respective test calculations.

Inner BCs

The inner boundary, with cell index $i = i_{\max}$, represents the immediate sub-surface of the core. The core is an incompressible sphere. Therefore, envelope gas cannot penetrate or compress the core. This translates into a following set of inner BCs:

$$r_{i_{\max}} = r_{\text{core}} = \text{const} \quad (3.2.23)$$

$$\varrho_{i_{\max}} = 0 \quad (3.2.24)$$

$$u_{i_{\max}} = 0$$

$$X_{i_{\max}}^{\text{adv}} = 0,$$

where ϱ is envelope gas density, u is gas velocity, and X^{adv} is any advected physical quantity.

Outer BCs The model represents a planet embedded in an inert nebula with infinite supply of gas. Thus, the nebula gas density is constant in time, and gas momentum transferred across the outer boundary will correspond to that of the constant nebula. Strictly speaking, it is unphysical to keep the gas density at the outer boundary (i.e. the nebula density) constant. This could lead to the wave-front reflections (of the outer boundary and back into the envelope), which would not happen in reality. But modelling the behavior of the nebula density, to properly mimic nebula response to the incoming envelope wave front, would be complex, to say the least, and there is no guarantee that the result of such modelling would be more physical than the present (constant density) assumption.

The following equations describe the stated outer BCs:

$$r_1 = r_{\text{out}}(t = 0) = \text{const} \quad (3.2.25)$$

$$\varrho_1^{\text{adv}} = \begin{cases} \varrho_1^* & \text{if } u_1^* \geq 0 \\ \varrho_{\text{neb}} & \text{if } u_1^* < 0 \end{cases}$$

$$u_1^{\text{adv}} = \begin{cases} u_1^* & \text{if } u_1^* \geq 0 \\ u_1^* & \text{if } u_1^* < 0 \end{cases}$$

Nebula density is determined from the initial hydrostatic condition, by linear extrapolation from the density gradient of the outermost cell. Such procedure is chosen, as opposed to $\varrho_{\text{neb}} = \varrho_1$, to avoid the perturbation caused by the force imbalance between the force of gravity and the zero pressure gradient (between the outermost cell and nebula cloud).

Numerical perturbations - static gravitational cell mass

The hydro-code uses a static radial profile, calculated with the 4-5 order Runge-Kutha method (rk45) in Maple 6. The discretization schemes in the rk45 and in the hydro-code are not the same; the rk45 evaluates the mass and the density at a particular point r_i , while hydro-code assumes constant density for the grid cell bounded with points r_i and r_{i+1} . Therefore, using r_i , in the calculation of the gravitational component of the equation of motion,

$$\frac{G \cdot M(r_i)}{r_i^2}, \quad (3.2.26)$$

produces underestimation of the strength of the gravitational force, because the mass element is not evaluated at its center of mass, but at its outer edge, r_i . To evaluate the mass element at the appropriate radius, following substitution is made for the $1/r_i^2$ in the equation of motion:

$$r_i \rightarrow r_{i,1/2} = \sqrt[3]{\frac{r_i^3 + r_{i+1}^3}{2}} \quad (3.2.27)$$

The mass-centered coordinate $r_{i,1/2}$ represents a center of mass for a constant-density spherically symmetric cell. As a result, the scheme-discrepancy perturbation is reduced by a factor of 3 (cf. Fig. 3.1). If the average amplitude of the scheme-perturbation is taken to be 4 cm s^{-1} , then the perturbation of the initial (static) solution in this case is equivalent to Mach $5.6 \cdot 10^{-5}$. This should be equivalent to the ideal, no-perturbation,

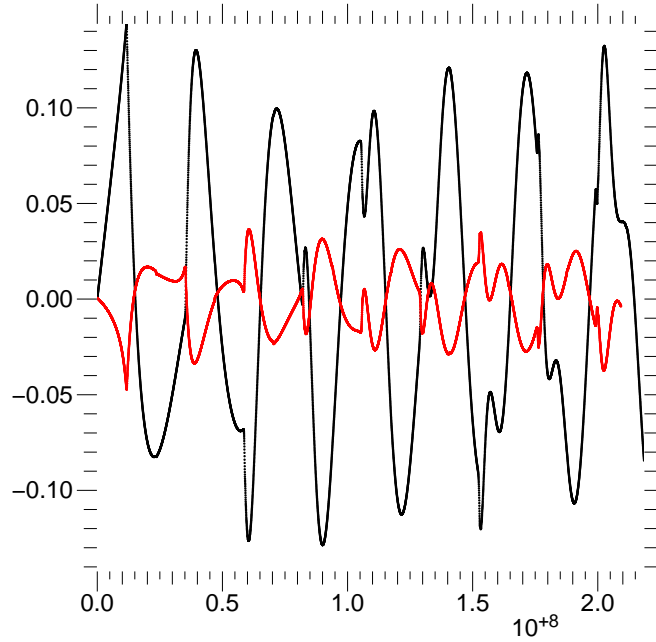


Figure 3.1: The time-evolution of the velocity at the outer boundary. Black points represent solution with r_i in the gravitational term of the equation of motion, while red points is the solution with mass-centered coordinates $r_{i,1/2}$. Time is in 10^8 seconds, and velocity in meters per second.

case for all but the most unstable envelope states.

Small perturbation is true for low gas density gradients. However, for the compact envelopes, with higher density gradients, deviation from the piecewise-constant density approximation will be larger, and the envelope perturbation will be stronger. We noticed, for a specific set of models, a direct analytic relation between the gas density at the core surface and the strength of the perturbation (c.f. bottom left plot of Fig. 3.21). The strength of the perturbation is connected to the duration of transition until envelope reaches the pulsating mode; envelope with 2^n higher value than ρ_x will take t^n time to switch from initial state to pulsating mode. Time t is the duration of the transition into the pulsating mode for the envelope with a ρ_x gas density at the core surface.

This means that, *for a model sequence with the same core, but increasing gas density at the core surface, models with higher ρ_{cs} will initially be more perturbed* (intrinsically, just with the change of the discretization scheme and the increasing discretization error difference

for increasing $\nabla \rho_{\text{cs}}$). In other words, perturbation is not the same for all models, but is instead tied to the envelope density gradients.

Increasing strength of the perturbation has to be taken into account when reviewing model sequences with the increasing gas density at the core surface (all surveys in Sect. 3.4).

3.3 Scheme tests

3.3.1 Saw-tooth profile advection

Several advection schemes are applicable to our model (c.f. e.g. LeVeque et al. (1997), § by E. Dorfi). In order to choose the most appropriate one, we tested two of those schemes - the Van Leer's monotonic advection (VL) and the donor cell advection (DC).

The donor cell scheme assumes constant value of the advected physical quantity throughout one cell, while the Van Leer's scheme presumes constant gradient of the same advected physical quantity, within each cell. Recipe for the VL scheme we used is given by Eqs. 3.2.20, while the DC scheme can be described with 3.2.19.

Numerical testing of the advection schemes was done with the same code which was later used to calculate the dynamics of the planetary envelopes, but the code setup was specially adjusted to accommodate to the specific requirements of the test.

The advection schemes were tested by advecting a saw-tooth density profile in a constant velocity field. The radial boundaries of the system were chosen such that the geometrical effects (spherical system) have minimal effect: $(r_{\text{out}} - r_{\text{in}})/r_{\text{out}} = 5 \cdot 10^{-4}$. The core mass was obviously set to zero, and the gravitating mass of the envelope gas was negligible.

The test results are summarized in Figs. 3.2 and 3.3. Both plots clearly show that the DC scheme is much more dissipative than the VL scheme - maximum deviation from the initial profile was about five times lower than for the DC, and the DC deviation regions are at least twice as large as those of VL. This kind of numerical dissipation has

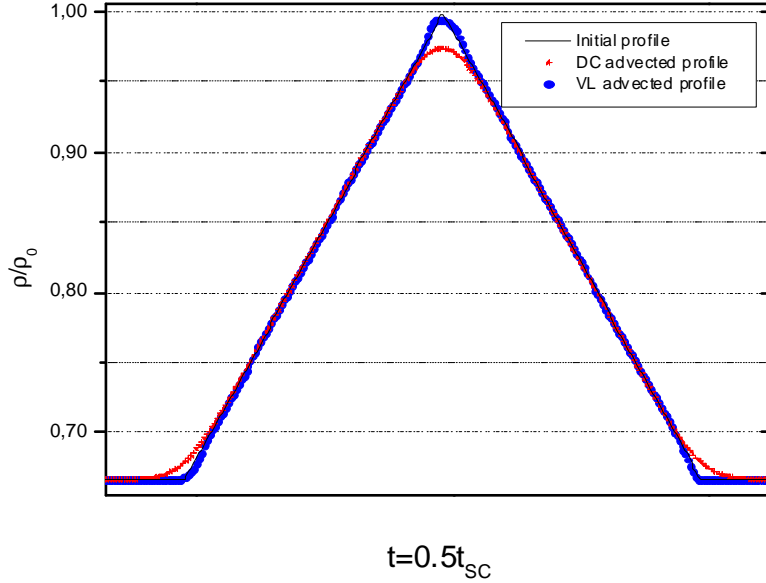


Figure 3.2: The radial profile of the advected saw-tooth profile, after half a sound crossing time. The donor cell advection scheme was used for the red profile, and the Van Leer's for the blue one. The initial profile is overplotted as a black line, to give an estimate of the profile distortion as a result of the advection scheme.

no equivalent in the physical process we are trying to model. Therefore, dissipation due to advection scheme had to be minimized, resulting in the use of the Van Leer's advection in the forthcoming calculations.

3.3.2 Free-fall

One of the tests for the evaluation of the performance of the hydro-dynamical code was computation of the free-fall of the constant-density gas cloud. The free-fall of the gaseous cloud will test the performance of the equation of motion used in our model.

When, according to the Jeans criterion, a gaseous mass has become unstable and the collapse has started, gravity increases more than the pressure gradient (c.f. e.g. Kippenhahn and Weigert (1990)). For spherical symmetry the gravitational acceleration is of the order GM/R^2 , where M is the total mass and R is the radius of the cloud, while an estimate

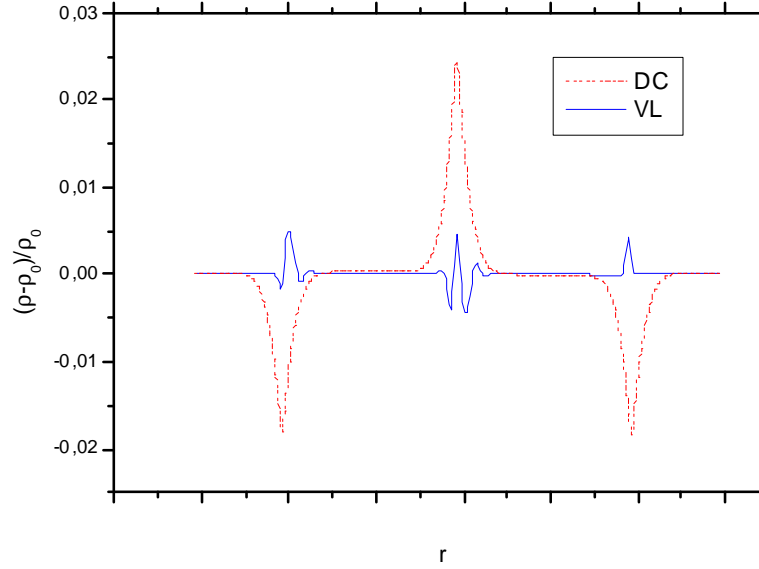


Figure 3.3: The relative deviation from the original saw-tooth profile. The donor cell-advected profile is red dashed line, and the Van Leer’s-advected profile is blue solid line. Maximum deviation is, as expected, around first derivative discontinuities of the original profile (the wing-bases and the top of the ‘tooth’). The donor cell scheme is considerably more dissipative than Van Leer’s.

for the acceleration due to the pressure gradient is

$$\left| \frac{1}{\rho} \frac{\partial P}{\partial r} \right| \approx \frac{P}{\rho R} \approx \frac{\Re T}{\mu R}. \quad (3.3.1)$$

The ratio of gravitational force to pressure gradient is therefore $\sim M/(RT)$, which during isothermal collapse increases as $1/R$. Consequently we may neglect the gas pressure, both in the derivation of the expression for the free-fall time, and in the equation of motion which is part of the numerical model equation set. The test problem is also a good approximation for the early gas cloud collapse.

The free collapse of a homogenous sphere can be treated analytically (e.g. Kippenhahn and Weigert, 1990, §27.1). Integrating the equation of motion

$$\frac{\partial^2 r}{\partial t^2} = -\frac{4\pi \rho_0 r_0^3 G}{3 r^2} \quad (3.3.2)$$

where subscript zero denotes the values at the beginning of the collapse, and after we introduce a new variable ζ , defined by

$$\cos^2 \zeta = \frac{r}{r_0} \quad (3.3.3)$$

we can write

$$\zeta + \frac{1}{2} \sin 2\zeta = \left(\frac{8\pi G \varrho_0}{2}\right)^{1/2} t \quad (3.3.4)$$

where the integration constant is chosen such that the beginning of the collapse (when $r = r_0$, or $\zeta = 0$) coincides with $t = 0$. It should be noted that r_0 no longer explicitly appears in the solution (3.3.4) and that $\varrho_0 = \text{const}$. Therefore, solution $\zeta(t)$ and consequently r/r_0 and \dot{r}/r_0 at a given time t are the same for all mass shells. This means that the sphere undergoes homologous compression. Since \dot{r}/r_0 is independent of r_0 , the relative density variation is independent of r_0 , and the sphere, which was homologous at $t = 0$, remains homologous.

Since our protoplanetary model always has a core, we are not interested in the free-fall time to the center of the sphere, but just in the time it takes the outermost mass shell to reach some r_{in} . Therefore, we choose $r_{\text{in}} = r_{\text{core}}$, and solve Eqn. 3.3.4 for

$$\cos^2 \zeta = \frac{r_{\text{in}}}{r_0}. \quad (3.3.5)$$

Setup

The cloud consists of the 1000 log-equidistant, spherically symmetric shells, extending from r_{in} to r_{out} . All of the shells initially have the same density, and they have zero initial velocity. The cloud is composed of the isothermal, pressureless, and ideal gas.

The gas is able to freely pass bellow $r_{\text{in}} = r_{\text{core}}$, and the *goal of the test* is to calculate the time it takes for the mass shell, that was initially at $r_{\text{init}} = r_0$, to reach the inner boundary, r_{in} .

To estimate the constancy of the cloud density during the collapse, streamlines are followed from the shells' initial positions. A particular streamline is not followed after it has

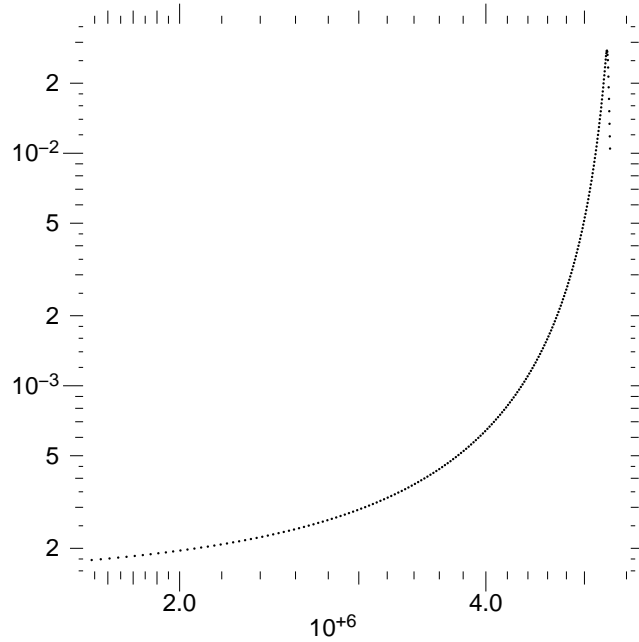


Figure 3.4: Time series/[10^8 s] of the gas density/[kg m^{-3}] at r_{in} . Peak denotes the moment when the outermost mass shell passes r_{in} .

collapsed below r_{in} , arbitrarily set at $r_{in} = 1.96 \cdot 10^9$ m. However, mass of the gas that has passed r_{in} is added to the mass of the sphere bounded within r_{in} . Therefore gravitational potential, due to the mass within r_{in} , is accounted for.

The cell grid consists of 1000 log-equidistant eulerian cells, making the typical relative grid resolution is $(\Delta r)/r \approx 10^{-3}$, which is also a rough estimate for the typical relative error.

Table 3.2 summarizes parameters used for the free-fall collapse.

Results

Within the isothermal paradigm, all the mass shells should collapse to the center at the same time. However, to avoid numerical problems at $r = 0$, and to keep isothermal assumption reasonably valid, collapse was followed only till r_{in} has been reached. Therefore, mass shells will reach inner boundary, r_{in} , at different times and with different gas densities. But at any particular time, all the (initial) mass shells outside r_{in} should have the same density (cf. introduction for this test calculation). This was indeed the case up to

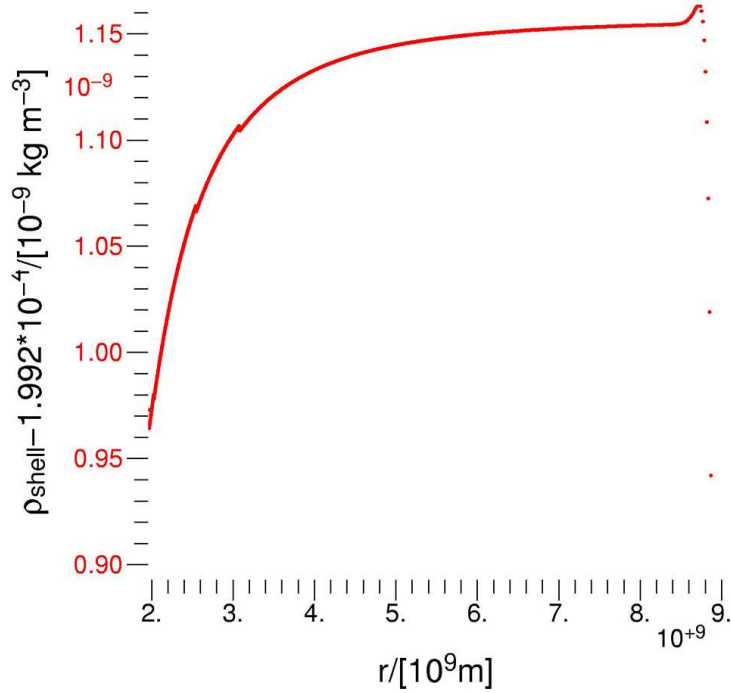


Figure 3.5: Density profile of the collapse of the initially-constant-density gas cloud. This particular snapshot is taken at about $0.5 t_{\text{ff}}$ of the outermost mass shell. Density scale, $10^{-9} \text{ kg m}^{-3}$, is centered on a $1.992 \cdot 10^{-4} \text{ kg m}^{-3}$. Relative density variation across the collapsing cloud is on the 10^{-4} level.

a 10^{-4} level, as can be seen from a typical collapse profile shown on a Fig. 3.5.

Figure 3.6 shows the relative deviation of the numerical values, from the analytical model, of the free-fall time for different mass shells. The relative difference is on a 10^{-3} level, and the deviation is largest for the innermost and the outermost cells. The deviation is largest at the boundaries because of the imperfect boundary conditions, mimicking open boundaries, i.e. the gas free-flow. But these boundary conditions were specific for this test, and were in no part the main subject of the testing procedure.

In general, Fig. 3.6 tells us that our pressureless form of *the equation of motion follows the analytic model to an expected degree of accuracy*. The cell grid consists of 1000 log-equidistant eulerian cells. Therefore, typical relative grid resolution is $(\Delta r)/r \approx 10^{-3}$. According to LeVeque et al. (1997, § 4.1.1), the method has global order p if the global error is $O((\Delta r)/r)^p$. Since we use a first order method (cf. Section 3.2), we expect that

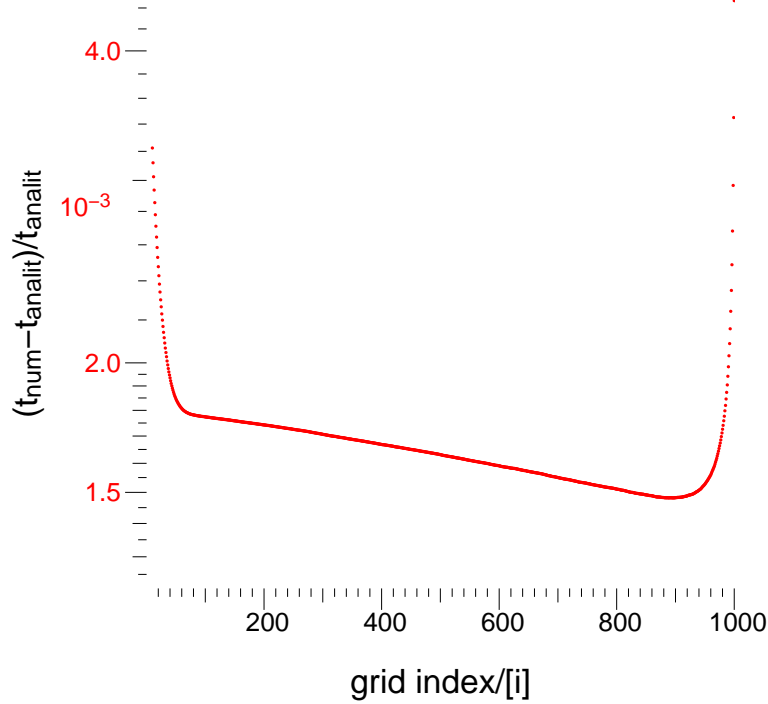


Figure 3.6: Relative error (on a 10^{-3} scale) of the numerical value of the free-fall time (vs the analytic expression, Eq. 3.3.4), as a function of the shell index, i .

Table 3.2: Free Fall Collapse Setup

initial cloud density ϱ_{cloud}	$1.5 \cdot 10^{-4} \text{ kg m}^{-3}$
inner boundary	$1.96 \cdot 10^9 \text{ m}$
outer boundary	$1.27 \cdot 10^{10} \text{ m}$
number of grid cells	1000
gas temperature	123 K

the relative error will be on the 10^{-3} level (for a 1000-cell grid).

3.3.3 Isothermal shock tube

One of the tests for the evaluation of the performance of the hydro-dynamical code was the classical shock tube problem. We follow the discussion of Courant and Friedrichs (1948), and specialize it for the isothermal case. In the next subsection we present the analytic solution for the isothermal gas case, and we use that solution in the following subsections for comparison with the numerical values for the flow variables.

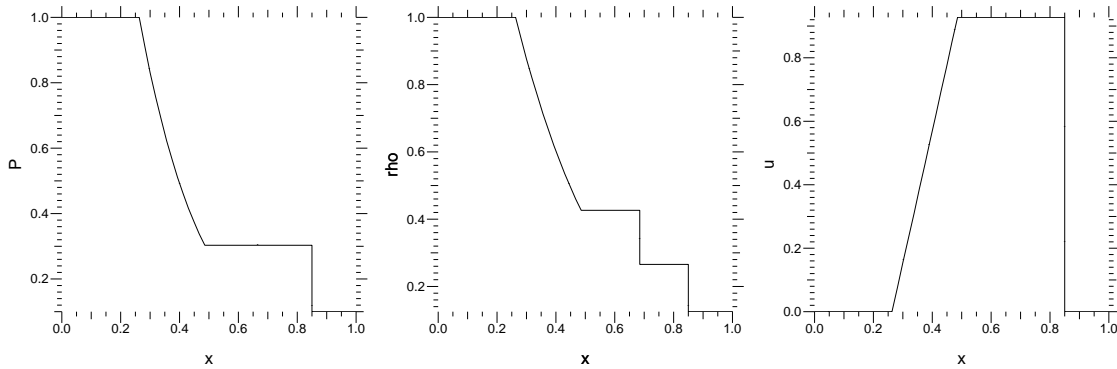


Figure 3.7: Sketch of the adiabatic-gas shock tube test problem. From the left to right: pressure, density, and velocity profile for classical Sod shock tube problem at $t = 0.2$: $P_{\text{left}} = 1$, $\rho_{\text{left}} = 1$, $u_{\text{left}} = 0$, $P_{\text{right}} = 0.1$, $\rho_{\text{right}} = 0.125$, $u_{\text{right}} = 0$. Time is in dimensionless units of sound-crossing time.

Analytic solution for the isothermal ideal gas shock tube

General remarks

The most notable difference in a shock tube problem for an isothermal and an adiabatic gas is the non-existence of the contact discontinuity for the isothermal case (compare Figures 3.7 and 3.8). The pressure on the both sides of the contact discontinuity has to be the same. In the adiabatic case, the gas on the right side is heated when passing across the shock, while the gas on the left side does not change its temperature. Therefore to keep the pressure balance, the density on the left side has to be higher (than the density on the right side). For the isothermal gas there is no heating across the shock, and the densities on both sides of the contact discontinuity are the same.

Figure 3.8 shows a typical test situation; initially, tube is split in the middle with a membrane at x_0 . The density of the region left of the membrane (ρ_L) is higher than the density (ρ_R) of the region to the right.

After the membrane is (instantaneously) removed at t_0 , two simple waves are created: a *shock wave*, travelling with a supersonic shock velocity U into the region of lower density, and a *rarefaction wave*, expanding into the region of the higher density with the isothermal

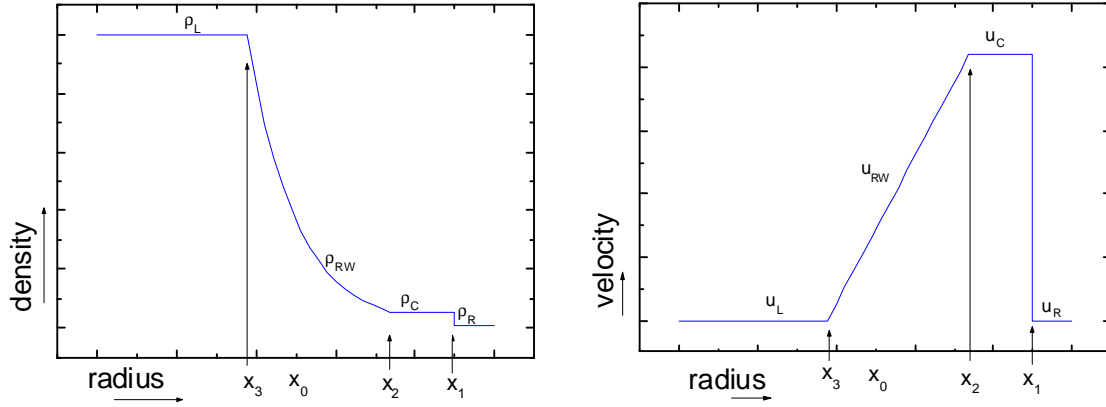


Figure 3.8: Sketch of an isothermal-gas shock tube. Left figure is a typical density profile of the isothermal shock tube. Dashed line represents initial density, with the membrane positioned at x_0 , while solid line shows density structure at some time after the release of the central membrane but before the shock hits the tube wall for the first time. Right figure is a corresponding velocity profile. Unlike the adiabatic case, a pressure profile completely corresponds to the density profile (cf. Fig. 3.7) and see text. Slight bumps inside the rarefaction wave (between points x_2 and x_3) are simplifications of the sketch and have no physical meaning.

sound speed c_T .

The gas is at rest before t_0 , therefore absolute gas velocities of the unperturbed regions, u_L and u_R , are zero by definition. The choice for the moment of the release of the membrane, t_0 , is free and we set it to $t_0 = 0$.

As the shock is propagating, it compresses the gas ϱ_R to ϱ_C , and accelerates the gas from u_R to u_C . The shock velocity U is always supersonic, while the gas behind the shock moves with the relative velocity $v_C = u_C - U$, which is always *subsonic relative to the shock*. The position of the shock in the tube, x_1 , is given with

$$x_1 = x_0 + U t. \quad (3.3.6)$$

The region behind the shockwave is a constant-flow region, because it is a product of the conditions which are valid across the shock and the constant-flow region in front of the shock. It is connected to the unperturbed, higher density region through the rarefaction

wave, which extends from x_2 to x_3 . Those rarefaction wave boundaries are determined with

$$x_2 = x_0 + (u_C - c_T)t, \quad (3.3.7)$$

$$x_3 = x_0 + (-c_T)t. \quad (3.3.8)$$

Equation 3.3.8 is obvious, since the head of the rarefaction wave is moving from the position of the membrane, x_0 , towards higher density region, with the isothermal sound speed. Equation 3.3.7 can be similarly explained, with point x_2 being ‘dragged’ from the membrane position with the velocity of sound towards the higher density region, and with the velocity u_C towards the constant-density region behind the shockwave. The point x_2 will choose its direction of motion depending on the Mach number of the region downstream from the shock, u_C/c_T , which is determined through the initial density ratio ϱ_L/ϱ_R .

The isothermal solution

The aim of this procedure is to obtain a set of equations which will allow us to describe the evolution of the sod tube problem from knowing just the initial values of gas densities at both sides of the membrane.

First two equations are coming from the conditions which are valid across the shock, namely from conservation of mass, we have

$$\varrho_C v_C = \varrho_R v_R \quad (3.3.9)$$

and the conservation of momentum yields

$$\frac{\varrho_C}{\varrho_R} = \left(\frac{U}{c_T}\right)^2. \quad (3.3.10)$$

The third equation will be obtained from the relations for the rarefaction wave density structure.

The simple wave is characterized with quantities that are conserved in time, so-called Riemann invariants. For a backward-facing wave, it can be shown (Courant and Friedrichs, 1948, §37) that the characteristic equation looks like

$$u + l(\varrho) = -2s(\alpha). \quad (3.3.11)$$

Characteristic equation holds for a simple wave:

$$u + l(\varrho) = u_0 + l_0(\varrho). \quad (3.3.12)$$

The quantity $l(\varrho)$ is given by

$$l(\varrho) = \int_{\varrho'}^{\varrho} \frac{c d\varrho}{\varrho}, \quad (3.3.13)$$

which for isothermal sound speed gives

$$l(\varrho) = c_T \ln(\varrho). \quad (3.3.14)$$

From this, and for $u_0 = 0$, it follows that the density structure of the simple backward-facing wave is given with:

$$\varrho = \varrho_L \exp\left(-\frac{u}{c_T}\right). \quad (3.3.15)$$

On the other hand, a velocity in the rarefaction wave is given with:

$$u_{\text{RW}} = \left(-\frac{x_0 - x}{t} + c_s\right) \quad (3.3.16)$$

and combining eqns. 3.3.15 and 3.3.16 we get expression for the density structure in the rarefaction wave:

$$\varrho_{\text{RW}}(x) = \varrho_L \exp\left(\frac{x_0 - x}{c t} - 1\right) \quad (3.3.17)$$

Finally, equation 3.3.17 must also be valid for the right boundary of the rarefaction wave, and we get the last equation needed to resolve the problem,

$$\varrho_{\text{RW}}(x_2) = \varrho_L \exp\left(-\frac{u_C}{c_T}\right). \quad (3.3.18)$$

Now we can determine all the flow variables for the isothermal shock tube by numerically solving for the system of equations 3.3.9, 3.3.10, and 3.3.18. The analytic solution of the system is not possible because of the combination of the exponential and polynomial equations.

Tube setup

In order to be as consistent as possible with the typical computational problem, the setup was marginally different to the one of (Sod, 1978), to directly test the spherical code.

The tube consists of the spherically symmetric shells, as opposed to Sod's equal-volume cells. However, distance from the center of the sphere and the tube range are chosen such that the volume difference between the first and the last cell is about 3%. Small cell-volume difference should insure that the geometric factors have minimal influence on the gas dynamics.

The ideal isothermal gas is used throughout the computation. We derived the piecewise-analytic solution for the isothermal ideal gas shock tube problem (cf. Sect. 3.3.3) to examine the numeric results. The resulting equation system is solved numerically with a Maple V routine.

The cell grid consists of 1000 log-equidistant eulerian cells. Therefore, typical relative grid resolution is $(\Delta r)/r \approx 10^{-3}$. According to LeVeque et al. (1997, § 4.1.1), the method has global order p if the global error is $O((\Delta r)/r)^p$. Since we use a first order method (cf. Section 3.2), we expect that the relative error will be on the 10^{-3} level (for a 1000-cell grid).

Apart from the 1000-grid-point test, equivalent to the grid used for the non-linear analysis of the protoplanetary gas envelope, we have performed the test with the 100- and 10000-grid cells. We expect that the numerical solution will converge toward the analytic one with the increase of the number of grid points.

The initial transition from ϱ_L to ϱ_R is not discontinuous in the test calculation, because

Table 3.3: Shock tube setup

ϱ_L	$10^{-10} \text{ kg m}^{-3}$
ϱ_R	$5 \cdot 10^{-11} \text{ kg m}^{-3}$
P_{left}	$0.5113 \cdot 10^{-4} \text{ Pa}$
P_{right}	$0.2557 \cdot 10^{-5} \text{ Pa}$
tube length	10^6 m
tube distance from the sphere center	10^8 m
number of grid cells	100, 1000, 10000
gas temperature	123 K

of the numerical difficulties of the problem, and is described with:

$$\varrho_{\text{sod}}(r) = \frac{\varrho_L + \varrho_R}{2} + \frac{\varrho_L - \varrho_R}{2} \tanh\left(8 \cdot 10^5 \left(\frac{r}{\Delta} - 1\right)\right) \quad (3.3.19)$$

where Δ is the radial distance of the tube center, given with

$$\Delta = r_{\text{left-wall}} + \frac{r_{\text{right-wall}} - r_{\text{left-wall}}}{2} \quad (3.3.20)$$

Table 3.3 summarizes parameters used for the shock tube test.

Results

We have tested the hydro code with two shock tubes. One has the initial pressure ratio between levels $P_L : P_R = \varrho_L : \varrho_R$ equal to 2:1, while the other has $P_L : P_R = 200 : 1$, which tests the code for the *strong shock*, as defined in Courant and Friedrichs (1948, §71). The pressure ratio in an isothermal case is equivalent to the density ratio.

Summary of the results can be seen in Table 3.4. The tabulated relative errors come from the areas of the tube which have the largest local truncation error (LeVeque et al., 1997, §4.1.1 and §4.1.2), therefore we can safely claim that even for strong shocks *our method is first-order convergent*, i.e. the global relative error scales with the (first power of the) relative grid resolution. A moderate shock, with $\varrho_L : \varrho_R = 2 : 1$, results in even smaller relative errors (again, cf. Table 3.4), but still within the order expected from the relative grid resolution.

Table 3.4: Flow variables

$\varrho_L : \varrho_R$	n_{grid}	value	U	c_T^{\S}	ϱ_C^{\ddagger}	u_C^{\ddagger}
200	100	analytic	2323.46	715.08	$5.2788 \cdot 10^{-12}$	2103.383
		numerical	2273.11	765.41	$5.0552 \cdot 10^{-12}$	2141.305
		relative error	$2.2 \cdot 10^{-2}$	$7.0 \cdot 10^{-2}$	$4.2 \cdot 10^{-2}$	$1.8 \cdot 10^{-2}$
200	1000	analytic	2323.46	715.08	$5.2788 \cdot 10^{-12}$	2103.383
		numerical	2318.08	718.20	$5.2578 \cdot 10^{-12}$	2103.453
		relative error	$2.3 \cdot 10^{-3}$	$4.3 \cdot 10^{-3}$	$4.0 \cdot 10^{-3}$	$3.3 \cdot 10^{-5}$
200	10000	analytic	2323.46	715.08	$5.2788 \cdot 10^{-12}$	2103.383
		numerical	2321.57	715.62	$5.256 \cdot 10^{-12}$	2103.662
		relative error	$8.2 \cdot 10^{-4}$	$7.5 \cdot 10^{-4}$	$6.0 \cdot 10^{-4}$	$1.3 \cdot 10^{-4}$
2	100	analytic	850.01	715.08	$7.0650 \cdot 10^{-11}$	248.44350
		numerical	849.86	714.21	$7.0599 \cdot 10^{-11}$	248.44225
		relative error	$1.8 \cdot 10^{-4}$	$1.2 \cdot 10^{-3}$	$7.2 \cdot 10^{-4}$	$5.0 \cdot 10^{-6}$
2	1000	analytic	850.01	715.08	$7.0650 \cdot 10^{-11}$	248.44350
		numerical	849.94	714.95	$7.0644 \cdot 10^{-11}$	248.44291
		relative error	$8.2 \cdot 10^{-5}$	$1.8 \cdot 10^{-4}$	$8.5 \cdot 10^{-5}$	$2.1 \cdot 10^{-6}$
2	10000	analytic	850.01	715.08	$7.0650 \cdot 10^{-11}$	248.44350
		numerical	850.00	715.06	$7.06496 \cdot 10^{-11}$	248.44337
		relative error	$1.2 \cdot 10^{-5}$	$2.8 \cdot 10^{-5}$	$5.6 \cdot 10^{-6}$	$5.2 \cdot 10^{-7}$

\ddagger numerical value averaged over the entire central region

\S numerical value for the speed of the head of the rarefaction wave, estimated at grid-cell j for which $(\varrho_L - \varrho(r_j))/\varrho(r_j) \approx 0.01$, see text for discussion

Figs. 3.9, 3.10, and 3.11 depict simulation of the strong shock, for three different grid resolutions, at different times. Figs. 3.12, 3.13, and 3.14 are the enlargements of the interesting regions of the shock tube. Those plots reiterate the result from Table 3.4, that solution converges towards the analytical one with the increase of the number of grid points.

The position of the head of the rarefaction wave needs to be precisely determined, in order to estimate the isothermal sound speed from the numerical result for the propagation of the head of the rarefaction wave. This is generally not easy (see e.g. middle left plot of Fig. 3.13). We decided to choose the value r_{RWhead} such that the relative density deviation

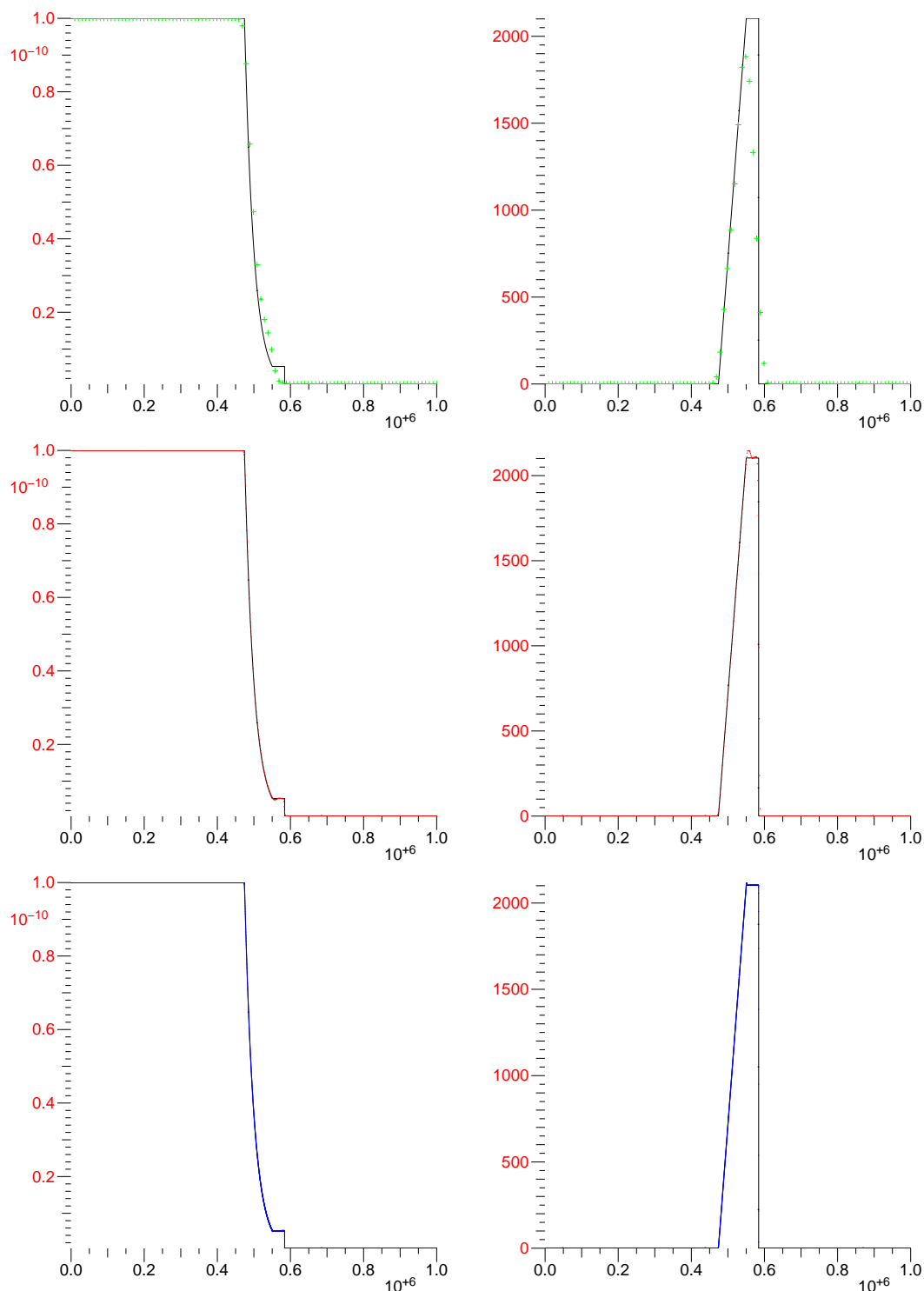


Figure 3.9: Shock tube density (left) and velocity (right) profiles at $t=37$ s. From top to bottom: the green grid has 100, the red 1000, and the blue grid has 10000 points. Black solid line is the analytic solution. Note that individual points are plotted (as visible at the shock front and in the rarefaction wave), but they combine into a line at flatter parts of the solution.

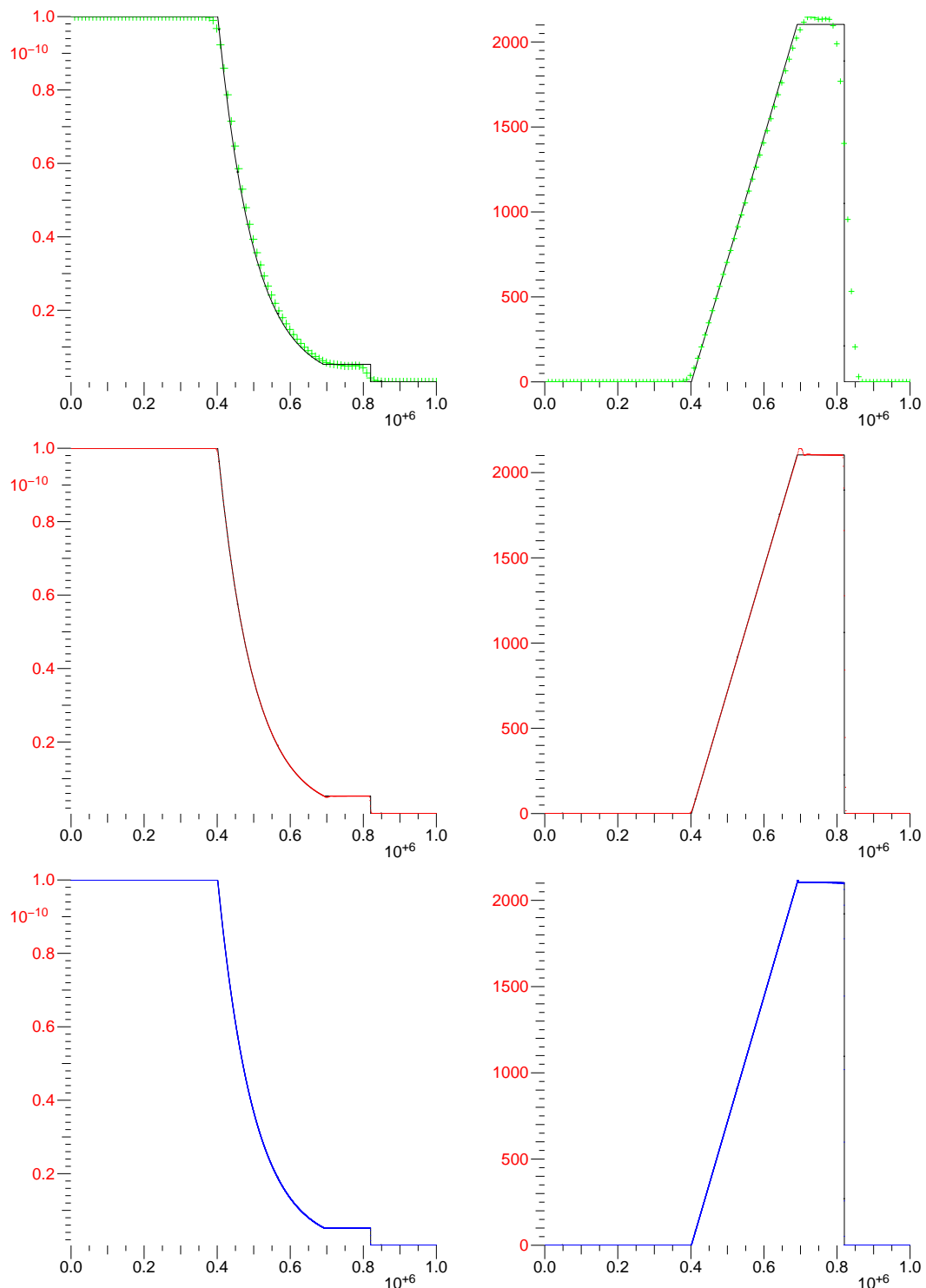


Figure 3.10: Shock tube density (left) and velocity (right) profiles at $t=138$ s. From top to bottom: the green grid has 100, the red 1000, and the blue grid has 10000 points. Black solid line is the analytic solution. Note that individual points are plotted (as visible at the shock front and in the rarefaction wave), but they combine into a line at flatter parts of the solution.

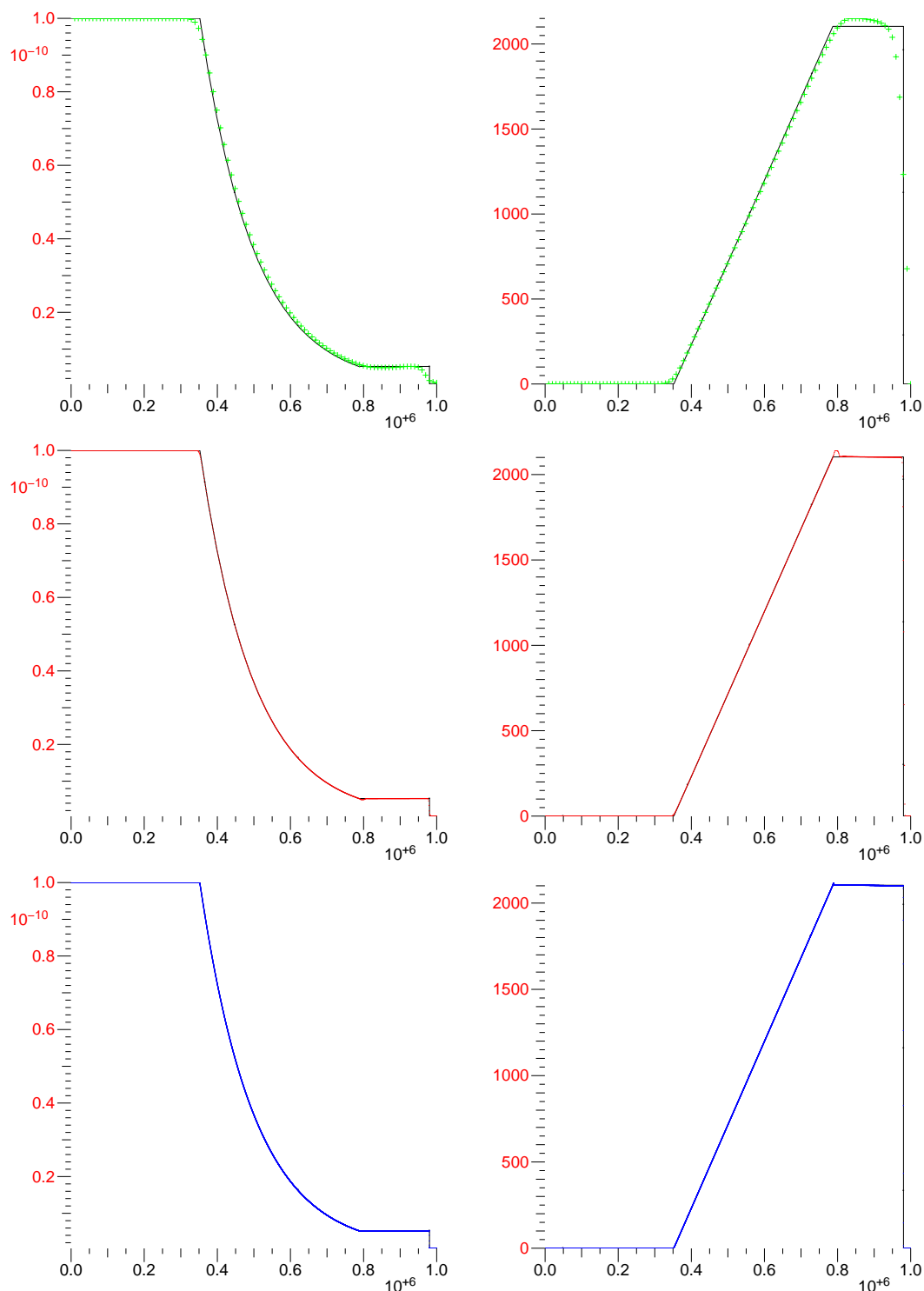


Figure 3.11: Shock tube density (left) and velocity (right) profiles at $t=207$ s. From top to bottom: the green grid has 100, the red 1000, and the blue grid has 10000 points. Black solid line is the analytic solution. Note that individual points are plotted (as visible at the shock front and in the rarefaction wave), but they combine into a line at flatter parts of the solution.

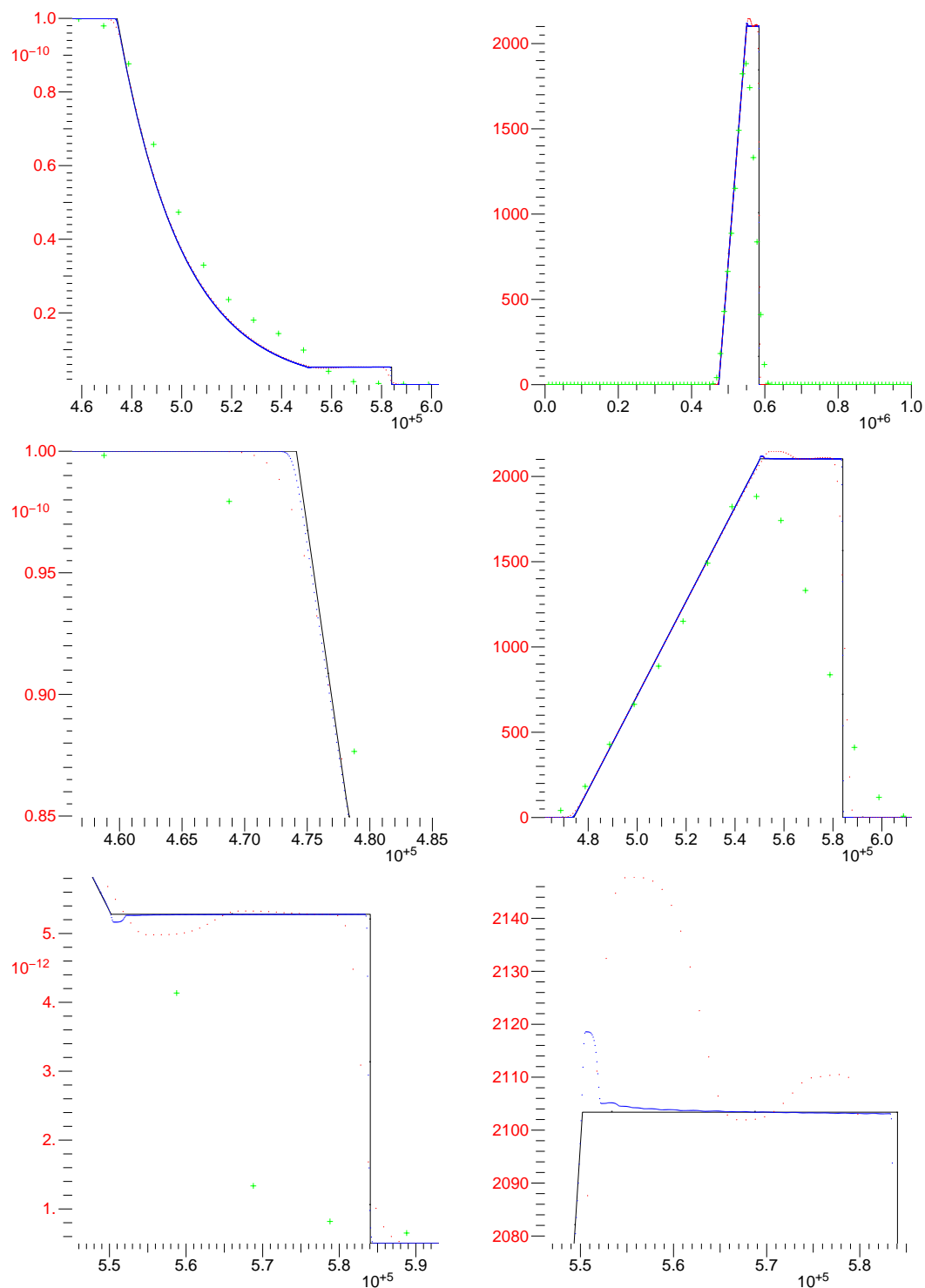


Figure 3.12: Shock tube density (left) and velocity (right) profiles at $t=37$ s, enlargements of the various regions. Three grids are overplotted: 100 cells (green points), 1000 cells (red points), and 10000 cells (blue points). Black solid line is the analytic solution. For additional orientation use Fig. 3.9.

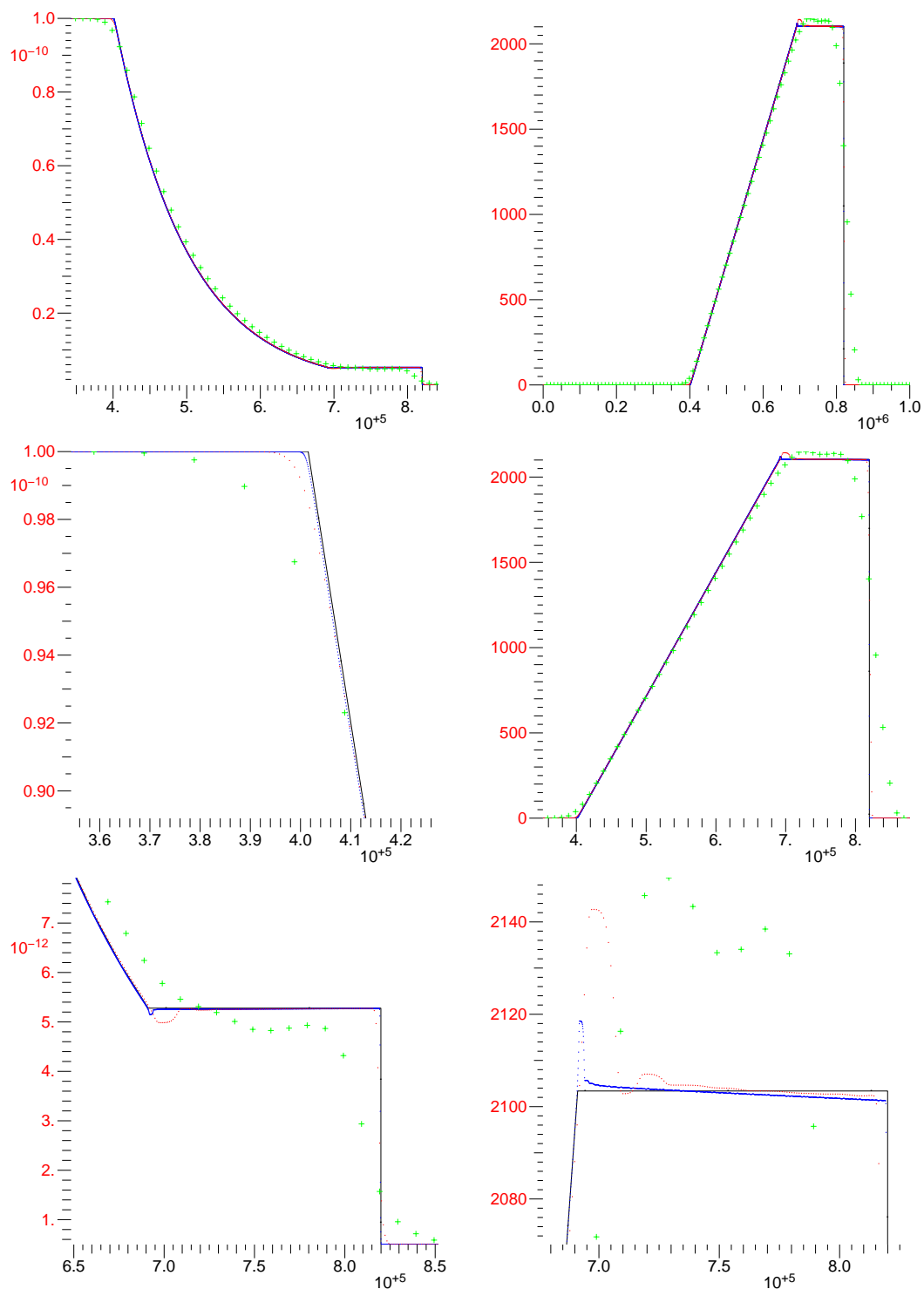


Figure 3.13: Shock tube density (left) and velocity (right) profiles at $t=138$ s, enlargements of the various regions. Three grids are overplotted: 100 cells (green points), 1000 cells (red points), and 10000 cells (blue points). Black solid line is the analytic solution. For additional orientation use Fig. 3.10.

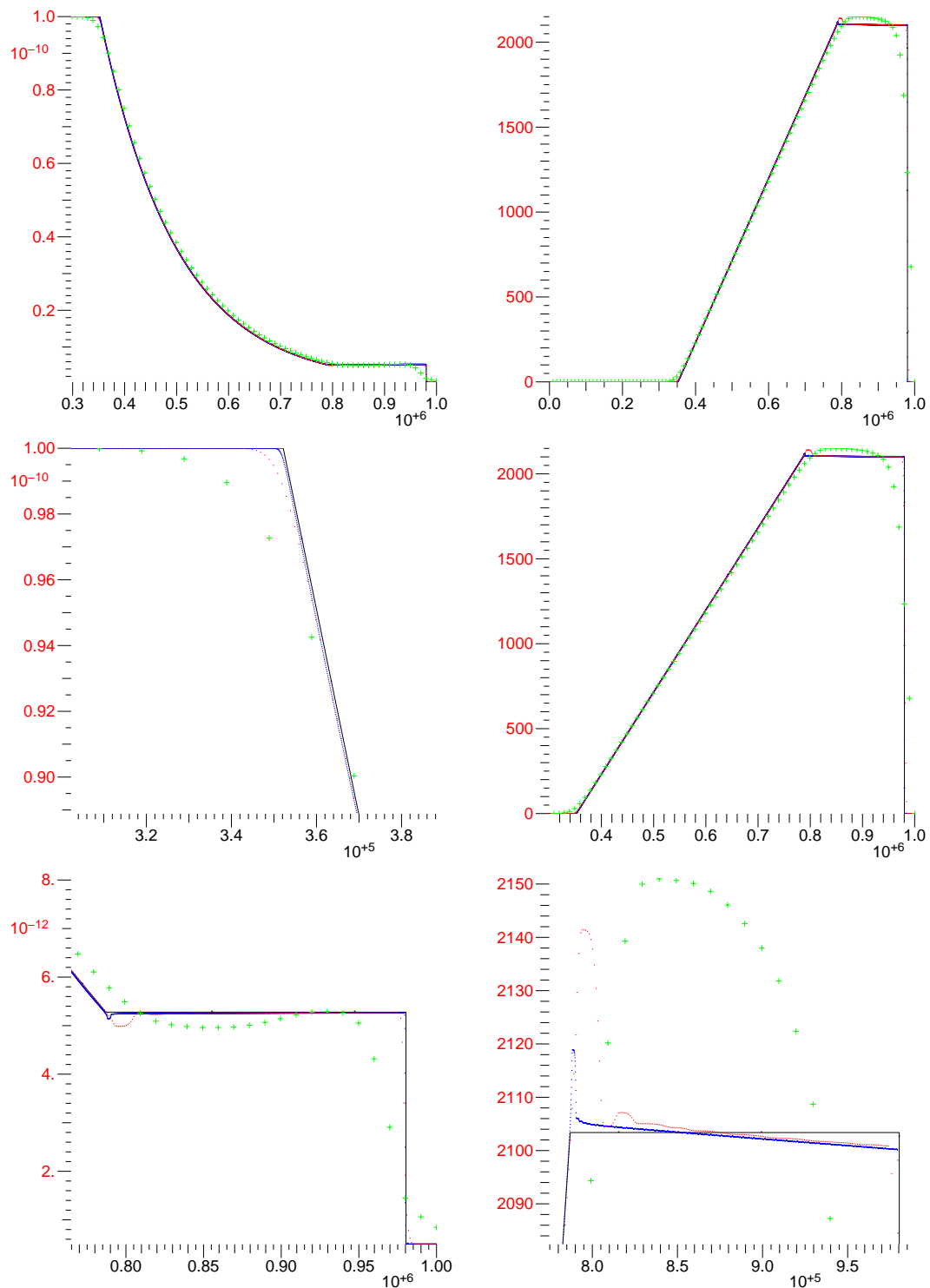


Figure 3.14: Shock tube density (left) and velocity (right) profiles at $t=207$ s, enlargements of the various regions. Three grids are overplotted: 100 cells (green points), 1000 cells (red points), and 10000 cells (blue points). Black solid line is the analytic solution. For additional orientation use Fig. 3.11.

from the unperturbed level, $(\varrho_L - \varrho(r_j))/\varrho(r_j)$, is about one percent.

The value for the position of the shock, needed to calculate the numerical shock velocity, is taken from the half-height of the shockwave's pressure step. Numerical values for the flow variables of the central region are calculated by averaging the respective flow variables across the entire central region. The (maximum) relative deviation from the average value is on the order of the relative grid resolution - $2 \cdot 10^{-3}$ for the 1000-cell grid.

First 45 minutes

By observing the time series of the gas densities at the tube walls for the moderate shock (cf. upper plots of the Fig. 3.15), i.e. noting the clearly correctly reflected density value and its non-oscillating nature, we infer that the reflection at the tube walls, as well as interaction of shock- and rarefaction-wave, does not noticeably reduce the quality of the results on a timescale of a few sound-crossing times.

In the following paragraphs we discuss the evolution of the strong shock case, which is shown on the lower plots of the Fig. 3.15.

A strong shock will force the tail of the rarefaction wave to follow the initial direction of the shockwave with the absolute supersonic velocity $u_{\text{RWtail}} = u_C$ (labels used here conform to Fig. 3.8). The gas velocity in the rarefaction wave itself smoothly decreases from $u(r_{\text{RWtail}}) = u_C$ to $u(r_{\text{RWhead}}) = 0$.

Furthermore, a shock represented with the numerical scheme is spread over several grid cells, which means that moments before the shock front hits the wall, it will no longer interact with the zone of quiet - initial 'right' zone ($\varrho_{\text{quiet}} = \varrho_R$, $u_{\text{quiet}} = u_R = 0$), but instead with the flow variables which are slightly deviating from the 'quiet' flow variables. The shock-front interaction with this deviation just before the reflection will produce the overshoot in the gas density behind the shock. This relatively small effect is greatly amplified at the reflection, and the reasons for the strong amplification are two-fold - the shock is strong, and the gas is isothermal. The amplification of the pressure on the wall

for the strong shock is given by the Courant and Friedrichs (1948, §70):

$$\frac{P_{C\text{post}} - P_R}{P_C - P_R} = 2 + \frac{1}{\frac{P_R}{P_C} + \mu^2} \quad (3.3.21)$$

where P_R is pressure in the zone of quiet, P_C is the pressure behind the shock, and $P_{C\text{post}}$ is pressure behind the shock after the shock-reflection; the constant μ is defined as

$$\mu^2 = \frac{\gamma - 1}{\gamma + 1}, \quad (3.3.22)$$

which for an isothermal case of $\gamma = 1$ amounts to $\mu = 0$, thus the observed large amplification of the overshoot (cf. lower right plot on Fig. 3.15, around $t = 240$ s). In the case of the moderate shock, the amplification is less than a factor of 3, and the consequence of the density-overshoot at the shock-front-reflection is not visible at the shown scale (upper right plot of Fig. 3.15).

At $t = 210$ s shock front hits the right wall and reflects to the left, but is slowed down by the supersonic gas flow region created behind the shock before the reflection. Immediately after the shock front hits the wall, the gas velocity behind the shock drops to zero - gas bounces off the wall with $-u_C$, but incoming u_C gas results in zero absolute velocity. Approximate zero absolute gas velocity, but high relative velocities ($\approx 2u_C$), combined with the density-overshoot at the shock reflection, result in the subsequent series of under- and over-shoots, i.e. in the oscillatory behavior around the correct value for the gas density behind the front, on a percent-relative-level. With zero gas velocity behind the front, the reflected front now serves as ‘the wall’ and, as long as the gas incoming to the front has the constant flow variables of u_C and ρ_C , front slowly moves to the left but the density behind the front stays the same.

However, as the back part of the rarefaction wave hits the front around $t = 360$ s, incoming gas velocity decreases linearly, but the incoming density increases exponentially. The net advected mass across the front from left to right, ρu , is increased, as is the gas density (at the right wall), which damps out the density oscillation.

On the left side, at around $t = 700$ s head of the rarefaction wave (HRW) hits the wall.

After that, density fall-off at the left wall is slower compared to the moderate shock case (compare exponential drop-off for the left plots of Fig. 3.15) because rarefaction wave for the strong shock case is more spread out. But more importantly, as the HRW passes back through the tube, it drags the gas behind it as a subsonic wave. This further increases the absolute gas velocity, and flattens the exponential density profile of the initial rarefaction wave.

At around $t = 1700$ s, the HRW passes the reflected shock front, which adds a slight linear component to the front-incoming gas velocity, but replaces the exponential rise of the front-incoming gas' density with the exponential fall-off (the same one which is seen on the bottom left plot of the Fig.3.15). From that moment, net mass is advected across the front from the right to the left, resulting in the decrease of the density (right of the front, and including the right wall).

Finally, around $t = 2200$ s subsonic front hits the left wall.

Conclusion

Overall, the hydrodynamic scheme proved convergent, stable and able to compute the propagation of the simple waves correctly to the (order of the) first power of the relative grid resolution, which is in agreement with the expected performance for a first-order scheme (LeVeque et al., 1997, §4.1.1). We also show that the 1000-cell grid can resolve strong shocks, but at the same time the calculation is fast enough that evolution can be followed on a time-scale of a hundred sound-crossing times.

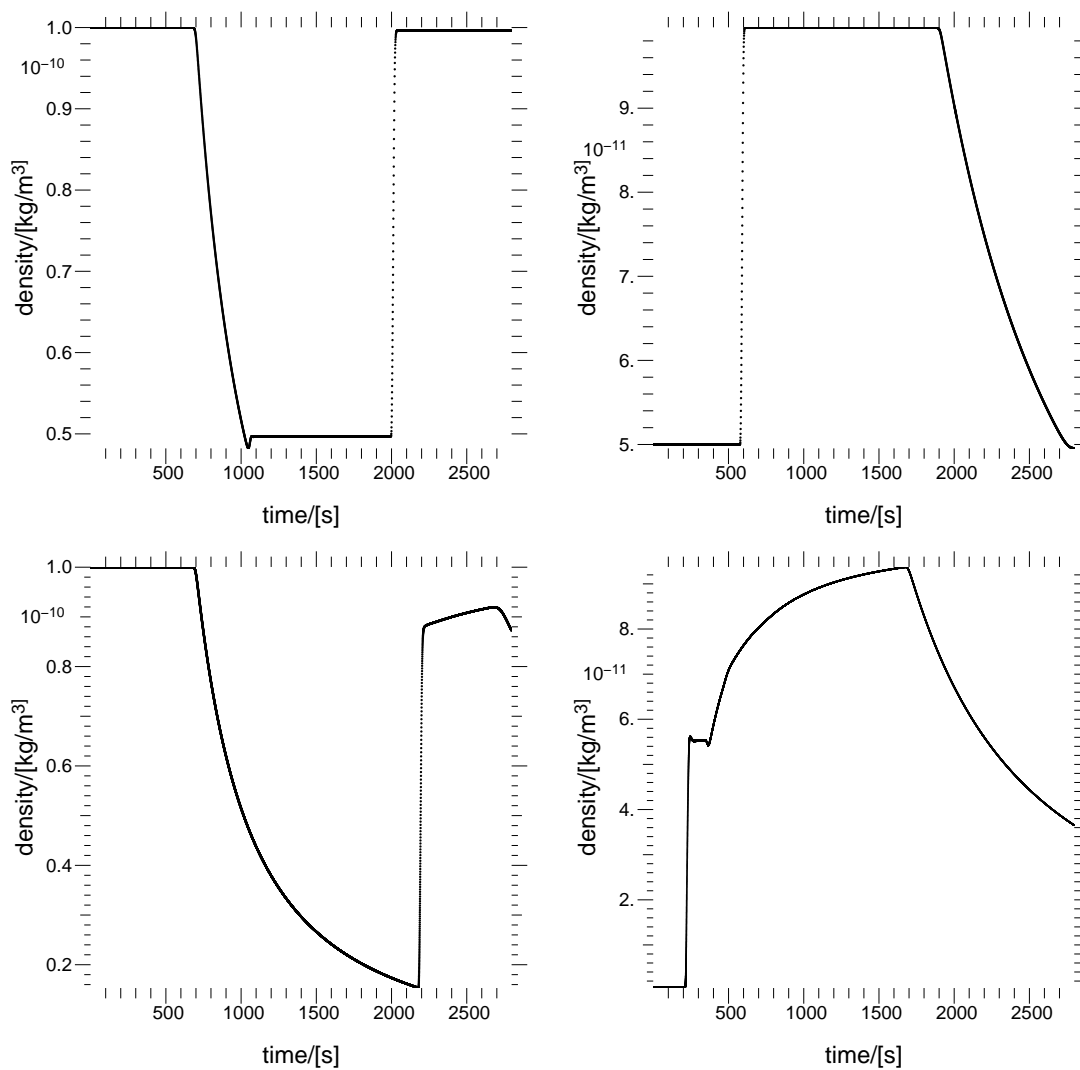


Figure 3.15: Time-evolution of the densities at the left (left plots) and the right (right plots) tube wall, for a weak (top plots) and a strong (bottom plots) shock. Evolution is followed for two sound-crossing times, and every tenth time level is represented with a point on a plot. The interaction of the strong shock and the rarefaction wave makes the strong shock plots more difficult to interpret than for the weak shock case. See text for the discussion.

3.4 Hydro-dynamical surveys

Manifold survey - non-linear stability analysis

The linear analysis can distinct a (linearly) stable from an unstable protoplanetary model, but it cannot be used to discover where the instability leads to, even more so for an intrinsically non-linear system. Additionally, the linear stability analysis is limited only to the small envelope perturbations. As we have learned from our own planetary system, planet formation involves ‘large perturbations’, i.e. giant impacts (e.g. see the rotational axis of Uranus, or the Earth-Moon system, or Mars’ Schiaparelli crater-Valles Marineris canyon system, etc).

Thus we perform a non-linear analysis of all qualitatively different protoplanets, using (the typical representatives of) the equilibria from our static classification as initial states for hydro-dynamic simulations.

Initial perturbation, due to the difference between the static and dynamic discretizing schemes, is proportional to the density gradient and can be regarded as small (see Sect. 3.2). However, this setup could also be used for the analysis of the core-envelope equilibria under large perturbations.

Envelopes have 1000 log-equidistant grid-points in radius, unless otherwise specified. Such grid density is sufficient to have results correct on a 10^{-3} level, as is expected from a first order scheme and as we have shown in the scheme tests (see Sect. 3.3).

Dynamical indicators

Simple but complete data representation of the complex system is at least as important as the data analysis. We had a wide choice of possible variables as indicators for the envelope dynamics: core-surface density, mass flow across the boundary, maximum (positive/negative) gas velocity, gravitational energy, total energy, free energy, entropy, and many others.

We decided to use two indicators: envelope's gravitational energy, and the extremal gas velocities (largest positive and negative). Such choice of the dynamic indicators provides relatively intuitive and complete overview of the envelope evolution.

The gravitational energy is a partially degenerate indicator, measuring the envelope mass, but also the envelope compactness. The degeneracy is resolved with the other indicator, extremal velocities, which offer an insight into the type of dynamics at work (e.g. accretion shock vs pulsation vs slow oscillation...). For a brief discussion about choosing extremal velocities over velocities at the outer boundary, see Sect. 3.4.3: *Dynamical properties and the core density*.

The gravitational energy is defined by (e.g. Kippenhahn and Weigert (1990)),

$$E_{\text{grav}} = - \int_0^M \frac{Gm}{r} dm, \quad (3.4.1)$$

or, in its discretized form:

$$E_{\text{grav}} = \sum_j 4\pi \frac{GM(r_j)}{r_j} \cdot \varrho_j \cdot \Delta \text{Vol}_j. \quad (3.4.2)$$

To be able to get meaningful comparison of the envelopes with the different masses and different radial structures, all envelope gravitational energies are normalized to their respective initial gravitational energy:

$$n_{\text{grav}} = \frac{E_{\text{grav}}(t)}{E_{\text{grav}}(t_0 = 0)}. \quad (3.4.3)$$

Core mass sequences

Regarding the mass of the core, there are three qualitatively different regions:

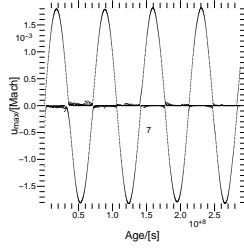
1. the subcritical cores
2. the cores in the vicinity of the critical core mass
3. the supercritical cores

With this in mind, we will perform dynamical investigations of the sequences of the models which will cover all dynamically qualitatively different cores. A particular model sequence will, additionally, cover all different envelope configurations for a corresponding core.

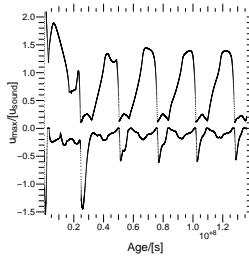
As already discussed in Sect. 1.3.2, statically there are four qualitatively different envelope types, depending on whether the solution is compact or uniform and self-gravitating or not. Those different envelope types form four distinct regions in the solution manifold (cf. e.g. Fig. 1.2). Surveys in Sect. 3.4.3 and 3.4.2 will investigate whether the envelopes within a particular region have similar dynamical properties. Therefore our discussion will be based on the stability properties of different manifold regions.

3.4.1 Types of dynamical behavior

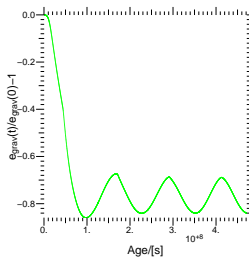
The following types of dynamical behavior were noticed within the survey of models with a medium core density: *oscillation*, *pulsation*, *transition*, *ejection*, and *collapse*.



Oscillation - The envelope oscillates around a particular, stable equilibrium. The oscillation is caused by an initial perturbation, and is maintained because of the specific boundary conditions, which (partly) permit/enable a wave reflection. Such an initial perturbation is small enough to preserve the initial envelope structure.

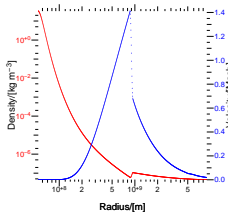


Pulsation driven by possible intrinsic non-linear instability - The envelope's equilibrium state undergoes a cyclic dynamical pattern. Equilibrium's meta-stability generates the (envelope gas) velocity field. The envelope is marginally unstable and as it is forced out of the equilibrium structure it becomes stable and returns to its (meta-stable) equilibrium. Such an equilibrium is too deeply bound to be destroyed with a self-regulating instability, and the envelope remains in a cyclic dynamical pattern (e.g. models 29, 30, and 31 on Fig. 3.21).



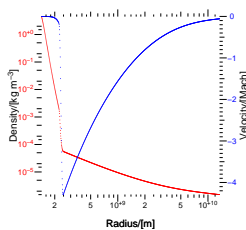
Transition - The envelope exchanges one equilibrium for the other. All of the observed transitions happened after finite perturbation. The envelope mass of the end state could either be higher or lower than the envelope mass of the initial state. The end state is *always* in the 'nebula' region, except for the cases with the collapsing envelopes. Thus, in all the observed cases (within this work) the end state had smaller gas density at the core surface than the initial state. As an example

of the transition, with identified initial and end states, see Fig. 3.22 and accompanying discussion.



Ejection - An ejection is initiated by the envelope dynamics.

Similarly to collapse, an instability is excited which produces the velocity field. However, this velocity field is *positive*, unlike the one for collapsing models. The field grows, becomes supersonic, and continues to grow, trying to pull the compact part of the envelope away from the core. The potential of the compact envelope part (plus the core potential) slows the growth of the velocity field (c.f. Fig. 3.21, e.g. model 42, around $\text{Mach} \approx +2$). This situation is analogous to increase in resistance to the piston which forcefully tries to open an under-pressurized vessel. During all that time the innermost envelope structure is virtually unchanged, and still gives rise to the instability-induced velocity field. The velocity field finally rips the compact envelope part from the surface of the core, envelope structure is completely destroyed, and consequently with it also the instability-induced velocity field. The envelope is then in a transition to a new equilibrium.



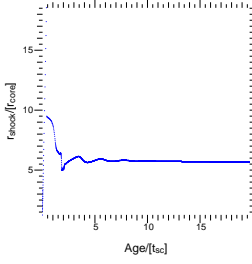
Collapse - A collapse is initiated by the envelope dynamics. The

outer part collapses onto a dense inner stratification, which forms a new, effective core. If an envelope in collapse is connected to a dilute nebula, the flux of matter falling onto the effective core is insignificant and the structure of the inner envelope part is preserved. However, if the significant amount of material is present in the outer envelope part, then the shock-front of collapsing matter reduces the radius of the effective core. The squeezing continues until essentially the complete initial envelope structure is destroyed and the whole envelope collapses in a free-fall-like manner onto the model's core surface.

We discuss these two kinds of the envelope collapse in a bit more detail in a section below.

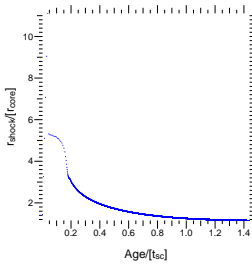
Two kinds of collapse

After a careful inspection of collapsing envelopes in our surveys, we noticed two different versions of the collapse evolution.



‘Slow’ collapse - In the first case, envelope does not have a significant mass above the compact inner part. When a collapse starts, the dilute outer part hits the effective core in a free-fall like manner. Because the density in the outer stratification is low, the momentum deposited onto the effective core is too small to be relevant, and the effective core radius stays almost constant in

time. The only contribution to the increase in the gravitational energy of the envelope by the in-falling mass flux (increase because the gravitational energy is defined with the positive sign - c.f. Eq. 3.4.1). Such an envelope has (to a very good approximation) a linear increase of the gravitational energy with time. Good examples are i.e. models 15 to 21 on Figs. 3.25 and 3.26. We dubbed such collapse - a *‘slow collapse’*, because the momentum flux, which forces the radius of the effective core to reduce, is dominated by the velocity component, while the mass component does not contribute significantly.



‘Fast’ collapse - In the second case, envelope has a massive outer stratification above the compact inner part. Thus, the momentum, carried with the supersonic flow onto the effective core, forces the compact inner part to further reduce its radius. This gives the additional component to the increase of the envelope gravitational energy, along with the incoming mass flux. Such an envelope has

a non-linear increase of the gravitational energy with time; for example, models 1 to 4 on Figs. 3.25 and 3.26. This type of collapse we named a *‘fast collapse’*, because the in-falling momentum flux has significant contributions both from the (gas and advected) velocity and the advected mass. Please note that in special cases (for the very large advecting velocities) the *‘slow’* collapse can happen on timescales shorter than the *‘fast’* collapse.

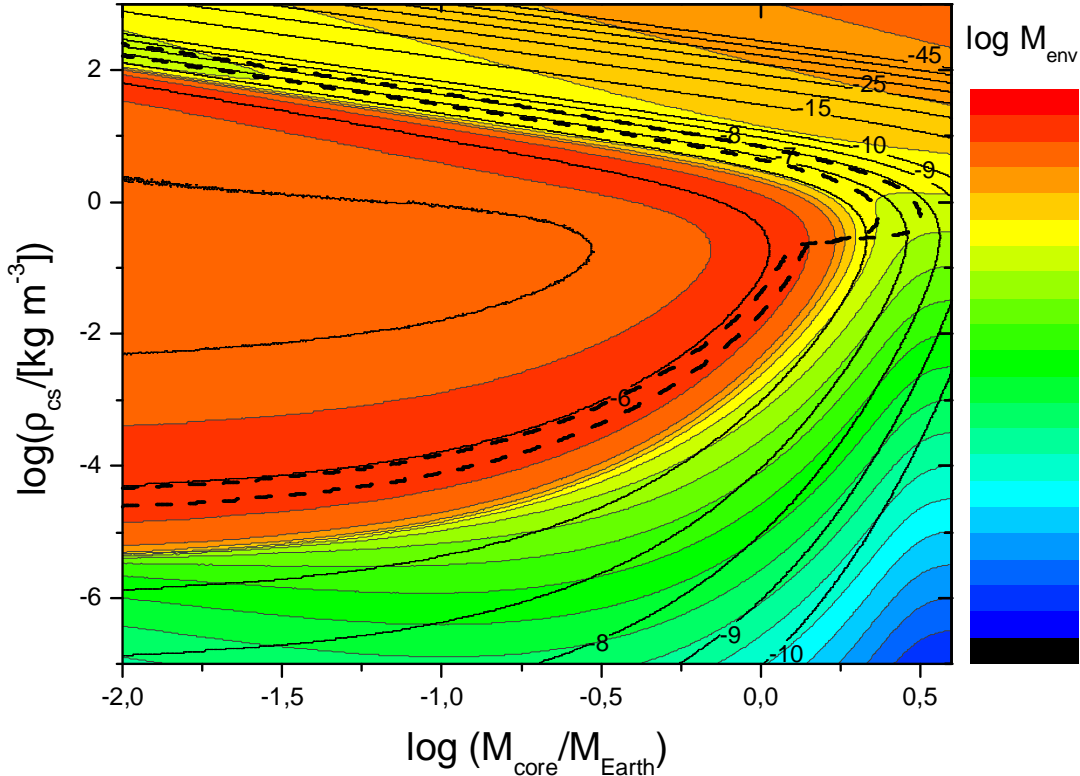


Figure 3.16: Nebula density contour plot of the solution manifold for $\rho_{\text{core}} = 1 \text{ kg m}^{-3}$, $a = 5.2 \text{ AU}$, and $T = 123 \text{ K}$. Color contours show the logarithm of the envelope mass in M_{\oplus} according to the legend. Thick dashed lines mark the region of linear stability, each line standing for different outer boundary stability condition for the linear dynamics; cf. Schönke (2005). Solid black lines are contours for different nebula densities, and labels represent logarithm of the nebula density in SI units. Raw manifold data for this figure courtesy of J. Schönke, AIU Jena.

3.4.2 Medium core density

The investigation of the dynamics of the solution manifold with $\rho_{\text{core}} = 1 \text{ kg m}^{-3}$ is an attempt to address both the prohibitively short time-step of the high-core-density models and the qualitatively different dynamics of the low-core-density models.

Inspecting the linear analysis of the models equivalent to ours, Schönke (2005), we decided that the ideal core density for the hydrodynamical investigation would be $\rho_{\text{core}} = 1 \text{ kg m}^{-3}$, because it allows large time coverage. Furthermore, the solution manifold with such a core density (Fig. 3.16) has very similar linear-stability properties to the solution manifold with the realistic core densities (i.e. $\rho_{\text{core}} = 10^3 \text{ kg m}^{-3}$). Thus we expect that the dynamical

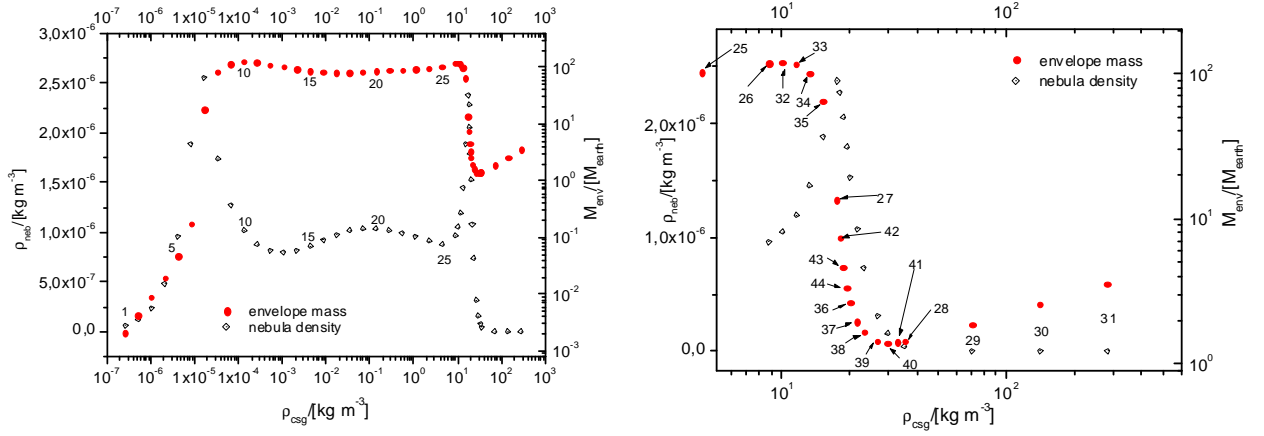


Figure 3.17: Manifold cut for a typical subcritical core ($\log(M_{\text{core}}/M_{\oplus}) = -1$, with $\rho_{\text{core}} = 1 \text{ kg m}^{-3}$ core density (complete manifold on Fig. 3.16)). Numbers identify different models, shown in Figs. 3.19 and 3.20.

properties of the mid core density models will also correspond to the dynamical properties of the high core density models.

Subcritical core mass model sequence

We choose a typical subcritical core mass with $\log(M_{\text{core}}/M_{\oplus}) = -1$ (c.f. Fig. 3.16) for our model sequence. The model sequence can be seen on Fig. 3.17, covering all the different envelope regions according to the classification for the static properties of high core density models (c.f. Chapter 1). For the reasons mentioned in the introductory paragraph to Sect. 3.4.2 we believe such sequence will cover all the qualitatively different dynamical regions (accessible to one particular subcritical core). For the same reasons we believe that the static classification of the models with high core density (c.f. Sect. 1.3.2) will be applicable within this survey. Therefore we divide models into four classes: ‘*mature telluric planet*’, ‘*mature giant planet*’, ‘*nebula*’, and ‘*protoplanet*’.

We start our inspection with the ‘*nebula*’ models (models 1 to 8 from Fig. 3.17):

Envelopes are stable, and the initial perturbation is small. No transition is observed; *envelopes oscillate around the initial equilibrium*. Oscillation is excited with the initial

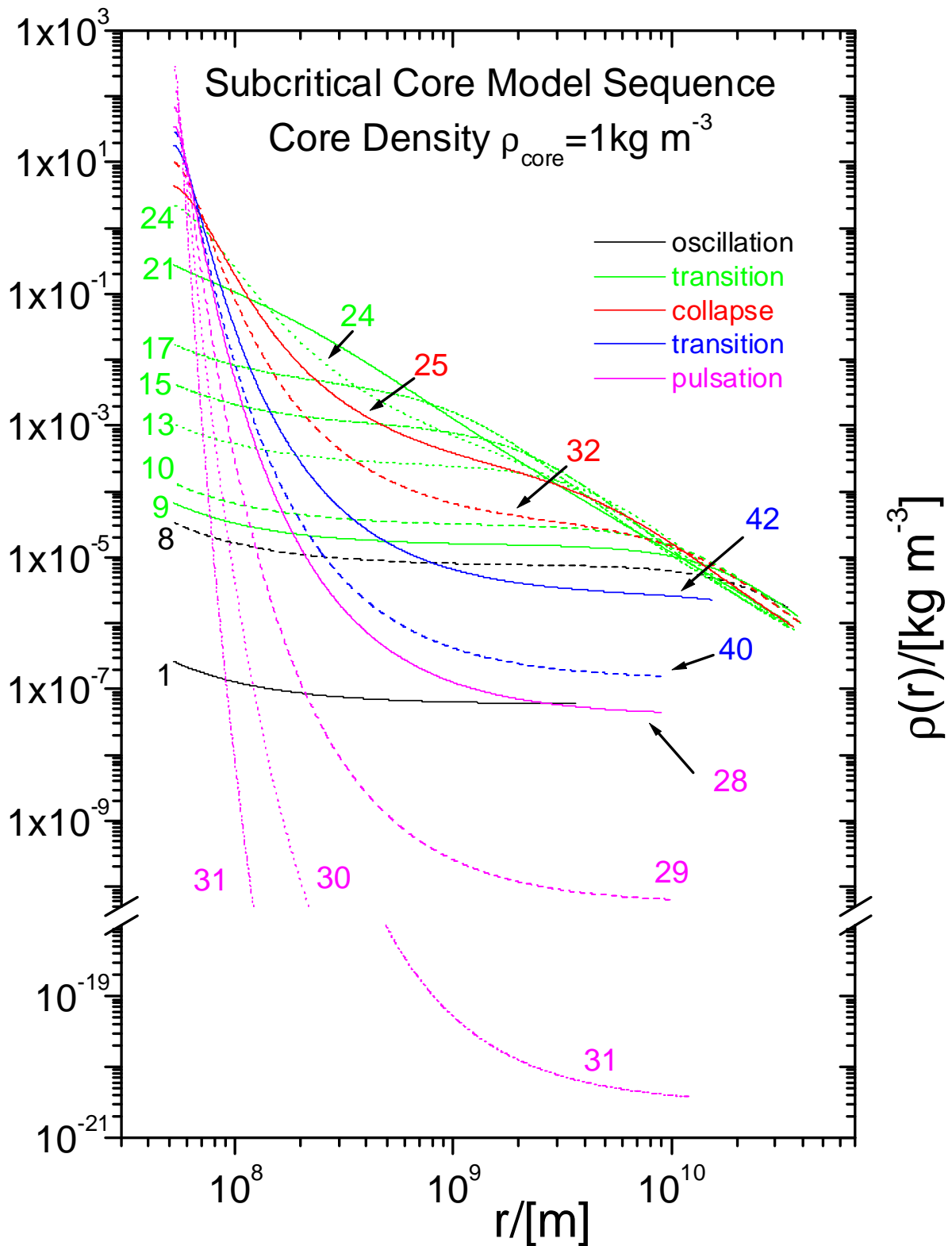


Figure 3.18: Envelope density profiles for different models shown on Fig. 3.17. Color coded lines represent dynamical properties: black - oscillation, green - transition, red - collapse, blue - transition, magenta - pulsation.

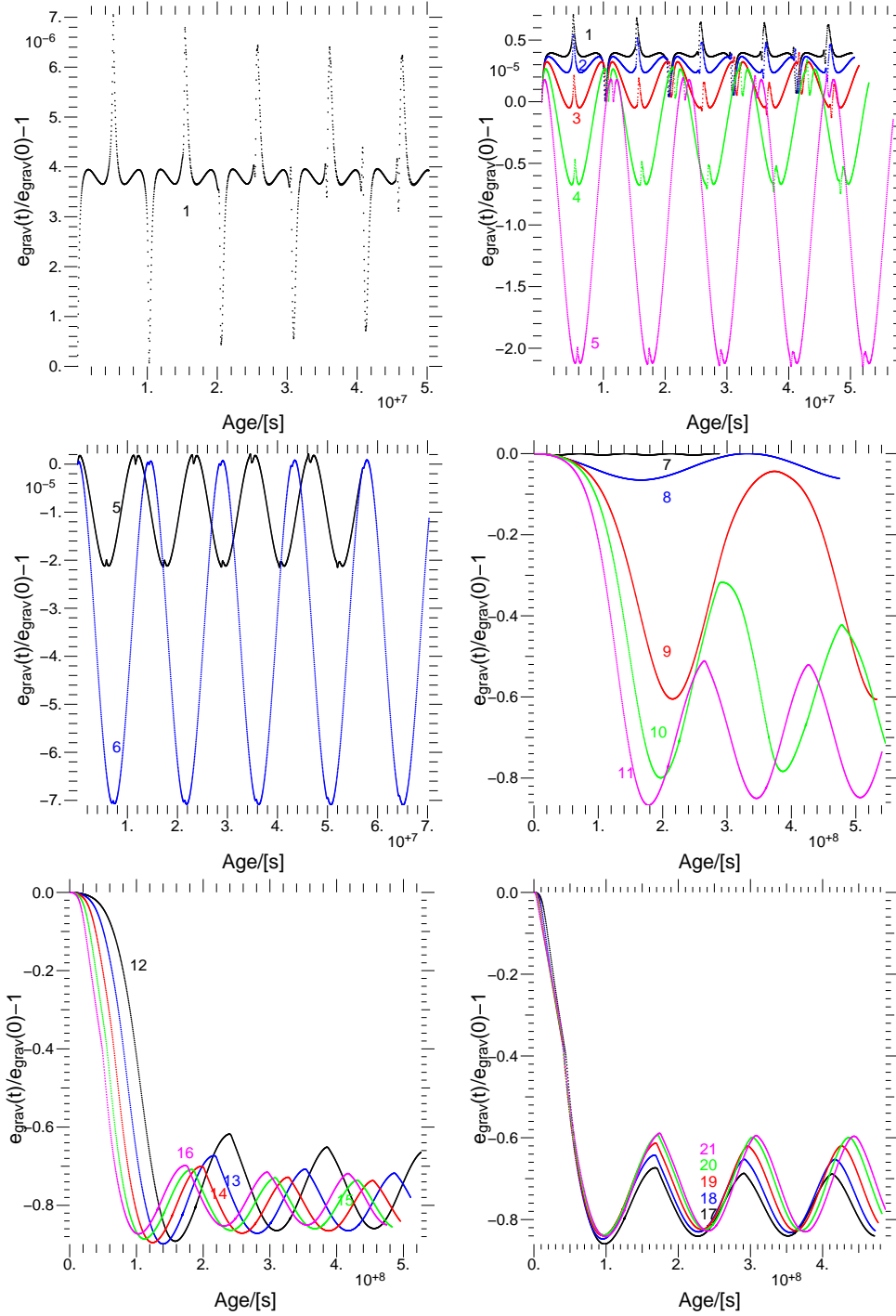


Figure 3.19: Time evolution of the envelope gravitational energy normalized to its initial value, Eq. 3.4.3. Every 100th time level is plotted, and is represented with a dot; dots are not connected. Numbers correspond to models from Fig. 3.17. Color coding is for easier identification. Calculations begin with slightly perturbed hydrostatic profiles. Spikes in curves, for models 1 to 6, represent a reflection of the initial perturbation wave from the outer and the inner boundary. Models 1 to 6 just oscillate, keeping their gravitational energy constant on a 10^{-5} level, while models 9 to 21 make a transition to another state, losing most of their envelope mass. See text for discussion.

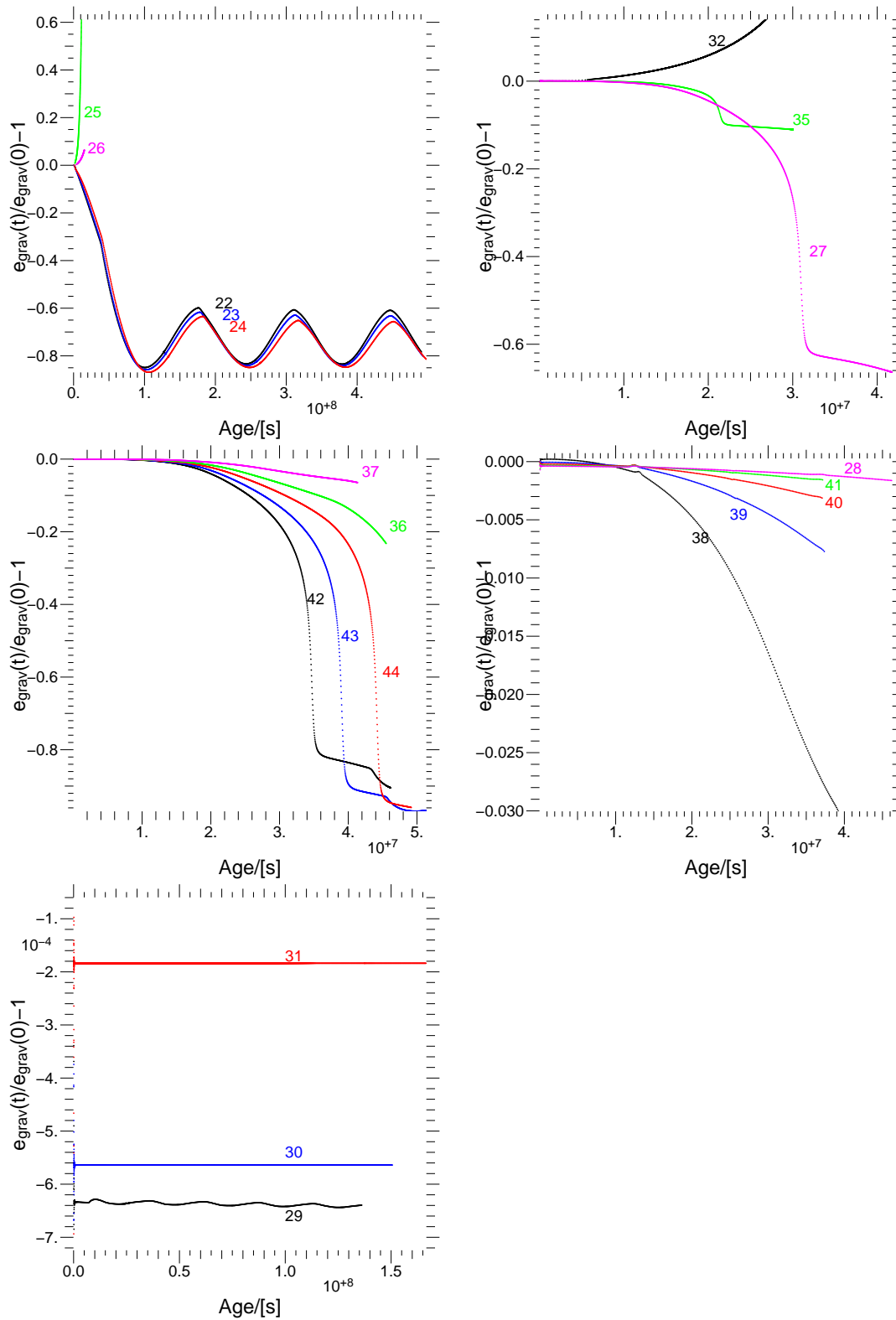


Figure 3.20: Time evolution of the envelope gravitational energy normalized to its initial value, Eq. 3.4.3. Every 100th time level is plotted, and is represented with a dot; dots are not connected. Numbers correspond to models from Fig. 3.17. Calculations begin with slightly perturbed hydrostatic profiles. See text for discussion.

perturbation. Time evolution of the normalized gravitational energy for such models can be seen on Fig. 3.19. Wave amplitude of the typical initial perturbation for such a model is shown as a top right plot on Fig. 3.22. Envelope structure of these models does not significantly change in time, as shown on relevant plots of Fig. 3.19, where we notice an essentially constant gravitational energy.

Further, we look at the ‘low-to-mid gas density at the core surface (ρ_{cs})’ part of the ‘*protoplanet*’ region (models 9 to 24 from Fig. 3.17):

Models are characterized with massive, unstable envelopes. The initial perturbation is strong enough to excite an instability. Models immediately make a transition into the ‘nebula’ region (c.f. plots for these models on Figs. 3.19 and 3.20). After the transition they oscillate similarly to observed oscillation of ‘nebula’ region models (1 to 8), but with a much larger (orders of magnitude larger) amplitude. Such an oscillation is excited with the transition from the initial state. Reflection of the transition-induced perturbation wave, from the core surface and (on a lesser scale) from the outer boundary, can be seen (for models 22, 23, and 24) on a top left plot of Fig. 3.21.

Change in the overall dynamics in the model sequence is slow and gradual, indicating that the instability governing the initial transition to the ‘nebula’ region has linear nature. Additional support for the linear instability case comes from excellent agreement between our analysis and the prediction of the linear stability analysis by Schönke (2005). Envelope mass of the end state is smaller than the envelope mass of the initial state.

Next, we stay in the ‘*protoplanet*’ region, but move to the models with higher ρ_{cs} (models 25, 26, and 32 from Fig. 3.17):

Envelopes are massive, but more compact than models 9 to 24. The initial perturbation is strong enough to excite an effective-core collapse (see plots for these models on Fig. 3.20). As soon as the initial perturbation wave passes over the area of the (soon-to-be) effective

core, the envelope instability pumps up a negative velocity field which grows, exceeds the velocity of sound and becomes a shock, while it continues to grow (see plots for these models on Fig. 3.21). Effective core feeds on the rest of the envelope, and there is almost no mass flux from the nebula as long as there is a significant amount of matter in the outer stratification of the envelope.

The gas density of the effective core is increased with time in accordance with the incoming mass flux from the outer part of the envelope. The outer stratifications collapse in a free-fall-like manner.

Interestingly, the instability intrinsic to the initial state is weaker for the more compact of these models. Thus the resulting collapse will be *more* pronounced for models with *smaller* ρ_{cs} (c.f. plots for these models on Fig. 3.21). This indicates that the nature of the intrinsic envelope instability might be non-linear, since the dynamical behavior changes drastically (from oscillation for model 24 to strong collapse for model 25) for models with relatively similar (initial) stratification (models 24 and 25). An additional argument for the non-linear nature of this instability is that the ('fast' collapse) dynamics of these models is reminiscent of the non-linear dynamics in the vicinity of the critical core mass.

We now inspect the models with the highest ρ_{cs} in the '*protoplanet*' region (models 35, 27, 42, 43, 44, 36, 37, 38, 39, and 40 from Fig. 3.17):

Envelopes are even more compact than models 25, 26, and 32. Like for those models, the initial perturbation excites the instability which produces the velocity field. However, this velocity field is *positive*, unlike the one for a previous group of models, but in accordance with the trend for the collapsing models: the amplitude of the velocity field goes from strongly negative toward more positive values, for the (collapsing) models with increasing ρ_{cs} . The field grows, becomes supersonic, and continues to grow, trying to pull the compact part of the envelope away from the core. The potential of the compact envelope part (plus the core potential) slows the growth of the velocity field (c.f. Fig. 3.21, e.g. model

42, around $\text{Mach} \approx +2$). This situation is analogous to increase in resistance to the piston which forcefully tries to open an under-pressurized vessel. During all that time internal envelope structure is virtually unchanged, and still gives rise to the instability-induced velocity field. The velocity field finally rips the compact envelope part from the surface of the core, envelope structure is completely destroyed, and consequently with it also the instability-induced velocity field. The envelope is in transition to a new equilibrium. The end state will share the density of the surrounding nebula cloud with the initial state, but will be in a ‘nebula’ region.

Figure 3.22, along with plots in Fig. 3.21 featuring model 42 (middle left and bottom right), shows an example of such an event in more detail.

Middle right plot on Fig. 3.22 shows initial state (black points) of models 42, along with the envelope state after 100 sound crossing times of evolution (red lines, the ‘end’ state). This plot is very reminiscent of Fig. 4 in Stahl et al. (1995), who studied thermodynamics of the coreless gas spheres. They formally showed that in their case two states are coexisting, and process of exchanging one for the other is a phase transition. We can not formally make a *phase transition* claim, for lack of the formal thermodynamic analysis, but all the indications point that the transition observed for model 42 is indeed a phase transition.

The last remaining part of this model sequence for increasing ρ_{cs} is the ‘*mature giant planet*’ region with models 28, 29, 30, 31 from Fig. 3.17):

The envelopes are basically versions of the barometric law - a compact inner part is connected to a dilute outer part via an exponential decrease in density. The outer part does not contain massive, self-gravitating stratifications. The initial perturbation again excites the intrinsic-instability-induced positive velocity field. But this time either the potential of the compact inner part is too strong for the structure to be disrupted, or the envelope structure is only marginally unstable (or both). The velocity field does

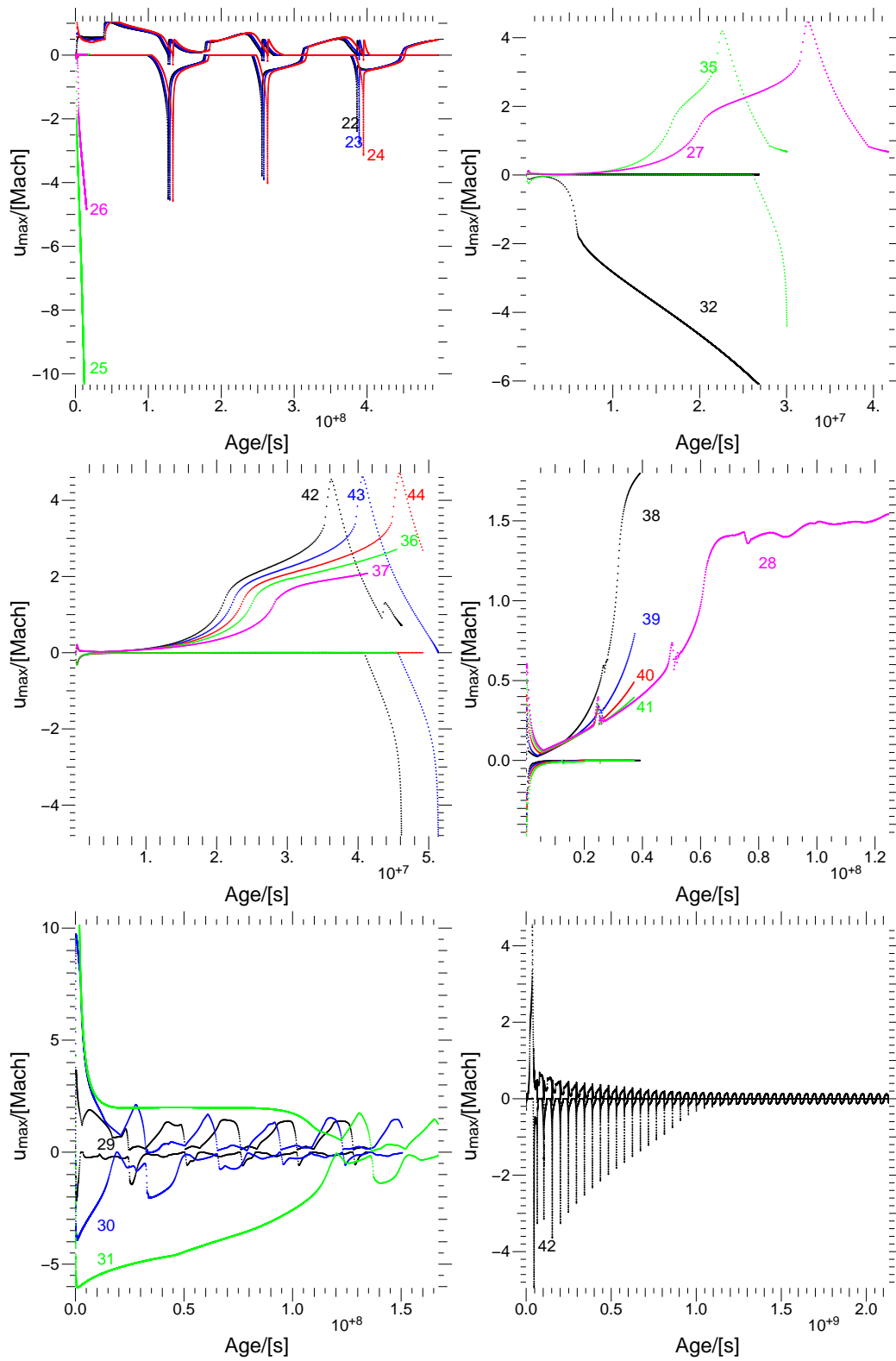


Figure 3.21: Time evolution of the extremal (largest positive and negative) envelope gas velocities. Every 50th time level is plotted. Calculations begin with slightly perturbed hydrostatic profiles. See text for discussion.

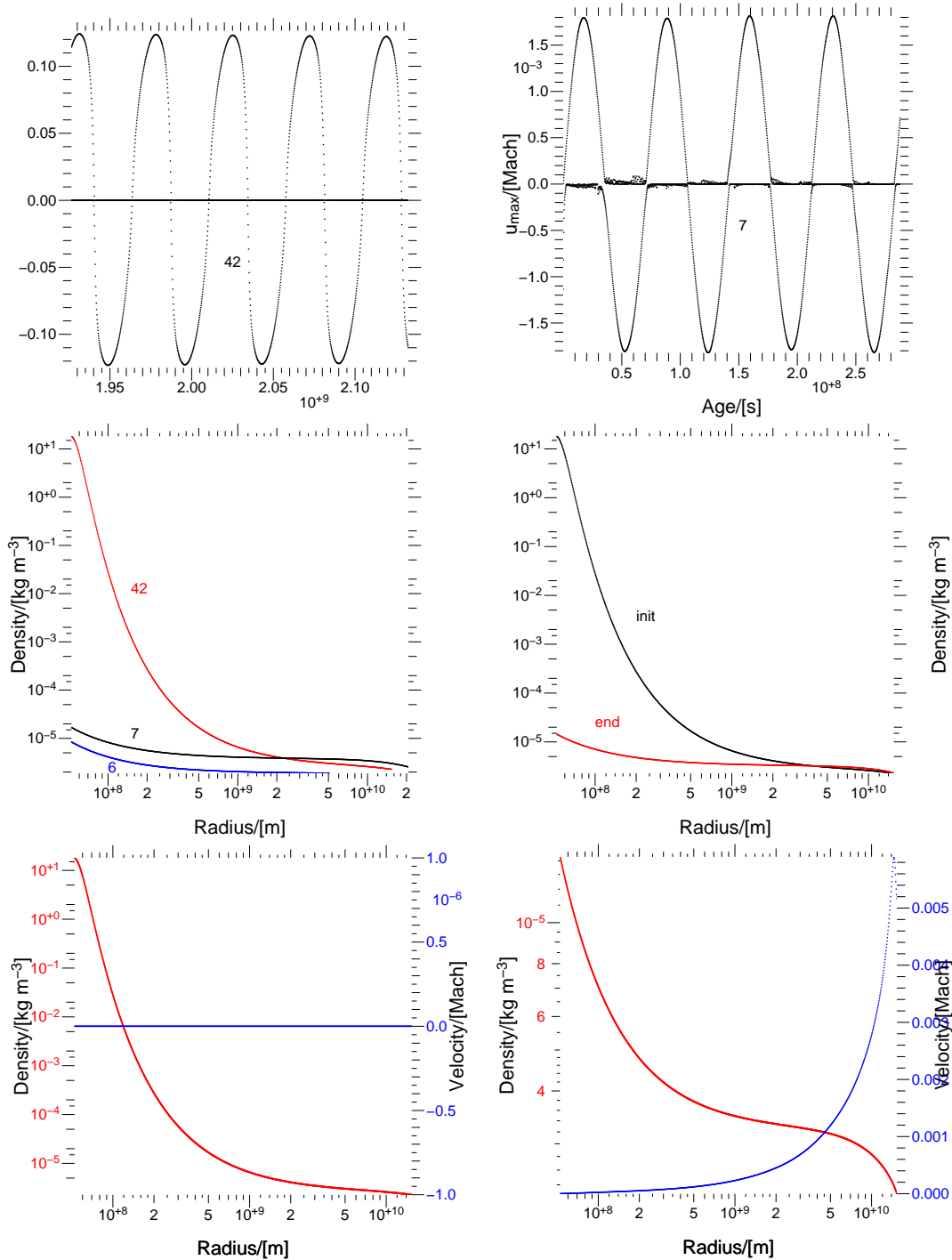


Figure 3.22: **State transition between different envelope regions.** Top row: Time evolution of the extremal (largest positive and negative) envelope gas velocities, for models 42 (left) and 7 (right). Extremal velocities of model 42 are shown after evolving for about 100 sound crossing times (c.f. Fig 3.21 for the initial evolution including the transition). Middle row: Density profiles of models 6, 7, and 42 (left), and density profiles of the initial and the ‘end’ (after $100 t_{sc}$) states of model 42 (right) . Bottom row: After initial perturbation, model 42 (left) made a transition and is oscillating around a radial profile (right) which is reminiscent of model 7 (compare the lower-right density profile of the evolved model 42, with the middle left density profile of model 7).

grow (even to supersonic values), but it is either pushed away from the critical radius by the (reflected) initial-perturbation wave and destroyed on a rigid, dense inner part, or it is self regulated - as soon as it grows to velocities large enough to affect the envelope structure, the structure is changed by the mass flux accompanying the velocity field. With the envelope structure changed, the instability-induced velocity field is weakened or completely destroyed. In any case, such an envelope goes through a (not-strictly) cyclic dynamical pattern, but on the whole it is too stable to be shifted away from the initial (meta-stable) equilibrium (into a new equilibrium). As the structure settles back into the initial stratification, the intrinsic instability rises again, starting another cycle, another (quasi-periodic) pulse (see lower left plot on Fig. 3.21). Throughout the pulse, the overall radial structure is not significantly changed, keeping the gravitational energy (almost) constant in time (see lower left plot on Fig. 3.20)

We noticed a direct analytic relation between the gas density at the core surface and the strength of the perturbation (c.f. bottom left plot of Fig. 3.21); The strength of the perturbation is connected to the duration of transition until envelope reaches the pulsating mode; envelope with 2^n higher value than ρ_x will take t^n time to switch from initial state to pulsating mode. Time t is the duration of the transition into the pulsating mode for the envelope with a ρ_x gas density at the core surface.

The strength of the perturbation is discussed in Sect. 3.2: *Numerical perturbations - static gravitational cell mass.*

Summary for the survey of the subcritical core model sequence

At the end of the subcritical core mass model sequence survey we reiterate several points and draw the following conclusions:

1. the ‘nebula’ region is stable
2. models from the ‘protoplanet’ region either make transition to the ‘nebula’ region or collapse toward the ‘mature giant planet’ region

3. the ‘mature giant planet’ region is (meta) stable
4. our results for stable and meta-stable envelopes are in a very good agreement with the stability predictions based on linear stability study by Schönke (2005)
5. additionally to linear instability, we see indications for non-linear instabilities governing the evolution of the collapsing models
6. for all of the observed transitions, the gas density of the initial state was higher than the gas density at the core surface of the end state. This gives us the strong indication that the ‘protoplanet’ region can not be reached within a framework of the gradual core growth (which leads to monotonically increasing ρ_{cs}).
7. we would expect that a strong perturbation, such as the coalescence of two cores of similar sizes, during a collision of two planetary embryos, could throw the model from a ‘nebula’ region into a ‘mature giant planet’ region, or in a ‘fast collapse’ part of the ‘protoplanet’ region. This could potentially open a way for a gas giant to form relatively quickly from a small (i.e. subcritical) core. But the exact nature, strength, or very existence of the perturbation needed for that kind of transition will at present remain unknown.

With this we conclude the initial inspection of the subcritical models sequence. We can confirm that the static classification (Sect. 1.3.2) indeed applies to the dynamical properties of the models with medium core densities. This further strengthens our hopes that the medium core density models are a good representation of the models with the high (realistic) core density.

Generally, further analysis is needed, with a stronger analytic description of the dynamic phenomena. Thermodynamical formalism for a core-envelope model needs to be developed, to be able to strictly describe state transitions and lowest energy states.

Such analysis is unfortunately out of the time-frame of this project.

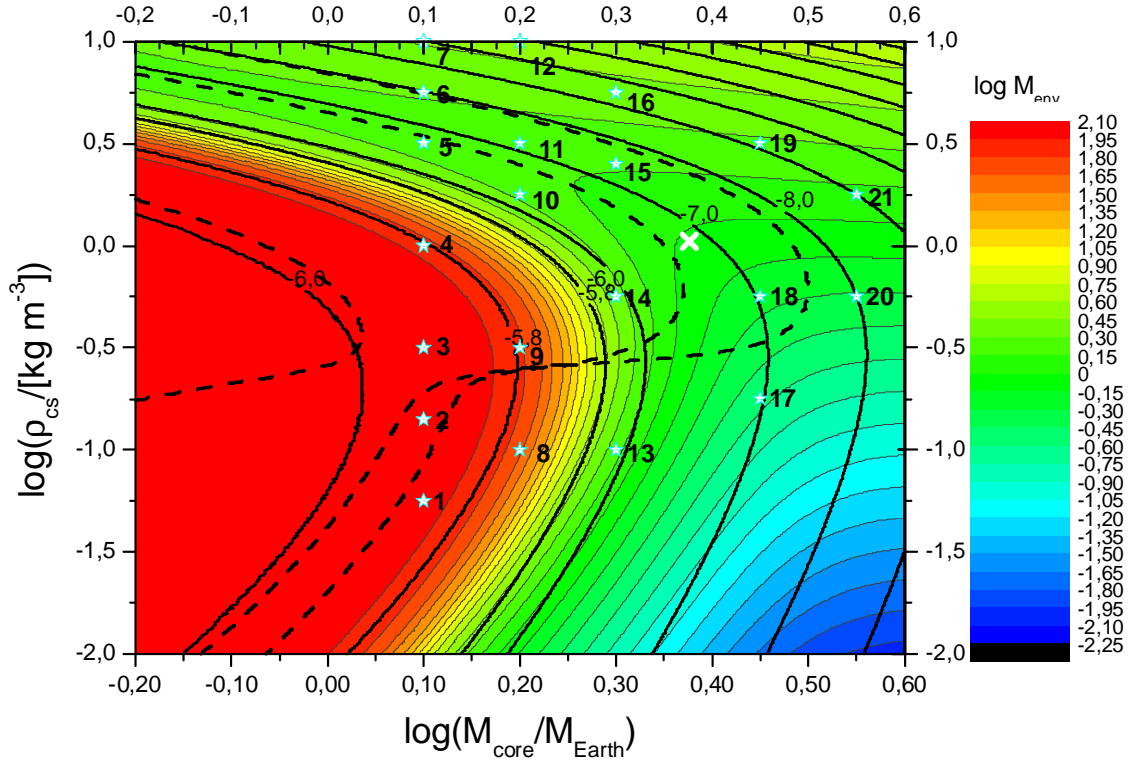


Figure 3.23: Nebula density contour plot of the region around the critical core mass of the solution manifold for $\rho_{\text{core}} = 1 \text{ kg m}^{-3}$, $a = 5.2 \text{ AU}$, and $T = 123 \text{ K}$. Color contours show envelope mass according to the legend. Thick dashed lines mark the region of linear stability, each line standing for different outer boundary stability condition; cf. Schönke (2005). Solid black lines are contours for different nebula densities, and labels represent logarithm of the nebula density in SI units. White stars mark the position of models chosen for dynamical calculations. White cross is the position of the global critical core mass, according to conditions stated in Eq. 1.3.7. Raw manifold data for this figure courtesy of J. Schönke, AIU Jena.

Region around the critical core

In the previous section we performed a non-linear analysis of the typical subcritical core. We now put focus on the region around the critical core mass, to get a better understanding of the role of the critical core mass in the early evolution of the planet.

Schönke (2005) performed a linear analysis for the same manifold region, and he found a region of the linear instability extending around a critical core mass (c.f. Fig. 3.23, thick dashed line encompassing a white cross). We have chosen our models, shown as stars on Fig. 3.23, to be able to compare linear and non-linear stability properties of the models

around the critical core mass. According to the classification of the static, high core density models (c.f. Sect. 1.3.2) all four envelope regions converge around the critical core mass. We have placed several models in each of those four regions. Thus we hope that we will investigate all dynamical phenomena relevant for this region.

Our models range from massive to low envelope mass, but all of them are quite compact (c.f. Fig. 3.24).

We present the results of the non-linear dynamical analysis of the critical core mass region on Figs. 3.25 and 3.26. As it turns out, all of the models we investigate follow the same dynamical behavior - they are all unstable against collapse. Subcritical, just critical, supercritical, self-gravitating or not, all of the models went into collapse after initial perturbation. This is in sharp contrast to the previous survey (subcritical core mass model sequence), where we observed several different types of dynamics at work.

Even models which are supposed to be linearly stable, according to Schönke (2005), go into collapse. The same is true for models which have an alternative state available (same nebula density, but lower gas density at the core surface). Such models in previous survey would usually make a transition to the alternative state with the lower ρ_{cs} , and would collapse only for a special subset of models (see Sect.3.4.2: *Subcritical core mass model sequence*).

Rebound of the effective core during collapse

When massive stars use up their fuel, they go into a collapse from a white dwarf to a neutron star (or to a black hole, for extremely massive stars) (see e.g. Kippenhahn and Weigert (1990), Sect. 34). During collapse, the core remnant is somewhat over-compressed by inertia beyond its equilibrium state, and it rebounds, sending shock-waves into the infalling matter above. If the shock expands to optically thin parts of the envelope, the core explodes and the object becomes a ‘supernova’.

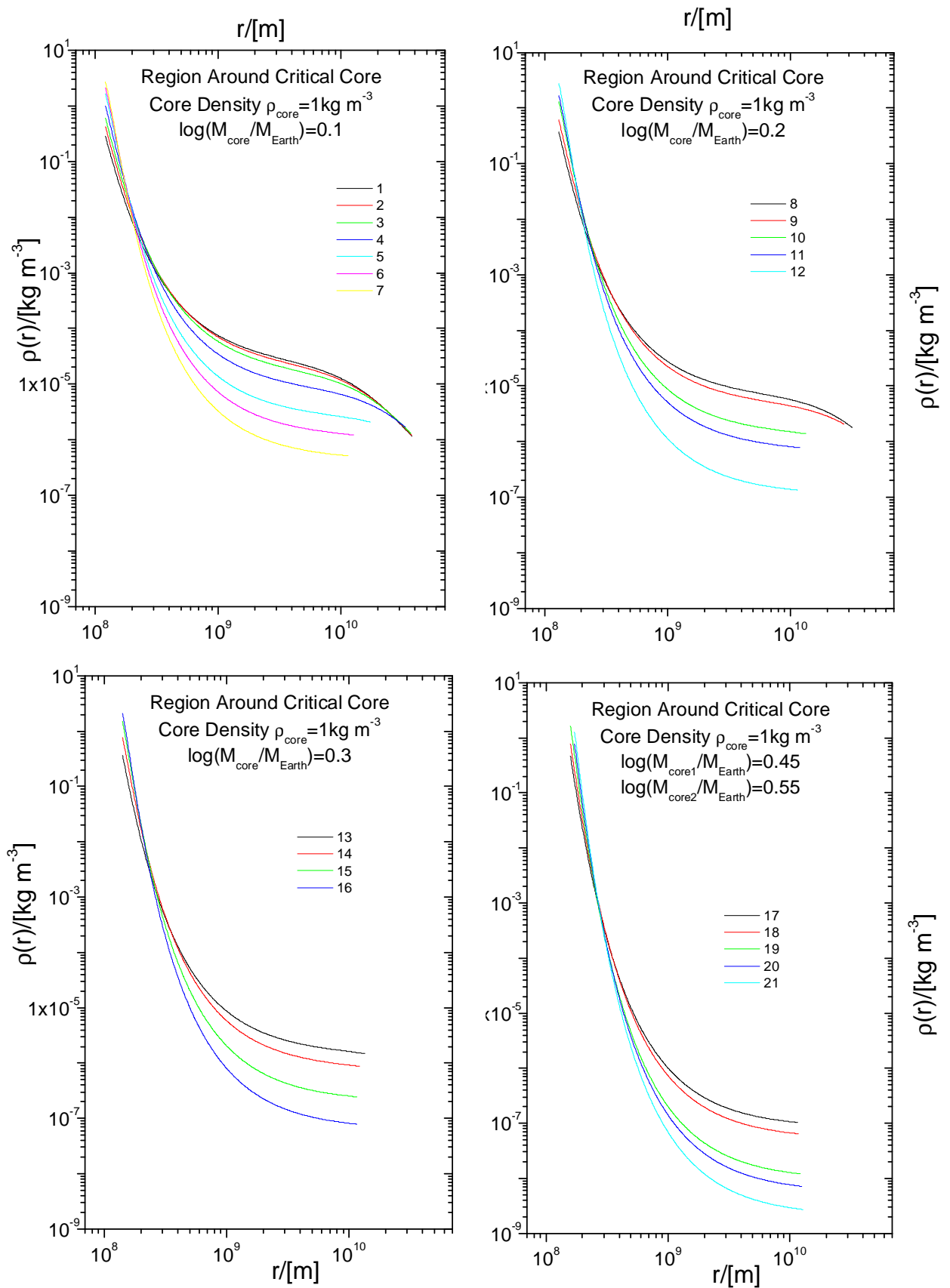


Figure 3.24: Envelope density profiles for different models shown on Fig. 3.23. Color coded lines are just for model distinction.

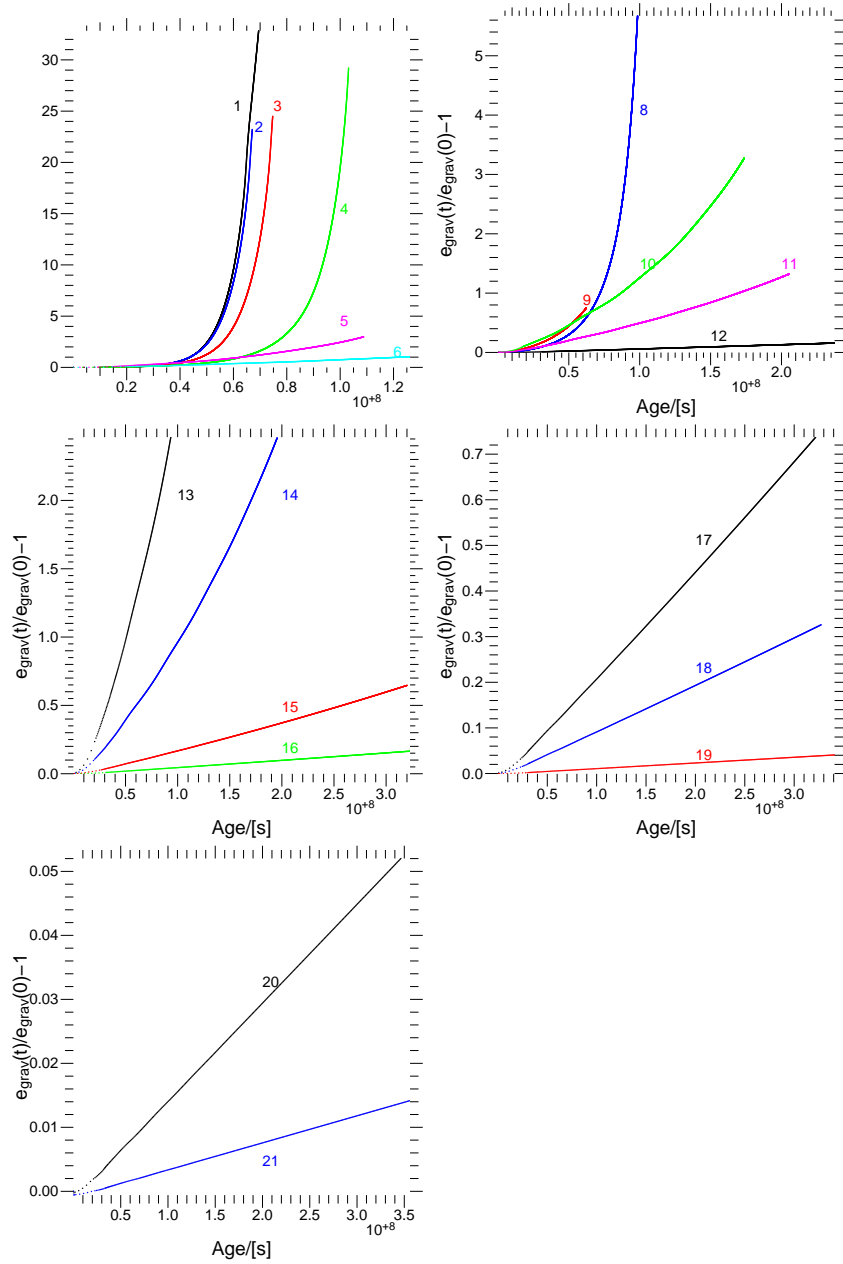


Figure 3.25: Time evolution of the relative change of the envelope gravitational energy (c.f. Eq. 3.4.3) for models in the vicinity of the critical core mass. Every 50th time level is plotted, and is represented with a dot; dots are not connected. Numbers correspond to models from Fig. 3.23. All models evolve into collapse. Difference between curves and straight lines is in the momentum that arrives onto the effective core; ‘fast’ collapse models (e.g. models 1 to 4) deploy a significant amount of the material onto the effective core, forcing the effective core to smaller radii and compressing it to higher densities, both of which contribute to the gravitational energy; ‘slow’ collapse models (e.g. models 17 to 19) do not transfer enough of momentum to force the effective core to the smaller radii, thus they increase gravitational energy only through the increase in the envelope mass. See text for further discussion.

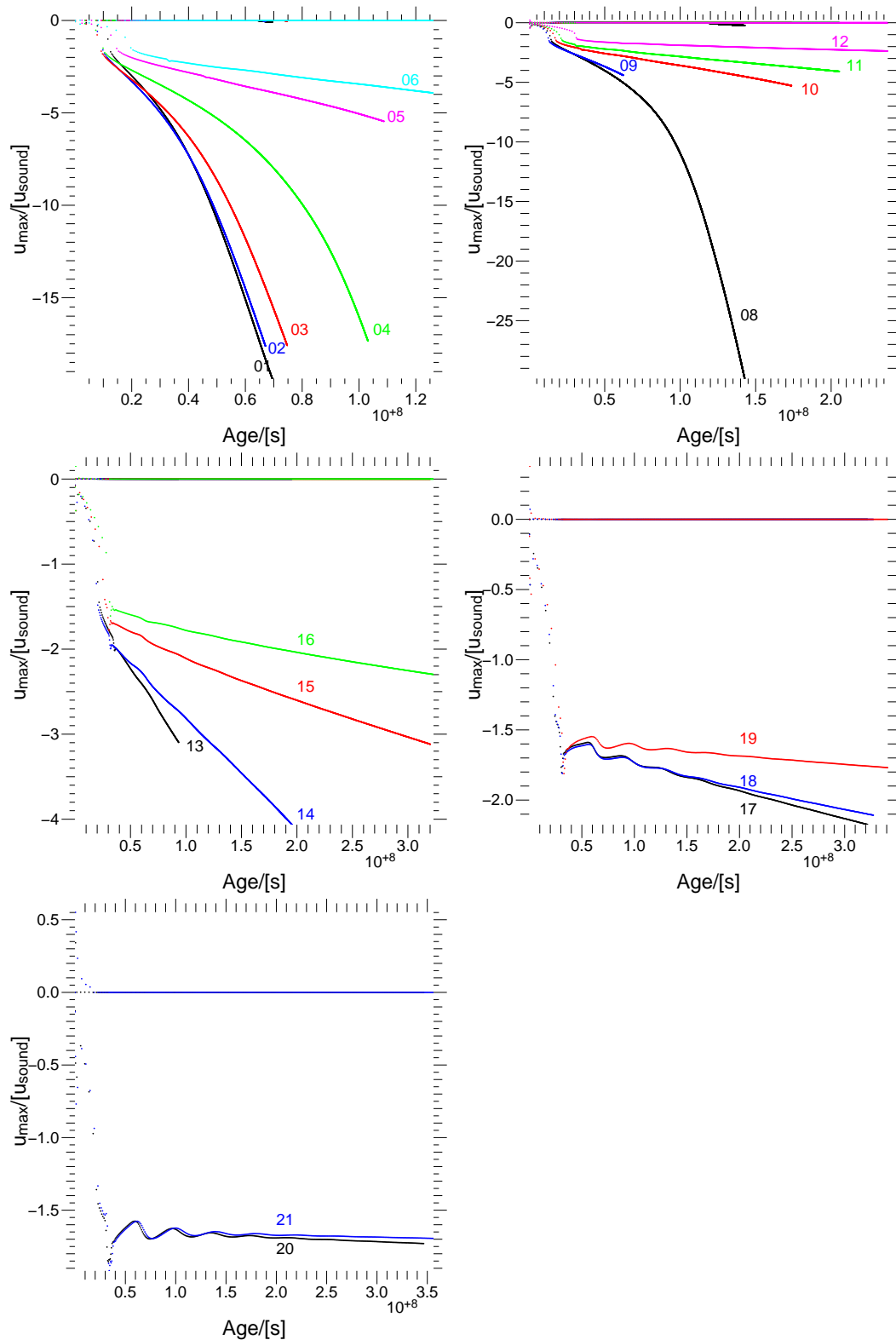


Figure 3.26: Time evolution of the extremal (largest positive and negative) envelope gas velocities. Every 50th time level is plotted. Calculations begin with slightly perturbed hydrostatic profiles. All models evolve into collapse. See caption of Fig. 3.25 and text for discussion on the difference between 'slow' and 'fast' collapse models.

We have noticed that the collapsing envelope of the model planet has a feature reminiscent of the core collapse for massive stars - a core rebound. In this case, it is not the real, incompressible model's core which rebounds, but the compact inner envelope part - the effective core.

When the envelope goes into a collapse, in some cases the initial mass infall onto the effective core can transfer a significant amount of momentum. The equation of state is for an ideal gas, and as such is not very 'stiff', yet it is stiffer than degenerate electron gas. Therefore the effective core could be over-compressed, and excited into a (damped) oscillation. Figure 3.27 shows several different examples of this phenomena.

In case of a massive envelope, collapsing with the strong initial 'kick', effective radius will be excited into an oscillation, and on top of that the continuous flux of incoming material will additionally reduce the radius of the effective core (left plot of Fig. 3.27).

If, on the other hand, the envelope is compact, but has no significant amounts of material to supply through collapse beyond the initial 'kick', the effective core will be excited into a damped oscillation, but its radius will not be further reduced (e.g. model 21 on Fig. 3.27).

We noticed a rebound of the effective core for both surveys of models with the medium core density.

An additional feature, not known from stellar astrophysics, is a non-linear 'crunch' just before the rebound. We noticed this only for just-critical and (weakly) supercritical cores. It is thus possible that this 'crunch' is connected to the critical core mass, possibly as a non-linear oscillation of the inner part of the envelope. Two examples can be seen on right plot of Fig. 3.27, for models 14 (just critical) and 21 (weakly supercritical), at $t \approx 3 \cdot 10^7$ s, i.e. $t \approx 1a$.

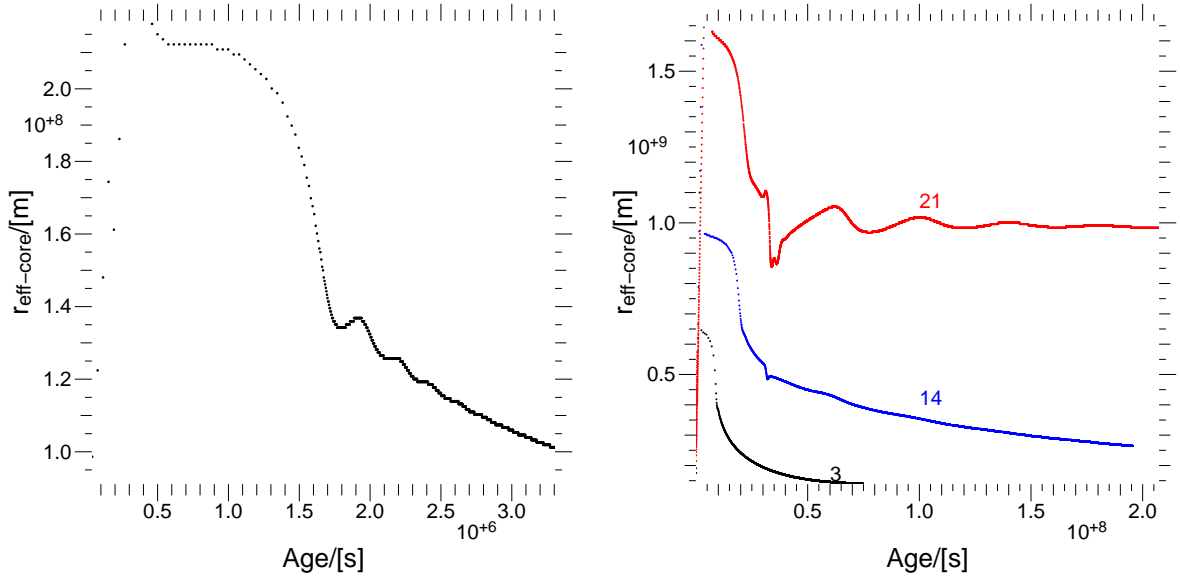


Figure 3.27: Effective core rebound: Time evolution of the radius of the effective core for a typical subcritical collapsing model (left figure, ‘fast’ collapse of model 25 from Fig. 3.17), and for models around the critical core mass (right figure): a subcritical core - model 3 (black, ‘fast’ collapse), a just-critical core - model 14 (blue, ‘fast’ collapse), a supercritical core - model 21 (red, ‘slow’ collapse). Models from the figure on the right are shown on the Fig. 3.23. Every 50th time level is plotted. See text for discussion.

Conclusions for the survey of the region around critical core

At the end of the survey of the region around the critical core mass we reiterate several points and draw the following conclusions:

1. *all of the states around the critical core mass are unstable against collapse.*
2. collapse can proceed either by keeping the radius of the effective core constant in time, or it can reduce the effective core radius essentially all the way to the real core radius, completely destroying the initial envelope structure in the process
3. in some cases the collapse can excite a damped oscillation of the effective core - an effective core rebound. Similar feature has been found for the collapse of massive stars (c.f. e.g. Kippenhahn and Weigert (1990)).
4. instability against collapse of the (weakly) subcritical models, found within this survey (models 1 to 12 from Fig. 3.23), hints that *a protoplanet can start the dynamical*

part of its early evolution even with a subcritical core.

5. the results of our analysis, for the region around the critical core mass, are not in agreement with the prediction of linear stability analysis by Schönke (2005). This, along with a non-linear ‘crunch’ during the rebound of the effective core, indicate that the critical core mass is associated with at least one kind of (strong) non-linear instability.
6. the effect of this instability is obviously greatly reduced, if not completely removed, in case of a subcritical core mass model (e.g. the subcritical core which we have chosen in our previous survey). Just how far exactly this (critical) core instability reaches will presently remain unknown.

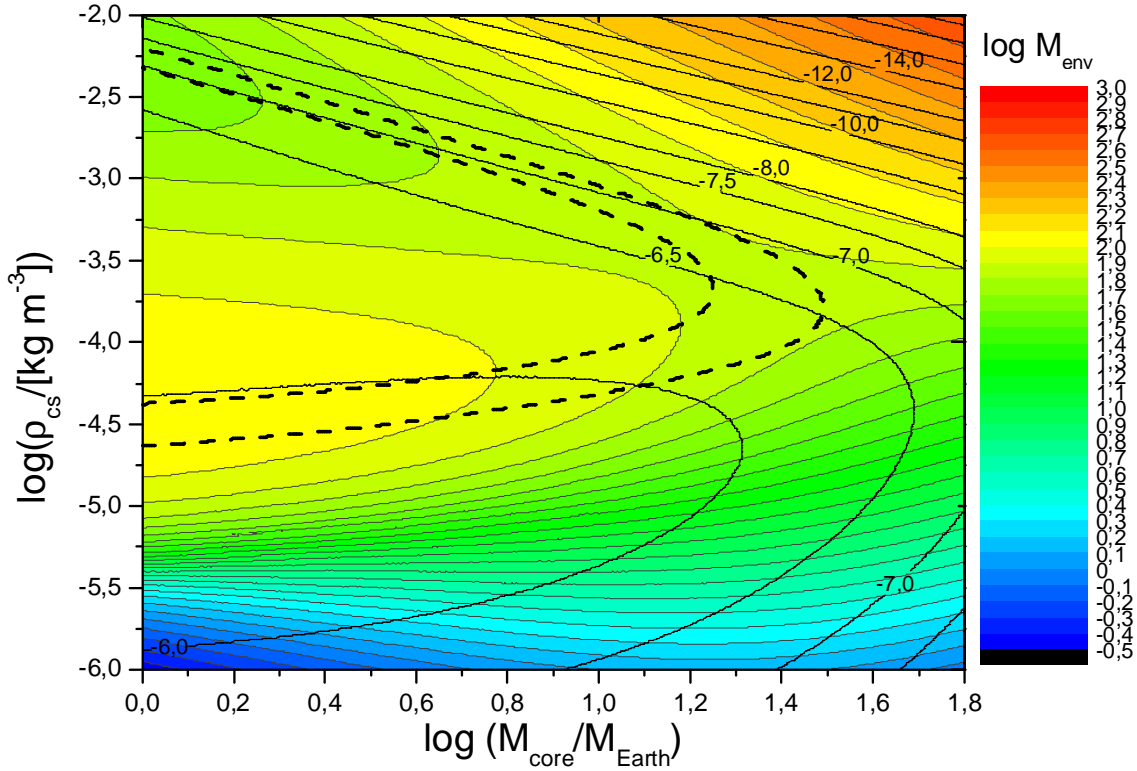


Figure 3.28: Nebula density contour plot of the solution manifold for $\rho_{\text{core}} = 1.5 \cdot 10^{-4} \text{ kg m}^{-3}$, $a = 5.2 \text{ AU}$, and $T = 123 \text{ K}$. Color contours show the logarithm of the envelope mass in M_{\oplus} according to the legend. Thick dashed lines mark the region of linear stability, each line standing for different outer boundary stability condition for the linear dynamics; cf. Schönke (2005). Stability for a given boundary condition is to the right (higher M_{core}) of the respective dashed line. Solid black lines are contours for different nebula densities, and labels represent logarithm of the nebula density in SI units. Raw manifold data for this figure courtesy of J. Schönke, AIU Jena.

3.4.3 Low core density

The core's gravitational potential needed to be 'softened' for the numerical convenience. The 'softening' was introduced by reducing the core density (see discussion in Sect. 3.1). The lowest core density we used was $\rho_{\text{core}} = 1.5 \cdot 10^{-4} \text{ kg m}^{-3} = 50\rho_{\text{Hill}}$, where Hill density is set through the definition of the Hill Sphere (c.f. Eq. 1.2.1). For such a core density $r_{\text{core}}/r_{\text{Hill}} \approx 0.399$, while a $\rho_{\text{core}} = 5500 \text{ kg m}^{-3}$ gives $r_{\text{core}}/r_{\text{Hill}} \approx 0.0012$. Although 'core' with $\rho_{\text{core}} = 1.5 \cdot 10^{-4} \text{ kg m}^{-3}$ is roughly six orders of magnitude less dense than rock/ice and is arguably closer to a typical nebula density than to a typical condensible

element structure, it was interesting to examine this case (see Fig. 3.28) for two reasons. Firstly, such a small core density enabled fast calculation of the envelope dynamics, and many models could have been covered for many (tens, even hundreds of) sound crossing times. Secondly, such a core density closely corresponds to the effective core density of the ‘gravitationally smoothed’ models in the state-of-the-art disk-planet-interaction type calculations, (e.g. Kley, 1999; D’Angelo et al., 2002, 2003; Nelson and Papaloizou, 2004). Therefore, it was valuable to learn to what degree the dynamics of such a system corresponds to the dynamics of the system with a much deeper potential (higher core density). For further discussion of the consequences of the results for such core densities, see Sect. 3.5.1.

A separate issue arises upon comparing the dependance of M_{env} and ρ_{neb} vs ρ_{cs} , Fig. 3.28 with Fig. 3.16, or Fig. 3.29 with Figs. 3.17 and/or 3.30. For model planets with middle to realistic core densities (i.e. 1 to 10^3 kg m^{-3}) distinct manifold regions, as determined by envelope mass properties, are closely overlapping with manifold regions derived from envelope’s outer density properties (c.f. Sect. 1.3.2 for a description of the manifold regions). The same is *not* true for models with low core densities (e.g. $\rho_{\text{core}} \approx 10^{-4} \text{ kg m}^{-3}$). This can easily be seen on Fig. 3.29, where the equivalent to the ‘mature gas giant’ region (compact self-gravitating envelopes) starts at different ρ_{cs} , gas densities at the core surface, for the envelope mass and for the nebula density. That is not the case for high core density models, c.f. Fig. 3.30, where the ‘mature giant planet’ region starts at the same ρ_{cs} for both the envelope mass and the nebula density. From Fig. 3.29, we can see that ρ_{out} would put the ‘mature gas giant’ region at $\rho_{\text{cs}} > 0.1$, whereas M_{env} would put it at $\rho_{\text{cs}} > 0.001$. Upon inspecting Fig. 3.28, we can come to a similar conclusion about the ‘location’ of the (global) critical core mass; one position ($M_{\text{core}}, \rho_{\text{cs}}$) would be chosen according to nebula density properties, entirely different position would be derived from the envelope mass properties, and yet another from linear instability lines.

This discrepancy questions the uniqueness and validity of the classification based upon

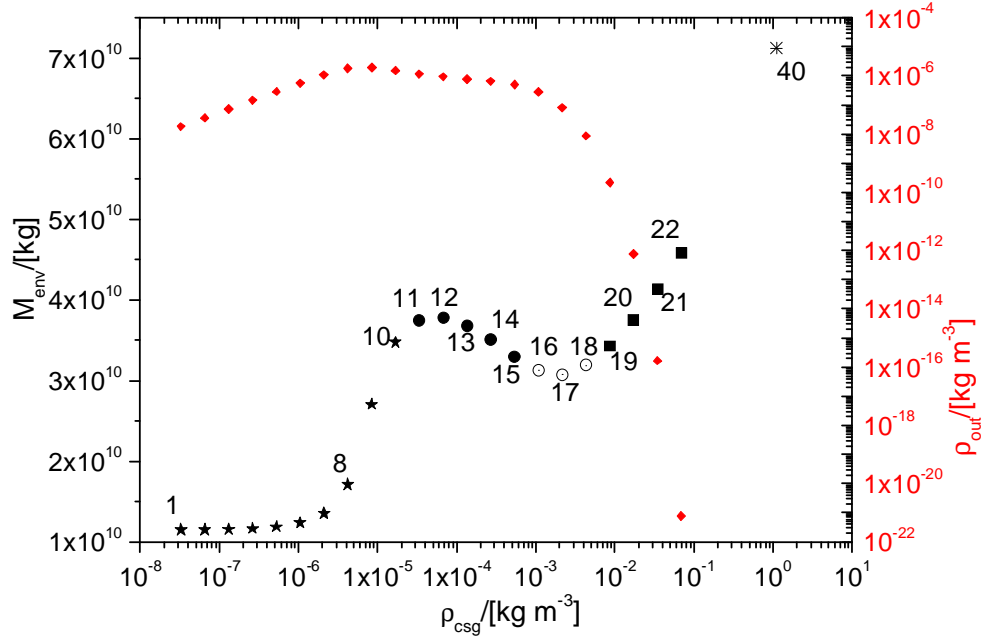


Figure 3.29: Manifold cut for a typical subcritical core ($\log M_{\text{core}}/M_{\oplus} = 0.5$), with $\rho_{\text{core}} = 1.5 \cdot 10^{-4} \text{ kg m}^{-3} = 50\rho_{\text{Hill}}$ core density, where Hill density is set through the definition of the Hill Sphere (c.f. Eq. 1.2.1). Numbers identify different models, shown in Figs. 3.31 and 3.32. Stars represent models from ‘nebula’ region, black circles and white circles are ‘protoplanet’ region models, while black squares are ‘mature gas giants’ region models (according to the classification of static high core density models, from Sect. 1.3.2).

the static properties of the high core density models. The ambiguity is confirmed when applied to the dynamical behavior of low core density models.

It also stopped us from performing dynamical analysis around the critical core mass. The critical core mass is so unconstrained that the model grid needed to cover the required area is just too large, in the time-frame presently available. A smaller grid density (than the grid density for the medium core density models) would not make sense, because some of the dynamical properties could easily be missed. Hence it would be very difficult to state any kind of reliable conclusions about the dynamical properties of that part of the solution manifold.

Because of the above stated reasons, we decided not to perform the analysis of the region around the critical core mass. The only analysis we will perform for the low density core models will be the analysis of the typical subcritical core model sequence.

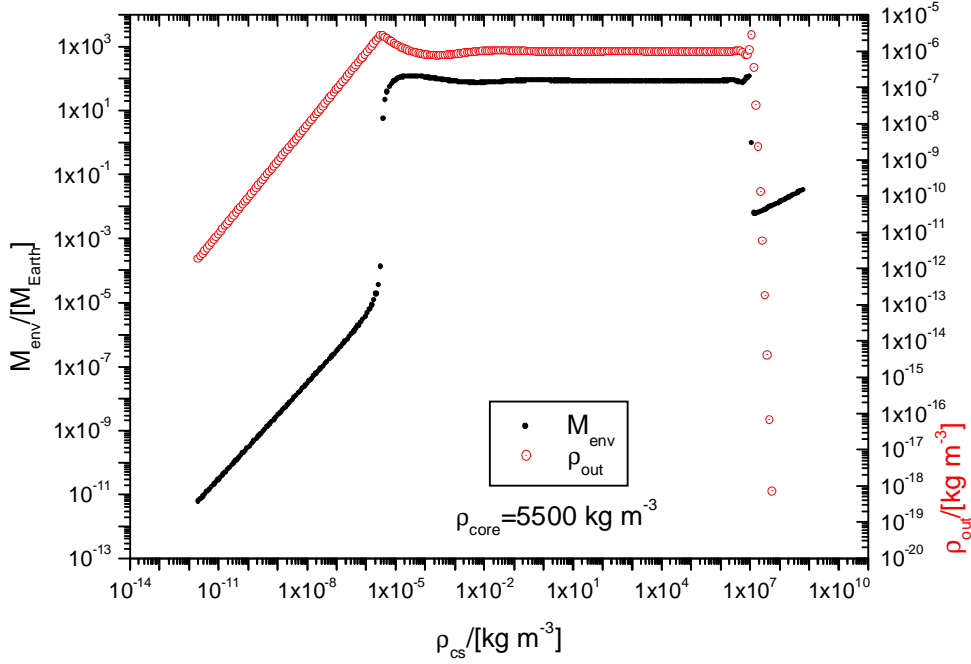


Figure 3.30: Manifold cut for a typical subcritical core ($\log M_{\text{core}}/M_{\oplus} = -5$), with high (realistic) core density, $\rho_{\text{core}} = 5500 \text{ kg m}^{-3} = 3.7 \cdot 10^7 \rho_{\text{Hill}}$, where Hill density is set through the definition of the Hill Sphere (c.f. Eq. 1.2.1).

Subcritical core mass sequence

Figure 3.29 shows a sequence of models placed along an envelope mass manifold cut for a typical subcritical core. The corresponding radial profiles of individual models can be seen on Fig. 3.31. Those models were used as initial states for hydro-dynamical calculation, and their evolution was followed for one hundred sound crossing times.

Figure 3.32 shows a time evolution of the envelope's gravitational energy, as defined with Eq. 3.4.3, while Fig. 3.33 shows a time evolution of the extremal velocity values (largest positive and largest negative). For a brief discussion on a choice of the dynamical indicators, see Sect. 3.4.

As in the equivalent survey for the medium core density models, we will inspect the model sequence in the order of increasing gas density at the core surface, ρ_{cs} . The reader should keep in mind the discussion of the initial perturbation (c.f. Sect. 3.2: *Numerical perturbations - static gravitational cell mass*), i.e. that models with higher ρ_{cs} will initially be

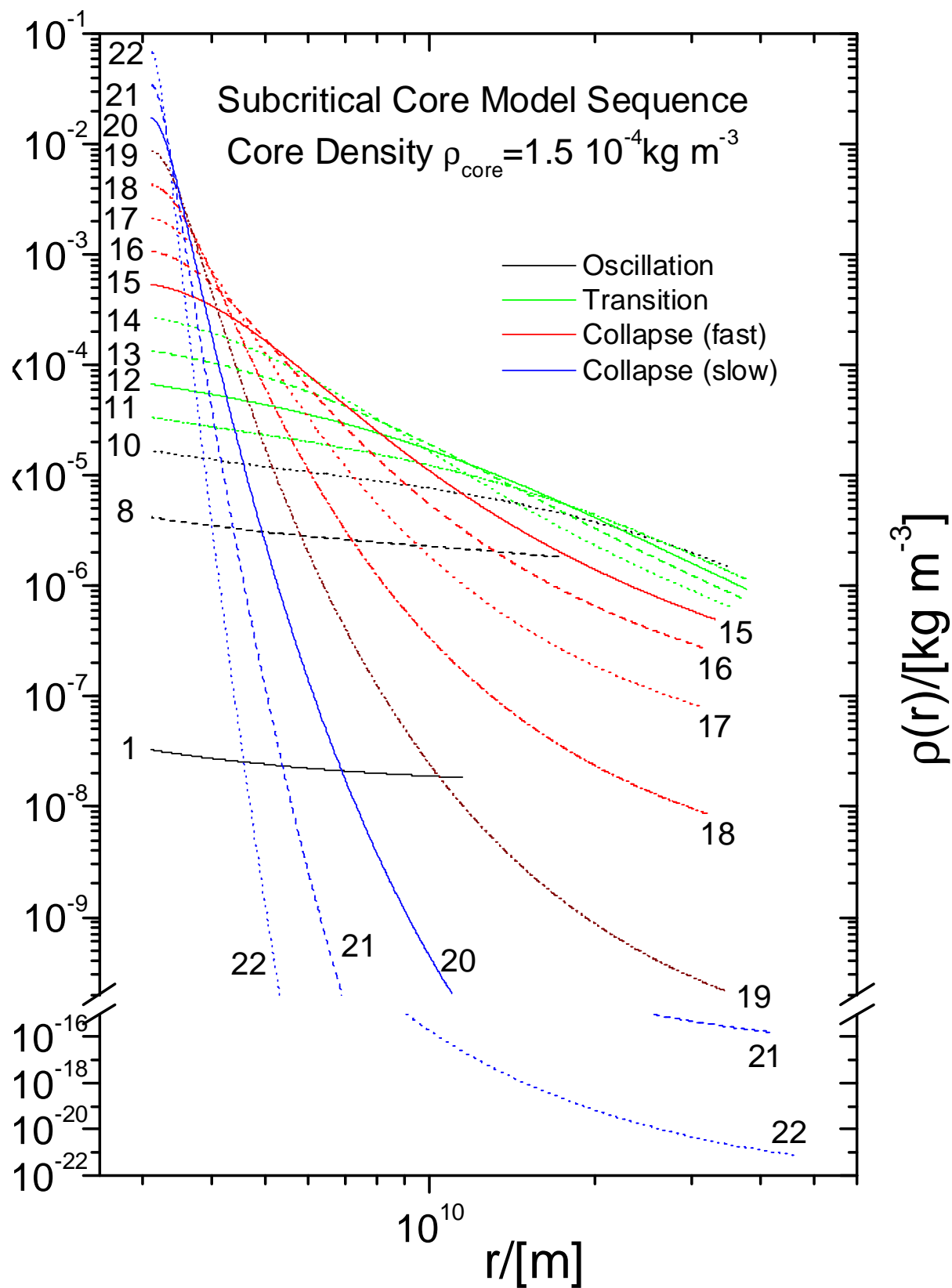


Figure 3.31: Envelope density profiles for different models shown on Fig. 3.29: black lines - stable, oscillating models; green lines - models undergo transition to the ‘nebula’ region; red lines - ‘fast’ collapsing models; blue lines - ‘slow’ collapsing models.

more perturbed.

Initially we inspect the models with the lowest ϱ_{cs} , the ‘nebula’ region models. Just as for the medium core density models, the stability of these models is well represented in the linear analysis of Schönke (2005). The models 1 to 10 from Fig. 3.29 are stable, and just *oscillate* around the initial equilibrium excited by the initial perturbation, as can be seen on Fig. 3.32.

The ‘protoplanet’ region follows, with massive envelope models, immersed into dense nebulae. As we mentioned already, the lower ϱ_{cs} boundary of the ‘protoplanet’ region agrees well with the linear instability line, i.e. we start noticing the dynamical *transition* of the initial models into the ‘nebula’ region equilibria, for the ϱ_{cs} which are within a factor two from linear stability analysis prediction for the first unstable model. The same was the case for the medium core density models. Figure 3.32 demonstrates that the transition into the ‘nebula’ region, followed with an oscillation excited by the transition, is a behavior characteristic for models 11 to 16 from Fig. 3.29.

We believe that the *transition*, from the lower ϱ_{cs} side of the ‘protoplanet’ region into the ‘nebula’ region, *is initiated by a linear instability*, because the region boundary agrees so well (within a factor of two) with the prediction of the linear instability analysis, and because the change of the behavior is gradual (as we go through the model sequence).

We now move to models with even larger ϱ_{cs} , models 16 to 19 from Fig. 3.29. From the same figure it is clear (especially upon comparison with the equivalent core mass manifold cut for the realistic core density models, Fig. 3.30) that, due to the low gradient, the ‘protoplanet-mature gas giant’ region boundary is not obvious for low core density models. Thus it is difficult to say with certainty to which region models 16 to 19 belong to. From comparison of the dynamical properties of these models (from Figs. 3.32 and 3.33)

with the dynamical properties of the equivalent medium core density models (e.g. models 25, 26, and 32 from Figs. 3.20 and 3.21), and noting the linear instability line for high ρ_{cs} (c.f. Fig. 3.28), we suggest that models 16 to 19 still belong to the ‘protoplanet’ region .

Just as it was the case for the medium core density models, the change is sharp, in the dynamical properties of the model sequence between the ‘transiting’ (models 11 to 16) and ‘collapsing’ (16 to 19) models of the ‘protoplanet’ region. This sharp change in the qualitative dynamics, along with the ‘fast’ collapse reminiscent of the ‘fast’ collapse around the critical core mass region (for the medium core density models), indicates that *the instability responsible for the ‘fast’ collapse of models 16 to 19 has a non-linear nature.*

For further details of the dynamics of the ‘fast’ collapsing models of the ‘protoplanets’ region we refer the reader to the equivalent section in the subcritical core mass model survey for the medium core density models.

Finally, we inspect models with the highest gas density at the core surface - models 20 to 22. For the medium core density models this would be the region of the (meta) stable ‘mature gas giant’ models. As we can see from Fig. 3.32, the gravitational energy of this group of models is constant in time. This reflects the fact that, although the effective core radius is slowly pushed back toward inner stratifications, the most massive part of the envelope stays virtually unchanged. In this context, this is the extreme example of the ‘slow’ collapse - the momentum flux of the collapsing outer stratifications is completely unable to significantly affect the massive inner parts. We followed the evolution of such ‘slow’ collapse up to shock (gas) velocities in excess of Mach 100, but were unable to locate any deviation from the dynamical characteristics described above.

We have performed the survey even further, for higher ρ_{cs} , hoping to find the (meta) stable equilibria. The model with the highest ρ_{cs} gas density at the core surface we

analyzed, model 40 from Fig. 3.29, exhibits the same dynamics as the ‘slow’ collapsing models (20 to 22). Further investigation of models with even higher ρ_{cs} was restricted because of lack of time, and, more importantly, because our numerical scheme started to break down.

Break-down of the code was most likely connected to outward shock propagation through the compact envelope with its exponentially decreasing density and the dynamic range of over 35 orders of magnitude. This type of environment is the only one our scheme had problems with.

Dynamical properties and the core density

Within this work we have performed a general study of the dynamical properties of a simple core-envelope system. One important aspect was to investigate how dynamical properties change with the change in the core density. This question is particularly interesting because artificially-low core density systems are used today in the state-of-the-art investigations of the (protoplanetary) disk-planet interaction. The low core density systems are used there for numerical convenience, and are generally considered to preserve the qualitative dynamical properties of the realistic core density systems.

We noticed qualitative differences in the evolution/stability of the envelopes for sub-critical cores with low core density (Sect. 3.4.3) and mid core density (Sect. 3.4.2).

Differences are not qualitative as long as the core is not supercritical, and as long as the gas density at the core surface is small, when compared to the core density. Thus, the ‘nebula’ region and the ‘nebula-protoplanet’ region boundary are qualitatively the same for both low and mid core density.

First, but major, qualitative difference in the dynamics occurs in the ‘protoplanet’ region, for equilibria with gas densities at core surface larger than those in ‘fast’ collapse model sequence (i.e. for models 20-22 from Fig. 3.29).

For medium core density survey, after ‘fast’ collapsing models in the ‘protoplanet’ region,

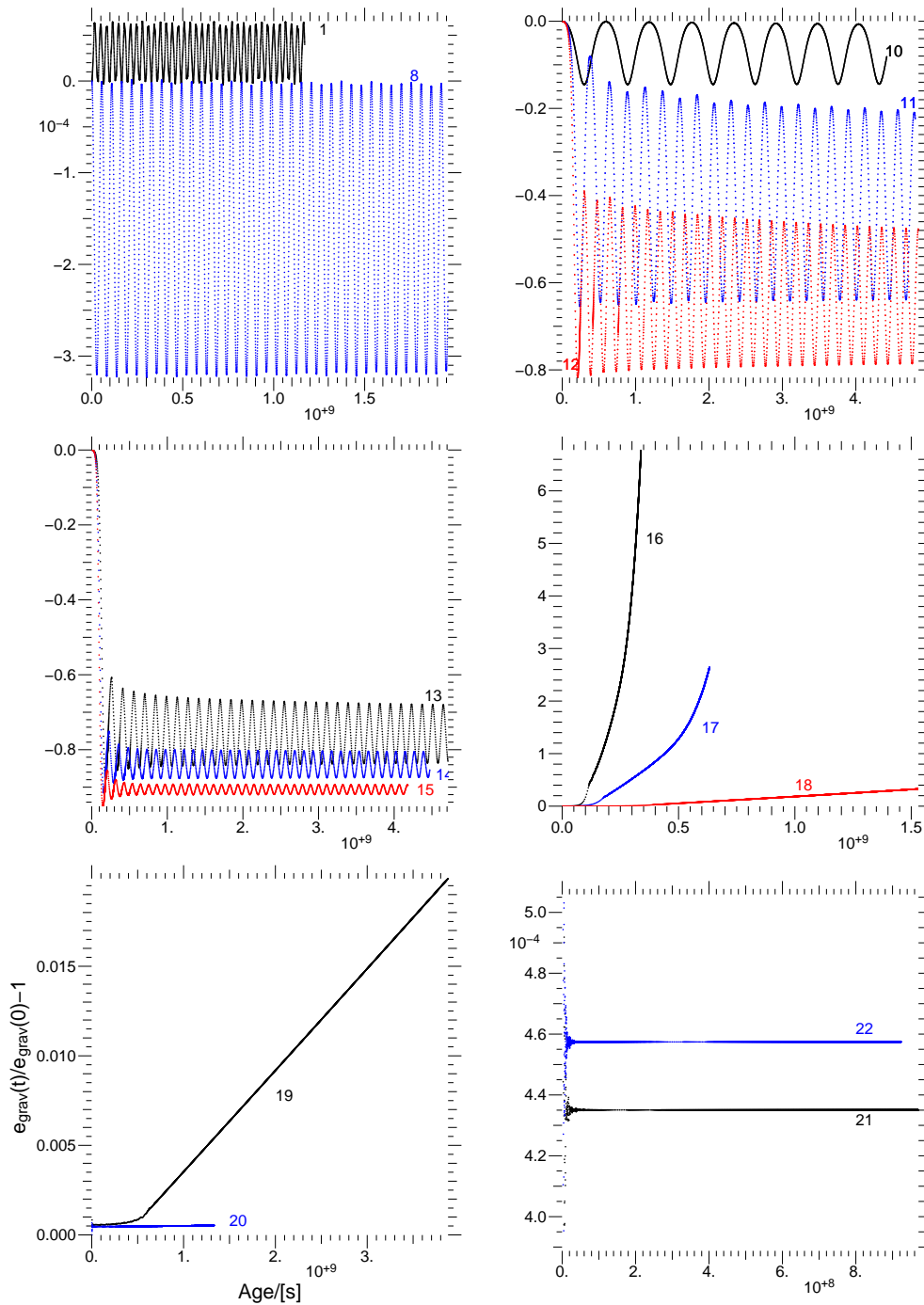


Figure 3.32: Time evolution (100 sound crossing times) of the envelope gravitational energy normalized to its initial value, c.f. Eq. 3.4.3. Every 500th time level is plotted, and is represented with a dot; dots are not connected. Numbers correspond to models from Figs. 3.29 and 3.31. Models 1 to 10 show an oscillation around the initial equilibrium; models 11 to 15 make a transition to an equilibrium (with a lower core mass than the initial equilibrium) and then oscillate; models 16 to 19 go into a fast collapse, quickly reducing their effective core (quickly relative to the sound-crossing time scale); models 20 to 22 go into a slow collapse, where the dilute outer part collapses onto the (essentially) fixed effective core. See text for discussion.

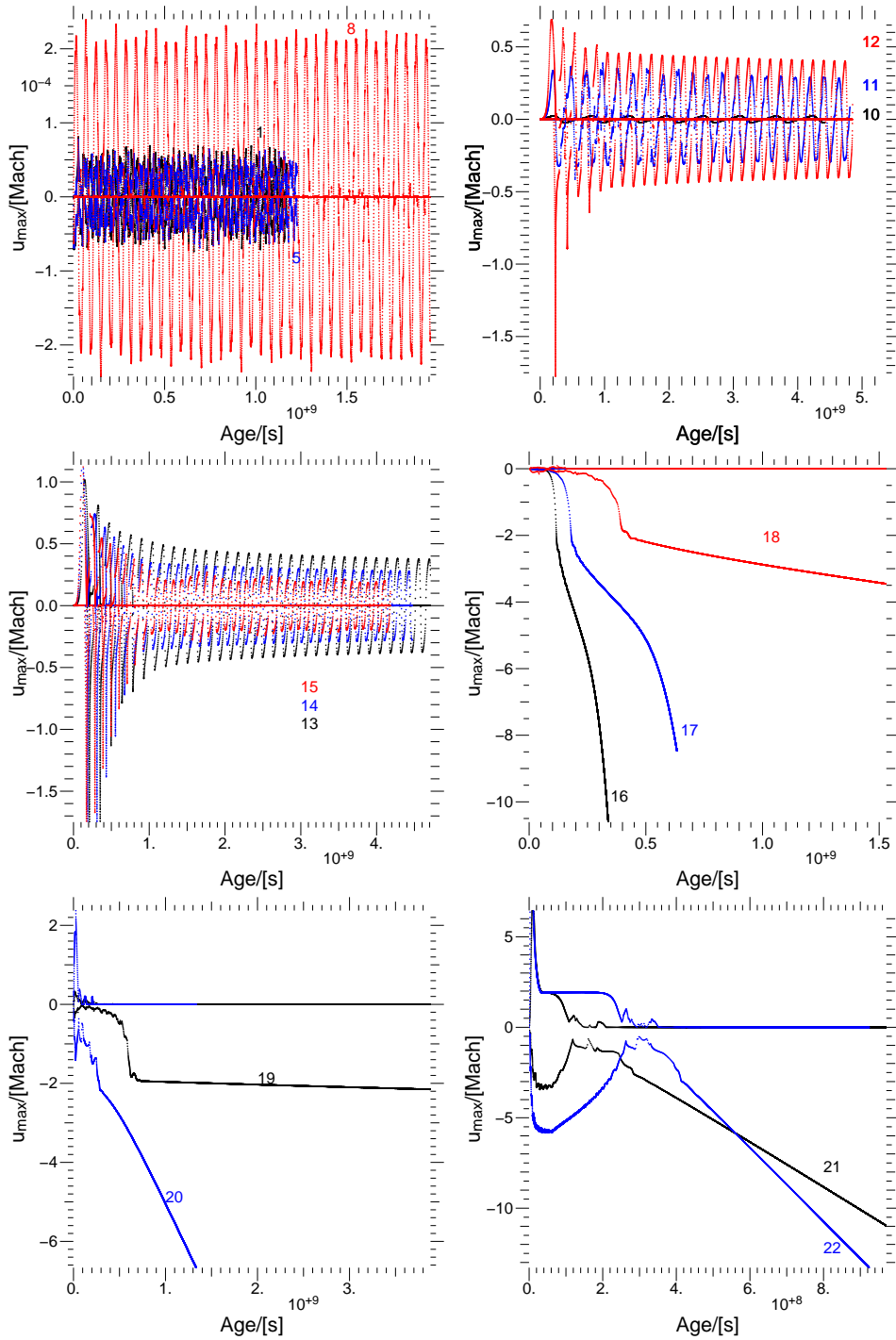


Figure 3.33: Time evolution of the extremal (largest positive and negative) envelope gas velocities. Every 500th time level is plotted, and is represented with a dot; dots are not connected. Numbers correspond to models from Figs. 3.29 and 3.31. Models 1 to 10 show an oscillation around the initial equilibrium; models 11 to 15 make a transition to an equilibrium (with a lower core mass than the initial equilibrium) and then oscillate; models 16 to 19 go into a fast collapse, quickly reducing their effective core (quickly relative to the sound-crossing time scale); models 20 to 22 go into a slow collapse, where the dilute outer part collapses onto the (essentially) fixed effective core. See text for discussion.

a sequence of models would follow which have their initial structures ripped apart by the instability triggered by the initial perturbation; after the envelope destruction, those models would undergo transition to the ‘nebula’ regime. In contrast, for low core density models, the sequence is continued with extreme cases of ‘slow’ collapsing models, such as models 20 to 22. The high ρ_{cs} ‘transiting’ subregion of the ‘protoplanet’ region could not be found and likely is small or simply non-existent.

Equilibria with even higher ρ_{cs} (e.g. model 40 from Fig. 3.29), exhibit the same dynamics as the ‘slow’ collapsing models (20 to 22). Thus, we were also been unable to find the meta-stable ‘mature gas giant’ region. This means that *compact equilibria are unstable against collapse, for core-envelope systems with the low core density.*

Such instability is in the sharp contrast to a (meta) stable ‘mature gas giant’ region, for core-envelope systems with the medium core density.

We continue by comparing the properties of a compact density profile for low and medium core density systems. This comparison reveals the advantages of choosing extremal velocity over velocity at the outer boundary, as one of the dynamical indicators.

Differences in the dynamical properties of the low and mid core density systems are not easy to spot by inspecting the evolution of the gravitational envelope energy; the constant-density (outer) boundary condition, coupled with the very low nebula density (order of $10^{-21} \text{ kg m}^{-3}$), greatly limits the accretion of an already quite compact envelope (c.f. radial profile of model 22 on Fig. 3.31). Envelope of such a compact model will look steady (c.f. model 22 on Fig. 3.32 and model 31 on Fig. 3.20).

But, upon comparing the velocities at the outer envelope boundary for both cases (low and mid core density), we see (Fig. 3.34) that the difference in the envelope evolution is qualitative; low core density model (on the left) goes into collapse, while mid core density model (right), after initial perturbation, finds a stable solution (and pulsates around it). This could mean that the ‘protoplanet’-region-instability extends to lower nebula densities

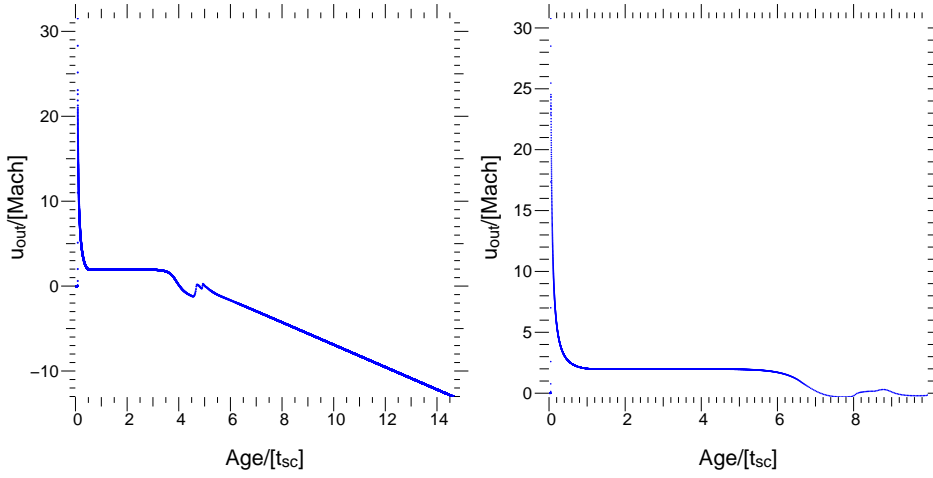


Figure 3.34: Comparison of the evolution of the velocity at the outer envelope boundary for two envelopes with similar nebula densities (order of 10^{-21} kg m $^{-3}$) and in a similar manifold region (lower ρ_{cs} of the ‘mature gas giant’ region), but with different core densities. Model on left figure (model 20) has a core density of $\rho_{core} = 1.5 \cdot 10^{-4}$ kg m $^{-3}$ (low core density), while the model on the right (model 31) has $\rho_{core} = 1$ kg m $^{-3}$ (medium core density). Model with the low core density goes into an envelope collapse, while the model with the mid core density settles around a meta-stable solution (c.f. Fig. 3.35). Time is in units of sound-crossing times, and velocity has dimension of Mach number.

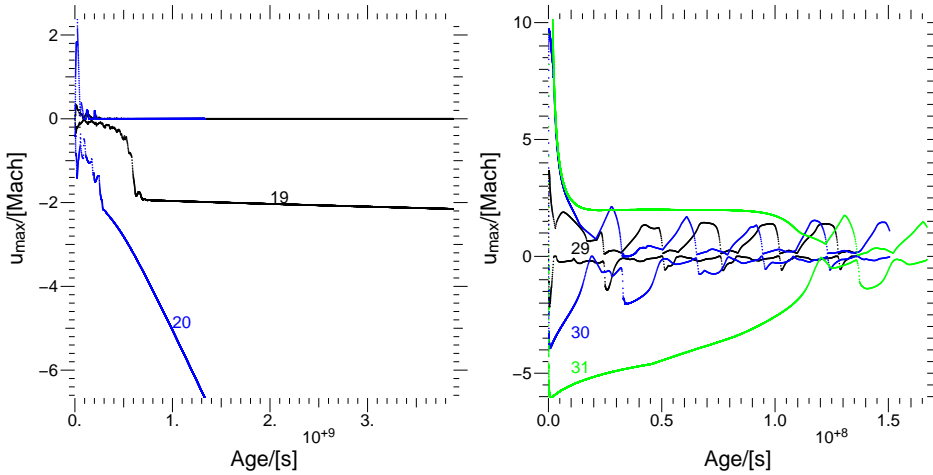


Figure 3.35: Comparison of the extremal velocity evolution for envelopes with similar nebula densities (order of 10^{-21} kg m $^{-3}$) and in a similar manifold region (lower ρ_{cs} of the ‘mature gas giant’ region), but with different core densities. Models on left figure have a core density of $\rho_{core} = 1.5 \cdot 10^{-4}$ kg m $^{-3}$ (low core density), while models on the right have $\rho_{core} = 1$ kg m $^{-3}$ (medium core density). Models with the low core density go into an envelope collapse, whilst models with the mid core density settle around a meta-stable solution.

for low density cores (even quite compact envelopes in near vacuum are unstable against collapse), as opposed to mid core density models, which are (meta) stable if placed in near-vacuum (in, e.g., 10^{-18} kg m⁻³).

Although in this case velocity at the outer boundary *did* indicate that one envelope is in collapse (model 22, left plot on Figs. 3.34 and 3.35), while the other (model 31, right plot on Figs. 3.34 and 3.35) is not, we are often limited to timescales shorter than the free-fall timescale. In such cases collapse does not have time to connect to the nebula, and from the outer boundary perspective envelope looks almost static. Therefore, additionally to normalized gravitational energy, we will use, as a stability indicator, the extremal (largest positive and negative) values of the envelope gas velocity. Extremal velocities will correctly indicate the state of the envelope, regardless of where the important dynamics is located.

Extremal velocity indicator shows that ‘more realistic’ (i.e. denser) cores indeed are able to stabilize against collapse. Thus, *cores with low effective densities do not show the stabilizing influence of realistic cores!*

Summary for the subcritical core model sequence

We conclude the subcritical core mass model sequence survey for low density cores with the recapitulation of the several important points:

1. the ‘nebula’ region is oscillating and stable
2. a linear instability operates in the ‘protoplanet’ region and drives the transition (from the ‘protoplanet’ to the ‘nebula’ region)
3. the border between the ‘fast’ and the ‘slow’ collapsing models is determined well by the linear instability line, c.f. Schönke (2005), and could serve as a dynamical counterpart to the static border between the ‘protoplanet’ and the ‘mature gas giant’ regions
4. a second ‘transiting’ subregion in the ‘protoplanet’ region does not exist (unlike for the medium core density models)
5. the entire ‘mature gas giant’ region appears to be unstable against the ‘slow’ collapse
6. *a subcritical core model sequence, for a low density core, is NOT dynamically equivalent to its medium core density counterpart.* Differences are qualitative.

Unlike for the high and medium core density models, the values of the *classical definition of the static critical core mass*, e.g. Wuchterl (1991a), and of the our newly proposed *global static critical core mass* (see Sect. 1.3.9) *are numerically incompatible*, i.e. $M_{\text{CCM}}^{\text{class}} \approx 8M_{\text{CCM}}^{\text{glob}}$. Thus a simple test could be performed in the future (dynamical stability of a core which is subcritical in the classical sense and supercritical in the new, global sense), to see which definition, if any of those, has more physical relevance.

3.5 Fluid-dynamics and disk-planet models

3.5.1 Future of the disk-planet calculations

We argue that the present-day locally isothermal disk-planet calculations are operating in a qualitatively different dynamical regime, than the one they are normally assumed to.

In Sect. 1.3.11 we showed that the introduction of the gravitational smoothing parameter in the disk-planet interaction type calculations (or alternative procedure with the same effect) is equivalent to drastically reducing the core density. *Manifold with reduced core density* (a problem with "soft" potential) *has a much higher critical core mass* (of the order of $100 M_{\oplus}$ already for the gravitational smoothing parameter $b \approx 0.1 r_{\text{Hill}}$!).

In the same Sect. we also showed that the transition between the envelope regions is smoother for smaller core densities.

Both of these facts will greatly affect the dynamics of the models in the disk-planet interaction type calculations. The dynamical properties of the system depend on the core density in number of instances (see summaries of the hydro-surveys for medium and low core density models). In other words, medium and low core density models operate in dynamical regimes which are mutually qualitatively different.

Therefore, present-day disk-planet calculations operate in a qualitatively different dynamical regime, from the one in which would be models with a correctly calculated gravitational potential.

We now give the outline of an idea that should greatly improve the resolution and the accuracy of the current hydrodynamical codes emulating a circumstellar protoplanetary nebula. The implementation should be relatively straightforward, and should not pose great difficulties for the hydro-codes written in a well-abstracted and structured manner. If the hydro-code is written in an object-oriented language, the matter of resolving the gravitational potential close to the core surface will be simplified even further.

Global 3D disk codes can greatly benefit in accuracy and computational speed by coupling to 1-(or 2- or 3-)D hydro code in a region between (proto)planet's core surface and a surface which is a (fraction to few) Hill radii away from the planet.

Close to the core surface spherical symmetry will be a good approximation, and the existing implicit hydro-codes will be able to include correct microphysics and will resolve the inner envelope stratifications much better than any existing global hydro-code.

Special attention will have to be paid to the consistent boundary conditions between the inner stratifications and the protoplanetary disk, as well as to the correct advection across this boundary.

3.5.2 Perturbations and the protoplanetary evolution

Additionally to the discussion of 3-(2-)D disk-planet interaction calculations, it can be argued that by putting a planet directly into an unperturbed nebula, instead of the gradual core growth, one type of solutions, with the higher ρ_{cs} , will be favored to the other, with the lower ρ_{cs} . At the same time, it is *not a priori clear* that the typical nebula perturbation will bring the planet to the state with higher gas density at the core surface.

This (type) of solution is more stable than the (type of) solution with the lower ρ_{cs} , but it is unclear under what circumstances during the evolution of the protoplanet the transition to the most stable equilibrium is made, and if it is made at all.

In future work, we could analyze the type and the strength of the perturbations which are able to produce the aforementioned transition, and the possible implications for the protoplanetary evolution.

Chapter 4

Summary and Discussion

Introduction

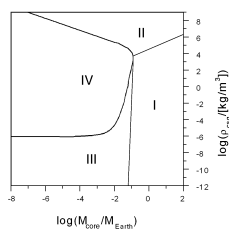
Our work is an investigation of the various aspects of the planetary formation theory, within the framework of the nucleated instability (for more on nucleated instability framework see e.g. Wuchterl et al., 2000).

Theory of the giant planet formation is to a large degree the question of how to accrete gas from otherwise stable nebula. That involves the issue of triggering the collapse or steady accretion. It has been assumed that the envelope accretion would follow once a critical mass of solids is assembled. The question of when this occurs has been tried to answer by constructing static models to the limit where no more static models would exist, and assumed accretion would occur (e.g. Ikoma et al., 2001; Bodenheimer et al., 2000). Dynamical studies have also been performed (e.g. Wuchterl, 1991a,b, 1993), as well as the disk-planet interaction investigations in 2D and 3D (e.g. Kley, 1999; D'Angelo et al., 2002, 2003; Nelson and Papaloizou, 2004). In all of these studies, both static and dynamic, 'the evolution' of *particular* planets is followed, but not much is known about the evolution of all possible protoplanets. Therefore, it is somewhat *difficult to frame the detailed solutions of previous investigations within a global perspective*.

We did the first survey of the dynamics of proto-planetary envelopes for arbitrary core and surrounding nebula. In our study we use a simple core-envelope model (c.f. Chapter 1) and aim for a complete hydro-dynamical classification of protoplanets.

Mapping out the solution space

During the early stages of the planetary evolution, typical dynamical processes most likely operate on the time-scales much smaller than the core-accretion timescale. Thus, most of its early days proto-planet will spend in a hydro-static equilibrium, or very close to it. It was therefore important to provide an idealized but complete road-map of all hydrostatic states, which we did in Chapter 1. Although our model is based on a fairly simple set of assumptions, after comparison with Broeg (2005), we are confident that *our model provides a qualitatively correct and complete overview of hydrostatic equilibria.*



We classify the protoplanets according to the general properties of their envelopes, within the complete set of core-envelope solutions (we propose to call it *solution manifold*). Depending if the protoplanetary envelopes are compact or quasi-homogenous, and self-gravitating or not, we have found four different envelope regions (c.f. Sect. 1.3.2): mature telluric planet (I), mature gas giant (II), nebula (III), proto-planet (IV). Borders between the regions are drawn using the morphological features of the envelope mass properties (c.f. Sect. 1.3.2).

We also develop a concept for the global static critical core mass, as a core of a proto-planet which connects all four qualitatively different envelope regions (c.f. Sect. 1.3.9).

As one of the byways of such global critical core mass, we provide a precise statement for the distinction between a planet and a minor planet, discussed in Chapter 2. In brief, a planet will have a core which is supercritical within the appropriate manifold. On the contrary, a minor planet will have a subcritical core. In Sect. 2.2 we show which of the larger bodies in the Sol System fulfill this planethood criterion.

The planethood criterion definition is general, and its validity extends beyond our isothermal model to any complete protoplanetary solution set, regardless of the complexity of the physical model used.

Protoplanetary dynamics

The next step in the understanding of the planetary equilibria was to find physically significant manifold solutions, i.e. to discriminate stable from unstable model-planets. We had the choice of either performing a linear or a non-linear stability analysis.

The linear analysis can distinguish a (linearly) stable from an unstable protoplanetary model, but it cannot be used to discover where the instability leads to, and even more so for an intrinsically non-linear system. Additionally, the linear stability analysis is limited only to the small envelope perturbations. As we have learned from our own planetary system, planet formation involves ‘large perturbations’, i.e. giant impacts (e.g. see the rotational axis of Uranus, or the Earth-Moon system, or Mars’ Schiaparelli crater-Valles Marineris canyon system, etc).

Therefore we decided to perform a non-linear stability analysis - we use the static profiles from a solution manifold as the initial states for a hydrodynamical code.

We use an explicit hydrodynamic code (c.f. Sect. 3.2), which was possible to build and test within a given time-frame, and whose performance (correct to 10^{-3} level) was good enough for the required problem (c.f. Sect. 3.3). The nature of our survey requires investigation of more than a hundred different protoplanetary models, and typically follows the evolution of every model for about ten to hundred sound-crossing times. These requirements would not be possible to fulfill for the models with a realistic core density of solids (i.e. $\rho_{\text{core}} \approx 10^3 \text{ kg m}^{-3}$), because such a core density imposes a prohibitively small time-step size in our explicit scheme¹. The compromise solution is to reduce the core density, but only to the point for which we can be reasonably certain that our dynamical analysis is still qualitatively correct. Through a comparison of linear stability properties for manifolds with different core densities (c.f. Schönke, 2005), we have chosen for our models a core density of $\rho_{\text{core}} = 1 \text{ kg m}^{-3}$.

¹time-step is determined, among other criteria, by the grid-cell size through the CFL condition; see Sect. 3.2

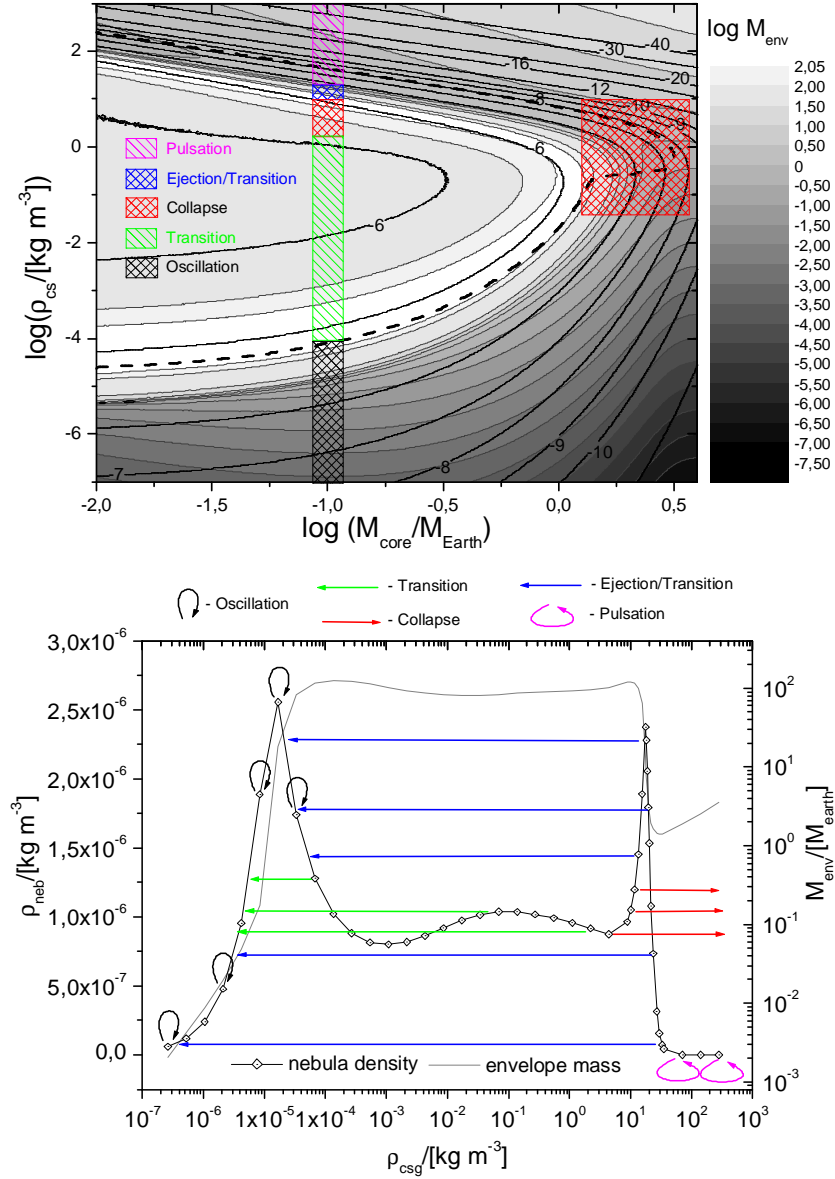


Figure 4.1: **Protoplanetary dynamics** *Top figure:* Dynamical characteristics of the solution manifold, with model parameters (M_{core} , ρ_{cs}) and for a core density of $\rho_{\text{core}} = 1\text{ kg m}^{-3}$, $a = 5.2\text{ AU}$, and $T = 123\text{ K}$. Shades of grey show the logarithm of the envelope mass in M_{\oplus} according to the legend. Thick dashed lines mark the region of linear stability, with stable solutions to the right of the curve, c.f. Schönke (2005). Solid black lines are contours for different nebula densities, and labels represent logarithm of the nebula density in SI units. Colored boxes show dynamical characteristics according to the legend. The critical core mass is located roughly in the middle of the large red box on the right side. *Bottom figure:* Manifold cut for a typical subcritical core ($\log(M_{\text{core}}/M_{\oplus}) = -1$, with $\rho_{\text{core}} = 1\text{ kg m}^{-3}$ core density). Arrows indicate initial and end states for the different dynamical regions, according to the legend. Typical subcritical core has five dynamical regions with different characteristic behavior: *oscillation* (stable), *transition*, *collapse*, *ejection+transition*, and *pulsation* (meta-stable). See text for details.

Although the non-linear analysis uncovered a whole zoo of evolutionary possibilities, all of them fitted into one or more of the five basic modes of dynamical behavior: *oscillation*, *pulsation*, *transition*, *ejection*, and *collapse* (c.f. Fig. 4.1). As the nomenclature suggests, some of these dynamical modes are stable or meta-stable (oscillation and pulsation), while other modes lose knowledge of the ‘initial’ envelope structure (transition, ejection, and collapse). Detailed description of the dynamical modes is available in Sect. 3.4.1: *Types of dynamical behavior*.

Dynamical diversity of embryo cores

During the earliest stages of the protoplanetary evolution, protoplanetary cores, composed from accreted solids, are believed to be unable to trigger the rapid gas accretion or the envelope collapse, upon a ‘small perturbation’; such cores do not have the ‘critical mass’ believed necessary for further evolution into a mature planet.

However, in our classification of static equilibria, we have shown that sub-critical cores (embryos) can have several qualitatively different envelope structures (e.g. quasi-uniform and non-self-gravitating, quasi-uniform and self-gravitating, and compact self-gravitating). A question naturally followed: ‘*Can sub-critical cores with qualitatively different envelope structures have different dynamical properties?*’. If this would be the case, than protoplanetary embryos could take different evolutionary paths already in the very early stages of their existence.

In order to understand this potential dynamical diversity, we have investigated a typical subcritical core mass for all the different envelope structures it can take, and have found out that five basic dynamical regimes are possible: oscillation, transition, collapse, ejection+transition, and pulsation (c.f. bottom plot in Fig.4.1).

The results of the hydro-dynamical calculations agreed quite well with the predictions of the linear stability analysis (c.f. Schönke, 2005), i.e. the boundary between the stable and the unstable core-envelope equilibria, obtained with the linear stability analysis,

agrees well with the same boundary coming from the hydro calculations. However, linear stability analysis predicts a stable solution for the ‘mature gas giant’ region models (ones with the highest ρ_{cs}), while hydro calculations show that the ‘mature gas giant’ is only meta-stable, and that such models experience a ‘pulsation’ (c.f. Sect. 3.4.2 for details). Furthermore, we show that the ‘protoplanet’ region, predicted by linear stability analysis to be unstable, actually exhibits three different kinds of dynamical phenomena. One of those (‘transition’) shows several indications that its a linear instability, while the other two (‘collapse’ and ‘ejection’) appear to have a non-linear nature (again, c.f. Sect. 3.4.2 for details).

On the issue of borders between different protoplanetary regions, we note that *the borders defined for the static classification do not agree with the borders defined by dynamical properties*. It came somewhat as a surprise that, for some nebulae, stable quasi-homogenous and self-gravitating (i.e. quite massive) equilibria exist (c.f. bottom plot of Fig. 4.1, for models with $10^{-5} < \rho_{\text{cs}} < 10^{-4}$). Such models can even be end-states of the transition which comes after a ‘strong perturbation’, i.e. after a complete destruction of the initial envelope structure (c.f. Sect. 3.4.2).

These models have envelope surface densities that are comparable to the asteroid density, and could consequently have their core-accretion cross-sections increased by several orders of magnitude². This could possibly be a venue for a *fast core accretion process*, one which could produce a significant (even critical) core in just a fraction of the canonical critical core growth time-scale (present-day best-guess value is around 5-10 Ma).

Another alternative for a rapid gas giant formation could be facilitated through initiation of a collapse for the subcritical core-envelope structure. Our investigation showed that collapse *is* one of the possible dynamical modes of the subcritical core. It is clear that

²For example, planet-model 8 from the subcritical core survey (see Fig. 3.18), has an average envelope density of $\overline{\rho_{\text{env}}} = 4.75 \cdot 10^{-6} \text{ kg m}^{-3}$, and a radius of $r_{\text{Hill}}(m8) = 3.4 \cdot 10^{10} \text{ m}$. This gives a column density of $\approx 3.2 \cdot 10^5 \text{ kg m}^{-2}$. Such an envelope, overdense relative to the nebula, would barely slow down a 10 km asteroid with $\rho_{\text{aster}} = 3000 \text{ kg m}^{-3}$ (effect would be on a percent level). But it also means that any asteroid smaller than 100 m, crossing a significant part of the protoplanet’s envelope, would be captured by the protoplanet!

the core-envelope structure required for the initiation of the collapse can not be reached, if one considers only the time-sequence of hydrostatic models with a (discretely) growing core, i.e. if only small perturbations are possible.

But at present time we can not exclude the possibility that the subcritical core collapse could be initiated by a large perturbation (e.g. by a collision with a core of similar size). Once started, collapse would end only after most of the available mass reservoir is eaten up, leaving the protoplanet with the compact envelope. We have shown that the compact envelope structure is meta-stable. Thus, once such compact equilibrium is reached, it would remain compact during consecutive evolutionary stages.

Such an evolutionary scenario could explain Jupiter's possibly subcritical core (see e.g. Guillot, 1999; Wuchterl et al., 2000). It could also serve as an alternative for the formation of gas giants in very young planetary systems (e.g. Neuhaeuser et al., 2005).

We have performed another dynamical survey of the typical subcritical core. This survey is equivalent in scope to the one discussed above, but for models with a much lower core density - $\rho_{\text{core}} = 1.5 \cdot 10^{-4} \text{ kg m}^{-3}$ (c.f. Sect.1.3.11 for a comparison of manifolds with different core densities).

Although such a low core density is more reminiscent of the protoplanetary nebulae than of the density of the solids, it was important to perform the dynamic analysis, because this core density closely corresponds to the effective core density of the 'gravitationally smoothed' models in the state-of-the-art disk-planet-interaction type calculations, (e.g. Kley, 1999; D'Angelo et al., 2003; Nelson and Papaloizou, 2004).

In brief (c.f. Sect. 3.4.3 for details), we have found dynamical behavior similar to the one for the models with the medium core density, but with several important differences, of which we state two here (c.f. summary of Sect. 3.4.3 for the others); first, the 'mature gas giant' region is unstable - we have been unable to find a compact equilibrium stable against collapse, and second, the 'ejection+transition' dynamical mode (c.f. Fig.4.1) from the 'protoplanet' region appears to be missing.

Hence, we conclude that *the low core density solution manifold has dynamical properties which are qualitatively different from the dynamical properties of the medium core density solution manifold* (and, along the same line, different from the dynamical properties of the solution manifold with the core density of solids).

Collapse of the Critical Core

As we state in the introduction to the summary, the role of the critical mass in the planetary evolution is still poorly understood. Hence, another focus of our dynamical survey was the manifold region around the critical core mass (red square on the right side of the upper plot of Fig. 4.1).

In this analysis, we covered the manifold region within a factor of two (in core-mass) around the critical core (c.f. Fig. 3.23 for the model grid around the critical core mass). The most important finding of this analysis is:

All of the states around the critical core mass are unstable against collapse.

This is true regardless if the models are sub- or super-critical, self-gravitating or not, as long as they are in vicinity of the critical core. The general instability against collapse is not in agreement with the prediction of the linear stability analysis by Schönke (2005) (compare the red box on the right side of the upper plot of Fig. 4.1 with the dashed line). Disagreement indicates that *the critical core mass is associated with* at least one kind of *non-linear instability*.

Furthermore, from the general instability against collapse we see that the envelope collapse will be a prominent evolutionary feature as soon as the core grows to (at most) half the size of the critical core; i.e. *a protoplanet can start the dynamical part of its early evolution even with a subcritical core, and regardless of the nebula environment the protoplanet is in.*

The effect of this instability is obviously greatly reduced, if not completely removed, in case of a typical subcritical core mass model (e.g. the subcritical core which we have

chosen in our previous survey). Exactly to how small cores the non-linear, critical-core-instability reaches will presently remain unknown.

For the details of the critical core region study, we refer the reader to Sect. 3.4.2: *Region around the critical core*.

Outlook

Although most of the goals of this study have been achieved, in the light of the new results we deem several avenues worth of further study.

Within a current physical model, we feel that an additional investigation of the dynamical properties of the supercritical models would be important, as well as the study of the boundaries of the unstable region around the critical core mass.

A better developed analytic description would be valuable, but due to intrinsic non-linearity of the system it is at present unknown how powerful traditional analytic analysis could be. Alternative approach would be to develop a thermodynamic formalism for self-gravitating system with core, retracing the steps done by Stahl et al. (1995) for coreless gas spheres.

Furthermore, the investigation of the highly distorted region around the critical core mass of the low-core-density manifold would probably improve understanding and interpretation of the results of the global disk-planet interaction type calculations.

A solution for the qualitatively correct gas flows in the protoplanet's vicinity, for the disk-planet interaction type calculations, would be to couple the (kind of) hydro code which we used to the global 2D/3D hydrodynamical disk model. Spherical symmetry is a good approximation of the envelope stratification deep in the gravitational potential of the protoplanet. Thus, such a model, embedded within a disk model covering the rest of the protoplanetary disk, would provide a (far) better representation, of the protoplanet's feedback onto the disk, than present day state of the art disk-planet models have.

A concept of the solution manifold needs to be further developed, for a system with

better microphysics. The protoplanet's surroundings - the nebula - needs to be described in a physically meaningful way, but one which would not over-constrain the model of planet itself. Additionally, a new paradigm is most likely needed for the core-luminosity-temperature relation at the core surface of the protoplanet.

Once a concept is developed for a solution manifold which includes more physics than the present study, it would be very important to redo the hydro-dynamical surveys, analogous to the ones we did within this investigation.

Bibliography

- P. Bodenheimer and J. B. Pollack. Calculations of the accretion and evolution of giant planets The effects of solid cores. *Icarus*, 67:391–408, September 1986.
- P. Bodenheimer, T. Ruzmajkina, and R. D. Mathieu. Stellar multiple systems - Constraints on the mechanism of origin. In *Protostars and Planets III*, pages 367–404, 1993.
- P. Bodenheimer, O. Hubickyj, and J. J. Lissauer. Models of the in Situ Formation of Detected Extrasolar Giant Planets. *Icarus*, 143:2–14, January 2000.
- C. Broeg. Doctoral Thesis. *Doctoral Thesis AIU-Jena*, 2005.
- N. F. Carnahan and K. E. Starling. Equation of state for nonattracting rigid spheres. *The Journal of Chemical Physics*, 51(2):635–636, 1969. URL <http://link.aip.org/link/?JCP/51/635/1>.
- C. H. Chen, M. Jura, K. D. Gordon, and M. Blaylock. A Spitzer Study of Dusty Disks in the Scorpius-Centaurus OB Association. *ApJ*, 623:493–501, April 2005.
- A. C. Clarke. *2001: A Space Odyssey*. Arrow Books, 1968, 1968.
- R. Courant and K. O. Friedrichs. *Supersonic flow and shock waves*. Pure and Applied Mathematics, New York: Interscience, 1948, 1948.
- R. Courant, K.O. Friedrichs, and H. Lewy. Über die partiellen Differenzgleichungen der mathematischen Physik. *Math. Ann.*, 100:32–74, 1928.
- G. D’Angelo, T. Henning, and W. Kley. Nested-grid calculations of disk-planet interaction. *A&A*, 385:647–670, April 2002.

- G. D'Angelo, W. Kley, and T. Henning. Orbital Migration and Mass Accretion of Protoplanets in Three-dimensional Global Computations with Nested Grids. *ApJ*, 586: 540–561, March 2003.
- F. Garvan. *The Maple Book*. Chapman & Hall, 2001.
- T. Guillot. Interior of Giant Planets Inside and Outside the Solar System. *Science*, 286: 72–77, October 1999.
- C. Hayashi, K. Nakazawa, and Y. Nakagawa. Formation of the solar system. In *Protostars and Planets II*, pages 1100–1153, 1985.
- M. Ikoma, H. Emori, and K. Nakazawa. Formation of Giant Planets in Dense Nebulae: Critical Core Mass Revisited. *ApJ*, 553:999–1005, June 2001.
- R. Kippenhahn and A. Weigert. *Stellar Structure and Evolution*. Stellar Structure and Evolution, XVI, 468 pp. 192 figs.. Springer-Verlag Berlin Heidelberg New York. Also Astronomy and Astrophysics Library, 1990.
- W. Kley. Mass flow and accretion through gaps in accretion discs. *MNRAS*, 303:696–710, March 1999.
- T. Kusaka, T. Nakano, and C. Hayashi. Growth of solid particles in the primordial solar nebula. *Progress of Theoretical Physics*, 44:1580–1595, 1970.
- R. J. LeVeque, D. Mihalas, E.A. Dorfi, and E. Müller. *Saas-Fee Advanced Course 27: Computational Methods for Astrophysical Fluid Flow*. Springer-Verlag, 1997.
- J. J. Lissauer. Planet formation. *ARA&A*, 31:129–174, 1993.
- H. Mizuno. Formation of the Giant Planets. *Progress of Theoretical Physics*, 64:544–557, August 1980.
- H. Mizuno, K. Nakazawa, and C. Hayashi. Instability of a gaseous envelope surrounding a planetary core and formation of giant planets. *Progress of Theoretical Physics*, 60: 699–710, September 1978.

- G. E. Morfill, W. Tscharnuter, and H. J. Voelk. Dynamical and chemical evolution of the protoplanetary nebula. In *Protostars and Planets II*, pages 493–533, 1985.
- R. P. Nelson and J. C. B. Papaloizou. The interaction of giant planets with a disc with MHD turbulence - IV. Migration rates of embedded protoplanets. *MNRAS*, 350:849–864, May 2004.
- R. Neuhaeuser, E. W. Guenther, G. Wuchterl, M. Mugrauer, A. Bedalov, and P. H. Hauschildt. Evidence for a co-moving sub-stellar companion of GQ Lup. *ArXiv Astrophysics e-prints*, March 2005.
- F. Perri and A. G. W. Cameron. Hydrodynamic instability of the solar nebula in the presence of a planetary core. *Icarus*, 22:416–425, August 1974.
- V. S. Safronov. *Evoliutsiia doplanetnogo oblaka*. 1969., 1969.
- N. C. Santos, G. Israelian, M. Mayor, R. Rebolo, and S. Udry. Statistical properties of exoplanets. II. Metallicity, orbital parameters, and space velocities. *A&A*, 398:363–376, January 2003.
- S. Sasaki. Minimum planetary size for forming outer Jovian-type planets - Stability of an isothermal atmosphere surrounding a protoplanet. *A&A*, 215:177–180, May 1989.
- D. Saumon, G. Chabrier, and H. M. van Horn. An Equation of State for Low-Mass Stars and Giant Planets. *ApJS*, 99:713–+, August 1995.
- J. Schönke. Linear Stability of the Isothermal Protoplanetary Equilibria. *Diploma Thesis AIU-Jena*, 2005.
- M. Schwarzschild. *Structure and evolution of the stars*. Princeton, Princeton University Press, 1958.
- F. H. Shu. *Physics of Astrophysics, Vol. II*. Physics of Astrophysics, Vol. II, by Frank H. Shu. Published by University Science Books, ISBN 0-935702-65-2, 476pp, 1992., 1992.
- G. A. Sod. A survey of several finite difference methods for systems of nonlinear hyperbolic conservation laws. *J. Comp. Phys.*, 27:1–31, April 1978.

- B. Stahl, M. K.-H. Kiessling, and K. Schindler. Phase transitions in gravitating systems and the formation of condensed objects. *Planet. Space Sci.*, 43:271–282, February 1995.
- D. J. Stevenson. Formation of the giant planets. *Planet. Space Sci.*, 30:755–764, August 1982.
- S. Udry, M. Mayor, and N. C. Santos. Statistical properties of exoplanets. I. The period distribution: Constraints for the migration scenario. *A&A*, 407:369–376, August 2003.
- K. H. A. Winkler and M. L. Norman. *Astrophysical Radiation Hydrodynamics*, volume 237. D. Reidel Publishing Company, ISBN 90-277-2335-4, 590p, 1982, July 1987.
- G. Wuchterl. Hydrodynamics of giant planet formation: II - Model equations and critical mass. *Icarus*, 91:39–64, May 1991a.
- G. Wuchterl. Hydrodynamics of giant planet formation III: Jupiter’s nucleated instability. *Icarus*, 91:53–64, May 1991b.
- G. Wuchterl. The critical mass for protoplanets revisited - Massive envelopes through convection. *Icarus*, 106:323–+, November 1993.
- G. Wuchterl, T. Guillot, and J. J. Lissauer. Giant Planet Formation. *Protostars and Planets IV*, pages 1081–+, May 2000.

CURRICULUM VITAE

Bojan Pečnik

born in Zagreb, Croatia, on 2nd of July, 1975

	education
2004-	PhD in Physics and Astronomy at Astrophysical Institute and University Observatory Jena from March 2004
2001-2004	PhD in Physics and Astronomy at Max-Planck-Institut für extraterrestrische Physik. In March 2004 moved to AIU Jena
1994-2001	BSc in Astrophysics from University of Zagreb, Faculty of Sciences, Physics Department
1990-1994	Technical school 'Rugjer Bošković', Zagreb
1983-1990	Elementary school 'S. S. Kranjević', Zagreb
	professional experience
2003	Third Helmholtz Summer School, Potsdam, 'Chaos and stability in planetary systems'
2002	International Space University's Summer School Program at Pomona, California, USA, with 'Jim Burke' scholarship
2001-2004	PhD in Physics and Astronomy at Max-Planck-Institut für extraterrestrische Physik, Garching bei München, on theory of Formation of gas giant planets, under supervision of prof. Gregor Morfill
2000	Traineeship in Max-Planck-Institut für Plasmaphysik Garching bei München, under prof. H. Zohm
1999	Traineeship in 'Centro Federal de Educação Tecnológica do Paraná, Departamento Academico de Física' (CEFET-PR), Curitiba, Parana, Brasil